Active hydrodynamics of actomyosin elastomer with turnover during tissue remodeling

by

Deb Sankar Banerjee

2018

A thesis submitted to
the Jawaharlal Nehru University for the degree of
Doctor of Philosophy

Certificate:

This is to certify that the thesis entitled **"Active hydrodynamics of actomyosin elastomer with turnover during tissue remodeling"** submitted by Deb Sankar Banerjee for the award of the degree of Doctor of Philosophy of Jawaharlal Nehru University is his original work. This has not been published or submitted to any other University for any other Degree or Diploma.

Prof. Ravi Subrahmanyan
(Director)
Raman Research Institute
Bangalore 560 080
India

Prof. Madan Rao
(Thesis Supervisor)

Declaration:

I hereby declare that the work reported in this thesis is entirely original. This thesis is composed independently by me at Raman Research Institute under the supervision of Prof. Madan Rao. I further declare that the subject matter presented in this thesis has not previously formed the basis for the award of any degree, diploma, membership, associateship, fellowship or any other similar title of any university or institution. I also declare that I have run this thesis through the plagiarism checking software *Turnitin* before submission.

Prof. Madan Rao

Deb Sankar Bnerjee

Theoretical Physics
Raman Research Institute
Bangalore 560 080
India

Dedicated to

My Mother Reba Banerjee &
My Late Father Gouri Sankar Banerjee

Acknowledgements

I am grateful to my supervisor Prof. Madan Rao for all the advices, care and help I received from him. He changed my scientific vision in many different ways. I thank Prof. Thomas Lecuit for many fruitful discussions and great insights that encouraged me on my pursuit of science. I will remain grateful to Akankshi, Girish, Ankita and other Lecuit lab members for their hearty welcome and support during my visit to Marseille and for the biological insights I gained from them.

I would like to thank Prof. Yashodan Hatwalne, Prof. Pramod Pullarkat, Prof. V.A. Raghunathan and other SAAC members for numerous helpful feedbacks on various occasions and their mentoring throughout my PhD. I have enjoyed working with Vijay Kumar Krishnamurthy and Mandar Inamdar and learned many things from them during the course of my PhD. I am grateful to Sriram Ramaswamy for all the insightful discussions we had. I want to thank all the faculties who taught us in IISc and RRI for their invaluable teachings. I want to thank Debarghya Banerjee, Richard Morris and Ananya Mitra for discussions that helped me greatly in my research. My life would have been difficult without all the support that I got from the scientific community in RRI, IISc, NCBS and Simons Center.

After spending all these years alongside my lab members, I really think it could not have been better anywhere else. I cannot thank you all enough for being with me through all these times, to Raj, Rituparno, Suman, Kabir, Amit, Amit, Amit, Alkesh, Krishnan, Alex.

I want thank my friends and peers in IISc and RRI: Adhip, Suman, Narendra, Tathagata, Tanujit, Saiantan, Shivam, Aniruddha, Santanu, Shusil, Deepak, Meera, Niranjan, Raviranjan and many more. Its not possible to thank you enough for all the experiences that we shared. And a spacial thank to Sufi Raja, without you our life would be “tasteless”! I have been blessed with some crazy friends : Abhishek and Riya.

Acknowledgements

I have never seen a more friendly office than the RRI admin, I thank you all for helping me whenever the need was there. I would like to thank K. Radha, Marisa, Vidya for all their help. I would also like to thank NCBS administration for hosting me and for all their numerous help and support.

When nothing works out I go running to these people and they have been always there for me - Moumita, Rituparno, my three sisters and bordavai. I cannot express my feelings in words but nothing would be possible without your constant support in everything: Maa. Finally there is no acknowledgement I can give to my family, whatever good is there in me has come from all of you.

Synopsis

Embryonic developmental processes in organisms involve well orchestrated changes in shape, size and organization of the tissues. This remodeling of shape in tissue (during embryonic development or elsewhere) is referred as *tissue morphogenesis*. Tissue morphogenesis emerges from actively driven shape, size or relative position changes in the constituent cells. These changes at cellular scale happen through self organized mechano-chemical dynamics of sub-cellular structures. The apical actomyosin network is one major example of such sub-cellular machinery that drives cell shape changes which result in tissue morphogenesis. Here we constrain our study within a broad range of phenomena where actomyosin pulsation and flow drive changes in cell shape and cell organization which in turn remodel the whole tissue.

Active hydrodynamics of actomyosin pulsation and flow

Here we describe the hydrodynamics of the actomyosin cytoskeleton as a confined active elastomer embedded in the cytosol and subject to turnover of its components. Our treatment is adapted to describe the diversity of contractile dynamical regimes observed *in vivo*. When myosin-induced contractile stresses are low, the deformations of the active elastomer are *affine* (homogeneous deformation over a spatially coarse-grained scale), and exhibit features of an excitable medium, including spontaneous oscillations, propagating waves, contractile collapse and spatiotemporal chaos. The collective nonlinear dynamics shows nucleation, growth and coalescence of actomyosin-dense regions which, beyond a threshold, spontaneously move as a *spatially localized traveling front*. However, large myosin-induced contractile stresses, can lead to *non-affine* deformations due to enhanced actin and crosslinker turnover. This results in a *transient actin network* that is constantly remodeling and naturally accommodates large intermittent strain fluctuations and *intra-network flows* of the

actomyosin dense regions.

Our work suggests that the driving force for the spontaneous movement, both of the travelling front and the intra-network flows, comes from the actomyosin-dense region itself and not the cell boundary. These symmetry breaking flows correspond to spatially localized traveling front solutions of the active hydrodynamic equations. We verify many predictions of our study in *Drosophila* embryonic epithelial cells undergoing neighbour exchange during a collective process of tissue extension called germband extension.

Reliable and robust junction shrinkage through actomyosin pulsation and flow

In a tissue, cells adhere to each other to form *cell junctions* and maintain integrity the tissue. In many cases of tissue morphogenesis, organizational changes are driven by active remodeling of cell junctions. Here we construct a dynamical model of cell junction stating from a local hydrodynamic description of actomyosin network (as an active elastomer) and E-cadherin adhesive complexes. We use this theory to understand junction shrinkage during cellular intercalation which leads to germband extension.

We show that this description is able to capture the qualitative behaviour of a junction shrinkage observed during *in vivo* experiments. We also address a very important question in the context of tissue morphogenesis: how the noisy dynamics of local molecular force generators ultimately results in reliable and robust shape changes at the cellular and tissue scale? In this work we identify a novel molecular mechanism, based on two pools of myosin (active stress generators) working in tandem, that provide a robust and reliable shrinkage of junction.

Prof. Madan Rao Deb Sankar Bnerjee

Raman Research Institute
Bangalore, India.

Publications

- Actomyosin pulsation and flows in an active elastomer with turnover and network remodeling
  Deb Sankar Banerjee, Akankshi Munjal, Thomas Lecuit and Madan Rao
  Nature Communications **8**, Article number: 1121 (2017)
  doi:10.1038/s41467-017-01130-1

- Medial and Junctional Myosin work in tandem to ratchet junctional shrinkage
  Deb Sankar Banerjee, Kabir B. Husain, Girish Kale, Thomas Lecuit and Madan Rao
  Manuscript under preparation.

Contents

Acknowledgements **ix**

Synopsis **xi**

Publications **xiii**

1. Introduction **1**

1.1. Tissue morphogenesis 1

1.2. Active matter 3

1.3. Phenomenology of germband extension 5

1.3.1. Convergence-Extension of tissue 7

1.3.2. Cellular intercalation 8

1.3.3. Actomyosin pulsation and flow 11

1.4. Hydrodynamics 13

1.5. Layout of this thesis 14

2. Dynamics of apical actomyosin as an active nonlinear spring **17**

2.1. Introduction 17

2.2. Description of the active nonlinear spring 19

2.3. Equation of motion 20

2.4. Spontaneous oscillations and contractile instability 21

2.5. Need for a hydrodynamic description 24

3. Hydrodynamics of apical actomyosin as an active elastomer : Affine description **27**

3.1. Different regimes of actomyosin dynamics during tissue morphogenesis 27
3.2. Hydrodynamic description of actomyosin 28
3.2.1. Elements of the theory 28
3.2.2. Dynamics of elastomer network 30
3.2.3. Dynamics of active force generators 31
3.2.4. Dynamics of ambient fluid 32
3.2.5. Forces and stresses 32
3.3. Resulting equations 34
3.4. Linear stability analysis of active elastomer 35
3.4.1. Linear equations 35
3.4.2. Fastest growing mode : Instabilities of the homogeneous state 37
3.4.3. Phase diagram 39
3.5. Active elastomer in one dimension 42
3.6. Mode truncated analysis 42
3.7. One mode analysis 44
3.7.1. Mapping to Van der Pol oscillator 44
3.7.2. Limit cycle and Hopf-bifurcation 46
3.8. Two modes analysis 49
3.8.1. Resulting equations 50
3.8.2. Bifurcation and limit cycle 50
3.8.3. Chaos 53
3.9. Concluding Remarks 57

4. Numerical solution of affine active elastomer : Spatiotemporal features **59**

4.1. Introduction 59
4.2. Equation of motion 60
4.3. Steady state phases and phase diagram 62
4.4. Nucleation, growth and coalescence 67

4.5. Asymmetric profile of traveling front 69
4.6. Dynamics of traveling front 70
4.7. Spatiotemporal Chaos in coexistence phase 73
4.8. Concluding remarks 75

5. Non-affine dynamics of apical actomyosin : Transient network description 77
5.1. Introduction 77
5.2. Where the affine theory works and where we need a non-affine description 77
5.3. Nonaffine elastomer with network remodeling and intranetwork flow 79
5.4. Comparison with experiments 82
5.5. Physical values of rescaled parameters 89
5.6. Concluding remarks and future directions 89

6. Dynamics of junction shrinkage 91
6.1. Introduction 91
6.2. Theoretical description of a junction 92
6.3. Dynamical equations for junction 95
6.3.1. Constitutive formulae: dependence of phenomenological parameters on myosin and cadherin 96
6.3.2. Steady state of the junction 99
6.3.3. Classification of dynamical phases 99
6.4. Junction shrinkage with fixed cadherin level : Unreliable shrinkage . 100
6.4.1. No reliable stepwise shrinkage in junction with fixed cadherin level 100
6.5. Junction shrinkage with leaky cadherin level : Reliable shrinkage . . . 102
6.5.1. Permanent change in junction length: Effect of a single pulse . 104
6.5.2. Reliable stepwise shrinkage 105
6.5.3. Timescales in junction shrinkage 107
6.5.4. Robustness against noise? 107

6.6. Robust and reliable shrinkage requires medial and junctional myosin working in tandem . . . 108
6.6.1. Forces from medial actomyosin stabilize cadherin clusters . . . 109
6.6.2. Robustness of stepwise shrinkage : Against external noise . . . 110
6.6.3. Robustness of stepwise shrinkage : Against internal noise . . . 112
6.7. Concluding remarks and future directions . . . 113

A. Appendix **115**
A.1. Strain dependent unbinding . . . 115
A.2. Numerical methods . . . 117
A.3. Experimental methods . . . 118
A.4. Image analysis : Actomyosin pulsation and flow . . . 118
A.5. Junction shrinkage calculations . . . 120
A.6. Approximate analytical solutions: Fixed cadherin level dynamics (single pulse) . . . 123
A.7. Approximate analytical solutions: Fixed cadherin level dynamics (pulse train) . . . 129
A.8. Approximate analytical solutions: Leaky cadherin level dynamics . . . 132

Bibliography **136**

List of Figures

1.1. Tissue morphogenesis driven by cell shape change 3
1.2. Active matter 4
1.3. Geometry of the germband tissue and the constituent cells 6
1.4. Germband extension in *Drosophila melanogaster* 7
1.5. Convergence-extension through cellular rearrangements 8
1.6. Cellular intercalation 10
1.7. Dynamics of apical actomyosin network drives the intercalation . . . 12

2.1. Dorsal closure in *Drosophila Melanogaster* 18
2.2. Area oscillation during actomyosin pulsation 18
2.3. Schematic diagram of the active nonlinear spring 19
2.4. Spontaneous oscillation and contractile instability in actomyosin density 23
2.5. Phase diagram in renormalized contractile stress and stiffness ratio . 24

3.1. Different timescales in actomyosin dynamics 27
3.2. Active elastomer schematic 30
3.3. Fastest growing mode in linear stability 38
3.4. Phase diagram and dispersion relations from linear stability 40
3.5. Frequency of oscillation from linear analysis 41
3.6. Stable, oscillatory and contracted steady state from one mode analysis 46
3.7. Hopf-bifurcation 47
3.8. Effects of nonlinearities 48
3.9. Spontaneous oscillations and chaos in two mode analysis 51
3.10. Bifurcation diagrams from two mode analysis 52
3.11. Limit cycle in phase space of u_1, ρ_{b1}, ρ_{b2} 52
3.12. Indication of chaos in bifurcation diagram structures 54

3.13. Chaotic trajectories in phase space of u_1, ρ_{b1}, ρ_{b2} 55
3.14. Aperiodic chaotic solutions 56
3.15. Maximal Lyapunov exponents for u_1, ρ_{b1}, ρ_{b2} 57

4.1. Actomyosin pulsation and flow 60
4.2. Effective elastic free-energy of the active elastomer 62
4.3. Phase diagram obtained from numerical solutions 64
4.4. Phases obtained from numerical solutions 65
4.5. Timescales in active elastomer dynamics 66
4.6. Nucleation, growth and coalescence during actomyosin dynamics . . . 67
4.7. Kymographs of bound myosin density 68
4.8. Time evolution of bound myosin density profile 70
4.9. Anatomy of the traveling front 72
4.10. Possible mechanisms for the movement of actomyosin-dense structures 73
4.11. Spatio-temporal chaos in the kymograph of bound myosin density and displacement field 74
4.12. Lyapunov spectrum calculated from coexistence phase shows spatiotemporal chaos 75

5.1. Timescales of oscillation, front propagation and contractile collapse . 80
5.2. *Advection* is crucial to obtain oscillations of bound myosin 84
5.3. Spatial profile and movement of myosin dense regions 85
5.4. Velocity and profile of myosin dense regions 87
5.5. Direction reversals of the moving myosin-dense cluster upon coalescence 88

6.1. Junction shrinkage from actomyosin pulsation and flow 92
6.2. The thick junction and the thin junction schematic 94
6.3. Phenomenological relations 97
6.4. Dynamic phases of junction shrinkage dynamics from experiments . . 98
6.5. Fixed cadherin level produces unreliable shrinkage 102
6.6. Leaky cadherin level produces permanent deformation of junction and reliable shrinkage 105
6.7. Reliable stepwise shrinkage lacks robustness 106

6.8. Medial and junctional myosin work in tandem to produce robust ratcheting of junction 109
6.9. Robustness of stepwise shrinkage phase via medial pulse dependent stabilization of cadherin: Against external noise 111
6.10. Robustness of stepwise shrinkage phase via medial pulse dependent stabilization of cadherin: Against internal noise 113

A.1. Strain dependent unbinding: effect of α sign 116
A.2. Protocol for image analysis 119

List of Tables

3.1. Dimensionless redefinitions 36
3.2. Phases from linear stability analysis 37
3.3. One mode analysis 49
3.4. Two mode analysis 57

6.1. Parameter values 102
6.2. Parameter values 105
6.3. Parameter values 106
6.4. Parameter values 111
6.5. Parameter values 113

Chapter 1

Introduction

In a multicellular organism many cells come together (adhere) to take a *form* and perform specific functions. These organization of cells which interact chemically and mechanically with the neighbouring cells, are called *tissue* [1]. A tissue can be very dynamic as a structure and shape, size or organization of a tissue can change with time as it undergoes *remodeling*. When a tissue undergo remodeling of its shape it is generally referred as *tissue morphogenesis*.

In this study we aim to understand the physics of remodeling of tissue shape in terms of shape-change in individual cells and dynamics of the sub-cellular elements that drive the changes in cell shape. In this chapter we introduce and discuss the physical and biological ideas that are crucial to our work and the main motivations for this study.

We start with a discussion about tissue morphogenesis with an aim to introduce it with necessary details and physical insights. We then briefly introduce the physics of active matter and describe tissue as an example of active matter. Next we consider a particular case of tissue morphogenesis and discuss the phenomenology involved at various scales (tissue - cellular - sub-cellular). Finally we discuss the preliminary ideas on how a coarse grained theoretical description can be used to understand the physics of tissue remodeling at large lengths and long times.

1.1 Tissue morphogenesis

The word *morphogenesis* literally means the creation (*genesis*) of shape (*morphê*). The process of development of an multicellular organism starts from a single cell

that divides into many cells which then organize to form an embryo and with time the embryo morphs into the organism with defined limbs and organs. This formation and transformation of an embryo into an organism is referred as *embryogenesis*. During embryogenesis collection of cells assemble to form tissues. To organize the embryo and to form organs, these tissues undergo a wide variety of changes ranging from comparatively simple overall shape or size change of the tissue to complicated topological or geometrical changes at tissue scale [2]. This process of rendering *form* to the tissues, seen during embryonic development, is referred as *tissue morphogenesis*.

Tissue morphogenesis is a result of the well organized change in shape, size or coordination of its constituent cells. Some of the well studied examples of such cases of tissue morphogenesis are invagination of mesoderm tissue during *gastrulation* and convergence-extension of germband tissue during *germband extension* in *Drosophila melanogaster*. Mesoderm invagination involves bending and fold formation in the mesoderm tissue achieved by *apical constriction* of individual cells [3, 4] (Fig.1.1 a) whereas *intercalation* of individual cells results in germband extension [5] (Fig.1.1 b) where the overall shape of the germband tissue changes. It is to be noted that local changes in each cells can interact with changes in neighbouring cells via adhesive connections to produce an integrated effect at tissue scale [6].

Following the similar principle of local dynamics giving rise to global effects, the dynamics of constituent molecular components of a cell collectively drives the changes in the shape or size of a cell [2].

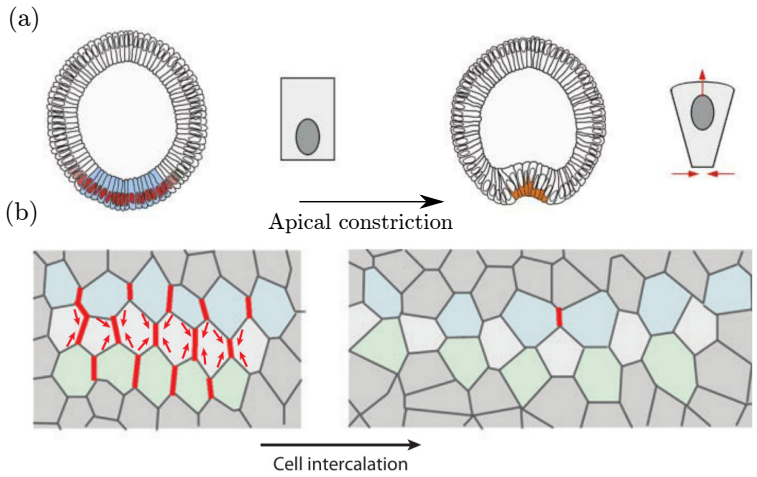

Figure 1.1. Tissue morphogenesis driven by cell shape change: (a) Apical constriction in mesoderm cells result in fold formation during mesoderm invagination (figure from [4]). (b) Tissue shape change during germband extension happens through cellular intercalation at each cell (figure from [3]).

In the above mentioned cases of tissue morphogenesis, the local forces generated by the contractile machinery of actomyosin drive both intercalation [7] and apical constriction [8] through remodeling of cell junction and apical surface of cell respectively.

Next we briefly describe *active matter* and how a tissue fits into the active matter description. We then focus on a particular case of tissue morphogenesis called germband extension in *Drosophila melanogaster* to discuss the processes involved in tissue remodeling across different scales from tissue to sub-cellular actomyosin network. The phenomenology of germband extension and the theoretical descriptions used to understand germband extension will be presented in following sections.

1.2 Active matter

Study of *active matter* is a relatively new field of physics and has drawn significant interest from many pure and inter-disciplinary branches of science. *Active matter* refers to a system where the constituent elements are driven by energy infusion (from the energy sources present inside the element or in the ambient medium) and energy dissipation (through inter-element collision, substrate friction etc) at the scale of the individual elements [9, 10]. Active systems can produce systematic

movement through this energy intake and dissipation at microscopic scale and are far from thermodynamic equilibrium [10, 9]. Active matter is different from an externally/boundary driven non-equilibrium system as the time reversal symmetry is broken at the level of the individual constituent elements.

Active matter can be living or non-living. Active matter systems can be found across different length scales (see Fig. 1.2) ranging from a scale of few hundred nano-meters (self propelled colloidal particles [16] or nanorods [15]) or a few micro-meters (bacteria colony [13] or cell cytoskeleton [19]) to several kilometers (animal migration [17]). Dynamical features in active matter can be slow or fast and span across different timescales from few seconds (vibrated granular rods [14]) to few hours (cell migration in confluent tissue [18]).

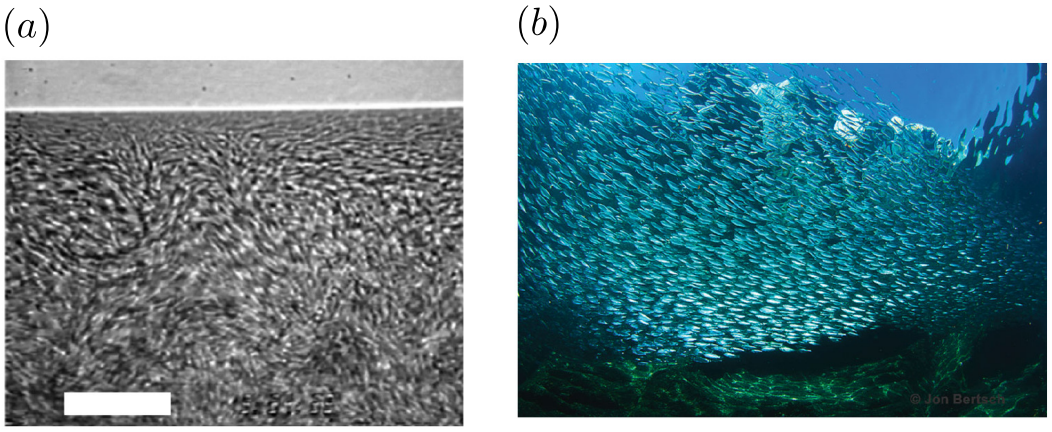

Figure 1.2. Example of active matter at (a) microscopic length scale : *Turbulence* in growing bacteria colony of *Bacillus subtilis* is an example of turbulence in highly viscous media (low Reynolds number) where each bacteria behave as an active element [13]. Scale bar is $35\,\mu m$. (b) Active matter at macroscopic length scale : A school of fish shows remarkable collective dynamics and emergent polar order in their collective motion has been widely studied [21, 22] (Figure from [20]).

Living active matter like cells, tissues, bacteria colony, a flock of birds all use chemically stored energy at the level of the respective active elements (each bacteria in the colony, each cell in the tissue and such) to exhibit *activity*. We shall mainly discuss about living active matter in this study. Such are usually very complex in their entirety. A single living cell presents an immensely complex system to study with huge variety of molecular components and various interactions among these components happening at different lengthscales and timescales . This scope

for seemingly immense diversity in behaviour can be constrained by global physical principles such as symmetries, conservation laws etc. Thus it is important to try and uncover these underlying global principles from a particular feature observed in living active matter. This has been done very successfully in the case of dynamics of active membranes [23], theory of flocking [22], large length scale dynamics of cytoskeleton [24] etc.

Living active matter systems has also been studied using a minimal microscopic description with emphasis on order, fluctuations and collective behaviour. Some notably successful and important works in this direction are studies on flocking [21, 25] and semiflexible filaments with crosslinkers and active stress generators to understand cytoskeletal dynamics [26] etc.

In the case of tissue remodeling the active constituent elements can be defined in a context dependent manner. For the cellular level the sub-cellular constituent elements of cytoskeleton act as the active elements by exerting local forces through conformational changes achieved using chemically stored energy from the ATP hydrolysis reaction. Then at the tissue scale the active matter description can be achieved by considering the individual cells as the active elements changing shape (or size) or going through topological transitions by using chemically stored energy inside each cell.

In the next section we discuss a particular case of tissue remodeling and describe how tissue morphogenesis is driven by active processes at various scales in the tissue - from sub-cellular structures to the tissue scale.

1.3 Phenomenology of germband extension

The *germband extension* (GBE) is an example of tissue morphogenesis that occurs during the development of *Drosophila melanogaster* embryo. It starts in *stage 6* of drosophila development, shortly after the beginning of gastrulation process and continues for approximately 2 hours upto *stage 8* [5]. In this section we describe the features of germband extension at the scale of tissue, cell and sub-cellular structures.

To proceed further we need to clearly illustrate the geometry of the germband tissue and its cells .

- At the beginning of GBE, the length and width of germband tissue are defined

along anterior-posterior axis and dorsal-ventral axis respectively (see Fig. 1.3 a).

- Germband cells are of columnar geometry with polygonal cross-section[30]. *apical* and *basal* side of a cell refer to the cell surfaces towards the outside and inside of the embryo respectively (see Fig. 1.3 b).

- In the apical side of the cell, the two junctions oriented along dorsal-ventral axis are called *vertical junctions* and the other four junctions are called *transverse junctions* [6] (see Fig. 1.3 c).

- We shall refer the central portion of the apical cell-surface as *medial region* and the region near the vertical junction is referred as *junctional region* [12] (see Fig. 1.3 c).

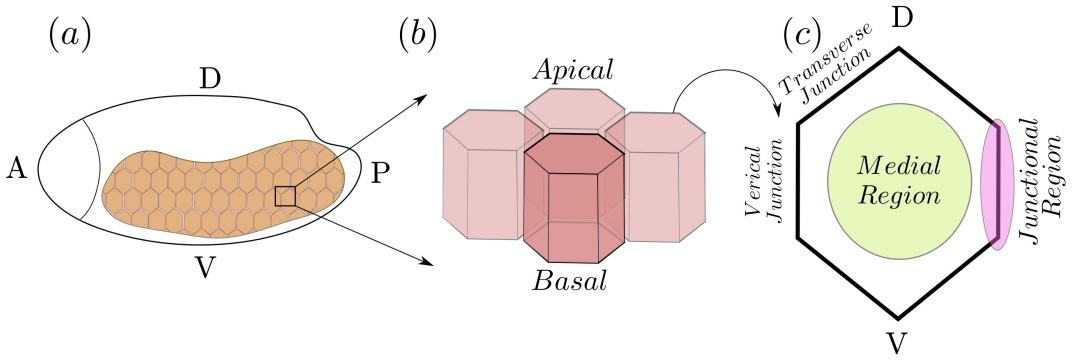

Figure 1.3. Geometry of the germband tissue and the constituent cells : (a) The germband is a part of the epithelial tissue of the drosophila embryo comprising the gnathal, thoracic, and abdominal segments [5]. The letters A-P and D-V represent the Anterior-Posterior and Dorsal-Ventral axis (lab frame of the embryo) respectively. (b) The cells in germband tissue are of polygonal-columnar shape and they adhere to each other to form the tissue. (c) The cells has polygonal cross section and most of the *activity* during intercalation has been seen near the apical surface of the cell [3, 12]. We define geometry of the apical surface : The two junctions oriented along dorsal-ventral axis are called *vertical junctions* and the other four junctions are called *transverse junctions*. The central portion of the apical cell-surface is called *medial region* and the region near the vertical junctions are referred as *junctional region*.

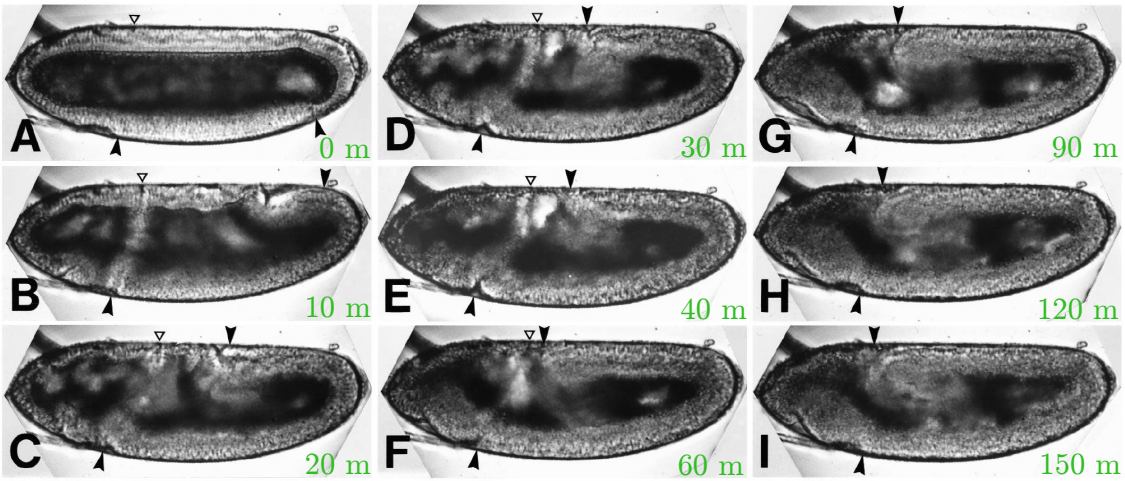

Figure 1.4. Germband extension in *Drosophila melanogaster*. Black arrows mark the anterior-posterior boundaries of the germband tissue at the given time (in green). The overall elongation of the tissue is clearly visible in this figure [5]

1.3.1 Convergence-Extension of tissue

During GBE the tissue increases in length (about 250 % of its initial length [5]) along anterior-posterior axis and simultaneously it gets shortened along dorsal-ventral axis (see Fig.1.4 and Fig. 1.5). It is important to note that during GBE, the germband tissue remodels without any cell divisions [5] and overall shape (polygonal) of the cells remain similar before and after GBE. To attain this simultaneous extension and convergence of the tissue, cells undergo active rearrangements [5] (see Fig. 1.5) where individual cells in germband region go through a topological transition process of exchanging neighbours called *cellular intercalation* (see Fig. 1.6). Due to the planar polarity in the germband cells only the vertical junctions undergo intercalation [7, 12]. Through this intercalation, the number of cells along anterior-posterior direction increases while number of cells along dorsal-ventral direction decreases [5] to give rise to the above described overall shape change in the tissue.

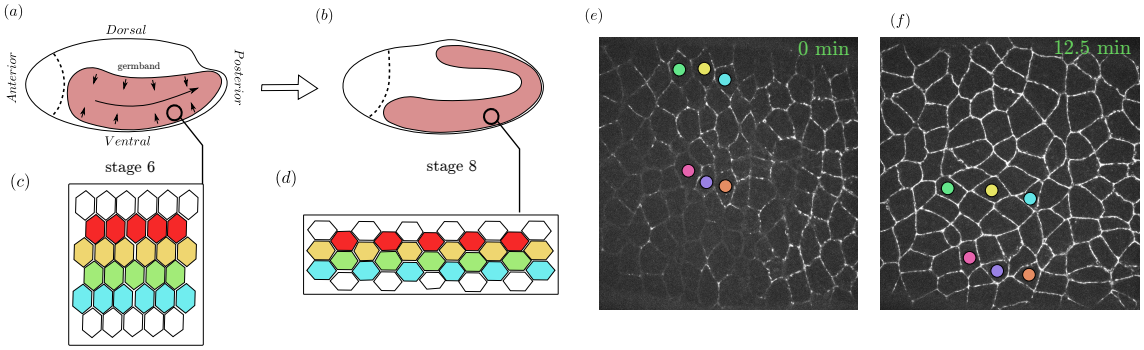

Figure 1.5. Convergence-extension through cellular rearrangements : The germband tissue at (a) the beginning of GBE and (b) at the end of the process. Through GBE the tissue gets extended along anterior-posterior axis and simultaneously it gets shortened along dorsal-ventral axis. This shape change in the tissue is a collective effects of cellular rearrangements where (c) the cells along the dorsal-ventral axis reorient themselves (d) along the anterior-posterior axis. This happens through cellular intercalation. (e-f) Images of germband cells with florescent E-cadherin show rearrangements of two groups of cells during a time lapse of $12m\,30s$.

Next we discuss *cellular intercalation* in detail to understand how each cell goes through this process of neighbour exchange.

1.3.2 Cellular intercalation

Cellular intercalation is a process where neighbouring cells change their co-ordination (by exchanging places) with each other while keeping tissue integrity intact [3]. There are several types of intercalation processes but intercalation seen during GBE in drosophila, is a mediolateral intercalation [3] where cells exchange places with other cells on the same plane. Germband cells mostly intercalate between their dorsal and ventral neighbours [5]. This preferential intercalation direction (due to planar polarity in germband cells) is important for successful elongation of the tissue [7, 12].

The cellular intercalation process starts with the shrinkage of a *vertical junction* (junction oriented along dorsal-ventral axis) followed by reorientation of the junction along a direction which is orthogonal with respect to the shrinkage direction (i.e. along anterior-posterior axis) and subsequent elongation of this reoriented junction (see Fig. 1.6 a). The above said reorientation of the junction results in co-ordination change between the neighbouring cells (see Fig. 1.6 a,b).

Cellular intercalation can be thought of as the unit of "change" which is occurring locally at cell scale through mechanical and chemical processes happening at cellular and sub-cellular scale. The integrated effect of this local change is driving the remodeling of the whole tissue. Intercalation of the vertical junction in germband cells is also referred as T_1-*process* and we frequently use this term in our study.

- **Cell junction :** In confluent tissue like the germband region in drosophila embryo, neighbouring cells form and maintain adhesive connections with each other and form *cell junctions* [3]. It is very important to maintain and regulate this connectivity to keep the tissue intact and successful completion of various steps of embryogenesis depends on it [3, 12]. The adhesive connections can be of various types which play specific important roles in the cell. Here we mainly focus on *adherens junctions* and the main component of the adherens junction is the adhesive molecule called *cadherin*. Details of cadherin dynamics and its involvement in intercalation will be discussed later. From here on "junction" shall refer to adherens junction unless specified otherwise.

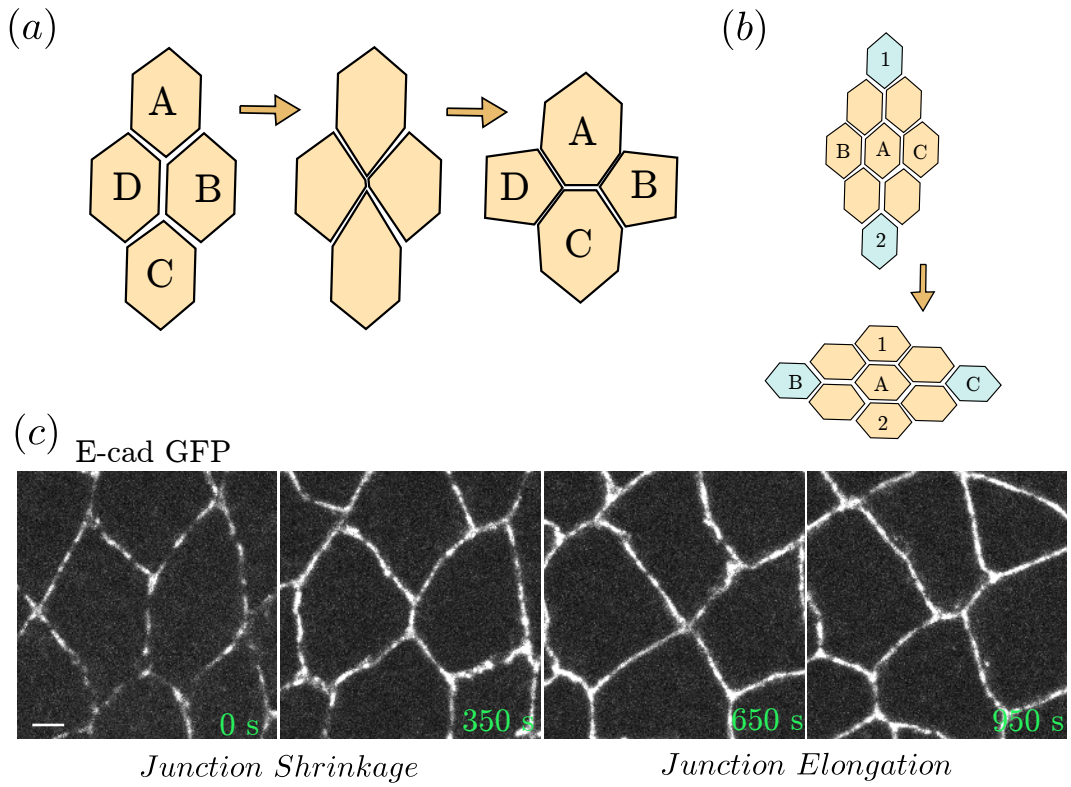

Figure 1.6. Intercalation process and neighbour exchange in germband tissue : (a) During intercalation of a junction (here between the "B" and "D" cell), first it shrinks and then it grows in length after re-orientation of the junction to direction which is perpendicular to the shrinkage direction. (b) A structure of nine cells changes in shape when all of the vertical junctions undergo T_1-transition. "A" exchanges its neighbours "B" and "C" with "1" and "2" during this whole process. (c) Panels show intercalation (shrinkage followed by an elongation) of a vertical junction in germband tissue for a duration of 950 seconds.

Each intercalation event involves regulated remodeling of the cell junction. The shrinkage (of vertical junction) and elongation (of re-oriented junction) occurs irreversibly [3] in a stepwise manner with repeated deformation and subsequent stabilization [12, 11] of the junction, commonly referred as *ratcheting of the cell junction* [11]. This remodeling of cell junction is driven by the local forces generated in subcellular actomyosin network [7] which mechanically couple with the cell junction via E-cadherin. We shall now discuss how the actomyosin dynamics remodel the cell junctions which in turn facilitate the tissue remodeling.

1.3.3 Actomyosin pulsation and flow

The apical actomyosin layer in germband cell is formed by assembly of crosslinked actin filaments and myosin minifilaments [12] and regulated by various mechano-chemical processes [11]. The dynamics of the actomyosin is localized near apical surface of the germband cells (*apico-basal polarity* [3]). This apical actomyosin network plays a critical role in driving the intercalation process through active contractile stress generation [7, 12]. Due to the apico-basal polarity of actomyosin activity in the germband cells, we consider the apical surface of the cell to be a planar representation of the cell. On top of the apico-basal polarity the germband cells also show another polarity on the plane of the tissue in terms of actomyosin organization and cell adhesion strength [3, 12], referred as the *planar polarity*. This planar polarity dictates the orientation of intercalation events and results in selective remodeling of vertical junctions.

Actomyosin dynamics starts with nucleation of small actomyosin rich regions in the medial region of the cell and then they subsequently grow and coalesce together to form a large actomyosin rich region[12]. This large actomyosin rich region then flows towards one of the vertical junctions and it gets disintegrated near the junction. This aggregation and disintegration of actomyosin occurs in a periodic manner and referred as *actomyosin pulsation*, while the movement of actomyosin rich region towards vertical junction is referred as *actomyosin flow* (see Fig. 1.7 a). This periodic pulsation and subsequent flow shrinks the vertical junctions irreversibly when it reaches the junctional region in a roughly step-wise manner [12] and thus drives the cellular intercalation process (see Fig. 1.7 d).

Developing a theoretical description in terms of the main elements of apical actomyosin network to understand the dynamics of pulsation and flow and the dynamics of junction remodeling during cellular intercalation is theme of this thesis.

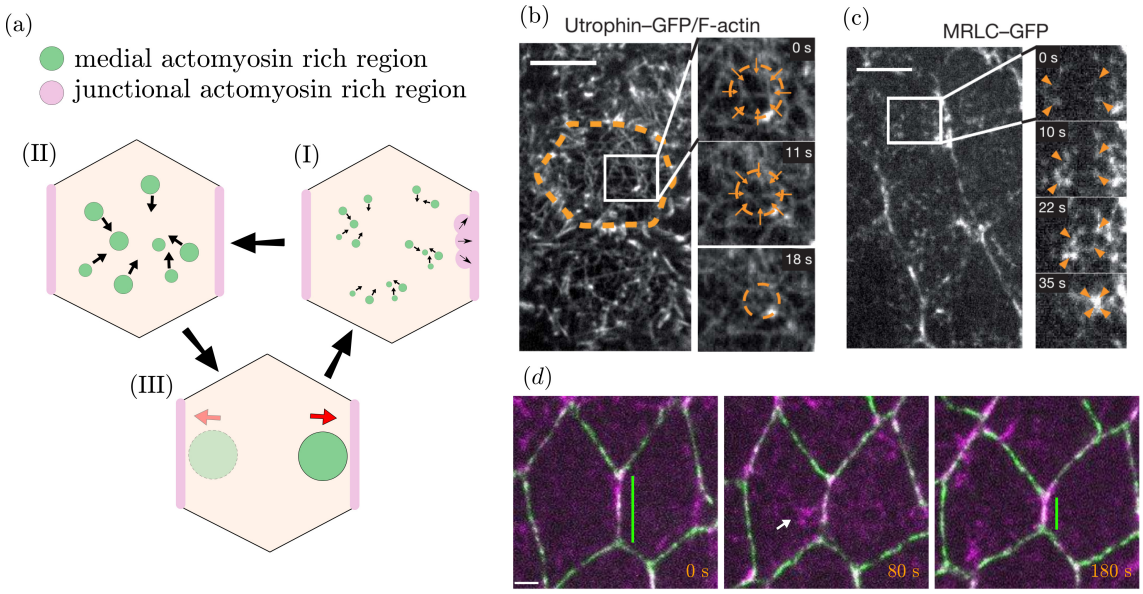

Figure 1.7. Dynamics of actomyosin network in the apical surface of germband cells drive the intercalation process : (a) Actomyosin dynamics starts with (I) nucleation of small actomyosin rich regions in the medial region of the cell and (II) then they subsequently grow and coalesce together to form a large actomyosin rich region. (III) This large actomyosin rich region then flows towards one of the vertical junctions and it gets disintegrated near the junction. This aggregation and disintegration of actomyosin occurs in a periodic manner and referred as *actomyosin pulsation*, while the movement of actomyosin rich region towards vertical junction is referred as *actomyosin flow*. Fluorescently labeled (b) filamentous actin and (c) myosin minifilaments show the formation of actomyosin rich region. (d) This periodic pulsation and subsequent flow (arrow) of actomyosin shrinks the vertical junctions irreversibly when it reaches in junctional region. Fluorescently tagged myosin (magenta) shows a pulse-flow shrinking a junction seen in fluorescently tagged E-cadherin (green).

We consider *actin, myosin* and *cadherin* to be the main components of the actomyosin network. Hence we provide brief introduction to these important constituent elements.

- **Actin :** Actin is one major component of actomyosin network in eukaryotic cells. The monomeric form of actin is known as globular actin which polymerizes to form filamentous actin with the length of a few micrometers. In cytoskeletal structures mainly two types of actin assemblies are found actin bundles and actin networks. These assemblies are formed by crosslinking proteins which can bind with actin filaments and regulated through various

mechano-chemical processes. Proper regulation of crosslinked actin network in germband cells has been found to be important for pulsation and flow.

- **Myosin :** Myosin is a molecular motor capable of producing force (as a force dipole) by using chemically stored energy through ATP-hydrolysis. There are many types of myosin motors with different builds and functionalities but here we only consider the non-muscle $myosin - II$. Myosin can self assemble to create myosin minifilament and it has been found to be the main local force generator in actomyosin inside germband cells. Myosin can bind to actin filaments and it produces contractile stresses in actomyosin network.

- **Cadherin :** Cadherin (named from "calcium-dependent adhesion") is a transmembrane adhesive protein. Cadherins are the main elements of an adherens junction which is formed between cells. There are many kind of cadherin molecules but in this study we only refer to the epithelial cadherin or *E-cadherin*. E-cadherin molecules can interact with actin filaments via linker proteins like catenin. On the cell membrane E-cadherin molecules can form two types of chemical bonding with other E-cadherin molecules, (i)*trans-bond*, when they bind to the cadherin from membrane of a neighbouring cell and (ii) *cis-bond*, when they bind with cadherin from the same membrane. E-cadherin plays a very important role in cell-cell force transduction and it is strongly coupled with the actomyosin network.

1.4 Hydrodynamics

Hydrodynamics refers to a coarse-grained description of the system in terms of its *slow* variables. Temporal dynamics of these variables at long length scale is much slower compared to the inter-particle collision or elementary excitation relaxation timescales. Hence the dynamics of hydrodynamic variables can be treated as perturbations from the thermodynamic equilibrium as any spatial point is near thermodynamic equilibrium at any given instant. Densities of conserved quantities and broken-symmetry elastic variables show such slow dynamics and therefore are identified as hydrodynamic variables. Historically hydrodynamics started with the study of water in terms of mass, momentum and energy densities as hydrodynamic

variables as these quantities follow the respective conservation laws. Since then hydrodynamics has been extensively used to understand fluids, elastic solids, liquid crystals, spin systems and many other problems.

Hydrodynamic framework has been used for several decades now to understand active matter systems such as active colloidal suspensions [27], dry flocks [22], active gel [24], active nematic liquid [28] and so on. Many seminal works paved the way for understanding the physics of living matter using hydrodynamic framework. It has been successfully used to understand the physics of many fascinating phenomena observed *in vivo* inside living cells, tissues or *in vitro* studies of motility assays and reconstituted actomyosin systems.

In this study we shall use the hydrodynamic description to understand the dynamics of active elastomer network which is described in detail in a later chapter.

1.5 Layout of this thesis

In this thesis we develop an active hydrodynamic framework to understand the subcellular dynamics of actomyosin during intercalation and we derive a dynamical systems description for cell junction to understand the stepwise shrinkage("ratcheting") of junction length during germband extension.

- In chapter 2, we discuss an active nonlinear spring model to understand the overall pulsatile behaviour of actomyosin in the cell and state the need for a hydrodynamic description for actomyosin dynamics inside the cell to understand the rich spatiotemporal behaviour observed during tissue morphogenesis.

- In chapter 3 and chapter 4, First we emphasis the existence of various dynamical regimes in actomyosin dynamics and propose an active elastomer description for actomyosin with turnover of its components. We start with a hydrodynamic description for actomyosin network as an elastomer with turnover of force generators: affine theory. We show that this description can capture the essential features of actomyosin dynamics in germband cells and make important predictions about the dynamics seen *in vivo* and verify qualitative aspects through analysis of experimental data.

- In chapter 5, we discuss the regime of the validity and applicability of the affine description and we present an alternative description for actomyosin as a transient network and discuss a preliminary theory which accommodates *nonaffine deformations* through turnover of the network components.
- In chapter 6, we derive a dynamical systems description for cell junctions starting from a coarse-grained field description and show that this dynamical description is able to capture the essential features of the junction remodeling including the "ratcheting" that happens during intercalation. We further explore the reliability and robustness of the ratcheting dynamics against perturbations and propose a possible mechanism to incorporate robustness through the self sustained actomyosin pulsation and flow already present in the germband cells.

End of Chapter

Chapter 2

Dynamics of apical actomyosin as an active nonlinear spring

2.1 Introduction

Periodic density variation or *pulsation* has been seen in apical actomyosin layer inside cells which are undergoing local shape/size changes leading to tissue morphogenesis. Examples of such events include apical constriction during dorsal closure [8, 32, 33, 34] (see Fig. 2.1) and cellular intercalation during germband extension [12, 84, 11, 37] (see Fig. 2.2) in embryogenesis of *Drosophila melanogaster*. Pulsation of actomyosin plays vital role in driving the mechanics of tissue remodeling through production of local contractile forces [31, 12].

The main purpose of this thesis is to develop a hydrodynamic theory to understand actomyosin dynamics during tissue morphogenesis. But before we delve into a hydrodynamic description of actomyosin network, in this chapter we shall describe the temporal behaviour of the apical actomyosin network in terms of a simple zero dimensional mechanical model. We consider the apical layer of actomyosin as a viscoelastic element with an active contractile stress generating machinery. We shall show that this minimal description is able to capture the feature of actomyosin pulsation as spontaneous oscillations in density and shape driven by local active contractile forces.

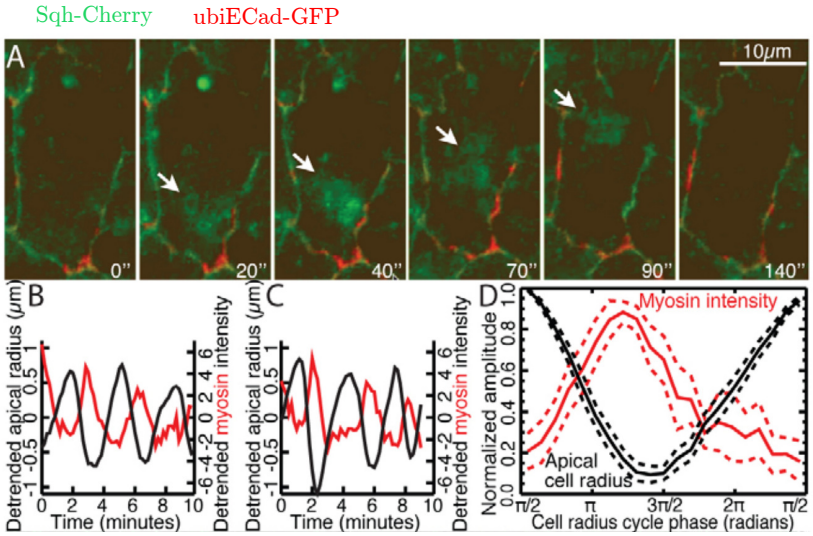

Figure 2.1. Dorsal closure in *Drosophila melanogaster* : (A) Fluorescent microscopy images of myosin in green and E-cadherin in red, showing contraction (during 0-90 seconds) and expansion (during 90-140 seconds) during the early phase of dorsal closure. The white arrow traces movement of a myosin rich region during contraction of cell area (B,C) Temporal dynamics of cell radius (black line) and medial myosin intensity (red line) during dorsal closure in two sample cells. (D) Overall dynamics of normalised cell radius (black line) and medial myosin (red line) for many cycles calculated in cells from multiple embryos. The result presents cell size change is in phase with the pulsation in medial myosin. Image courtesy [34].

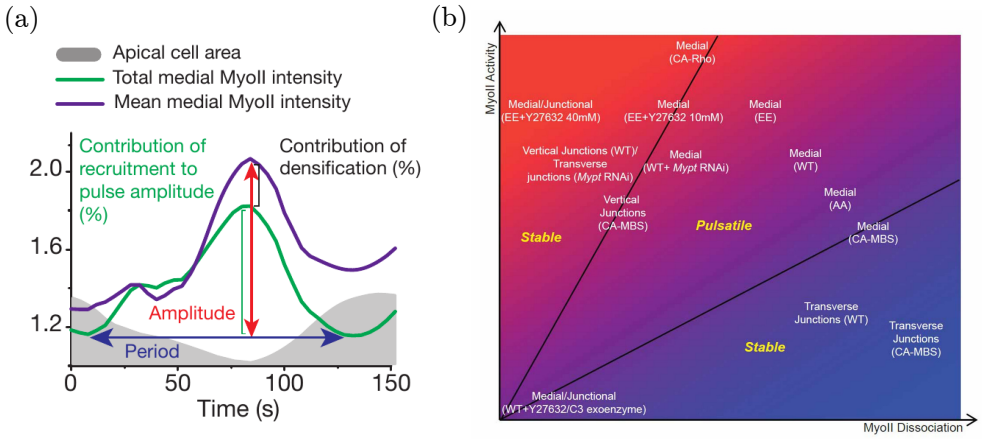

Figure 2.2. (a) Study of the cell average of apical myosin and cell area show correlated area oscillation with myosin density oscillation during actomyosin pulsation. (b) A qualitative phase diagram in myosin activity and myosin dissociation rate shows pulsatile behaviour. Image courtesy [11].

2.2 Description of the active nonlinear spring

The main ingredients of this minimal model of actomyosin are an elastic element and a viscous or dissipative element connected in parallel with the elastic element and active contractile stress generators where the amount of stress depends on the density of the stress generator molecules (myosin motors) which undergo turnover with binding and unbinding rates given by k_b and k_u respectively (Fig.2.3). These three elements constitute the description of medial actomyosin network and this network is connected to two elastic elements at the boundary representing the anchorage of actomyosin network with the cell boundary via cadherin coplexes. This description bears some similarity with the work presented in Solon et al. [49] where an active Kelvin-Voigt like model was used to study apical cell area oscillations during dorsal closure.

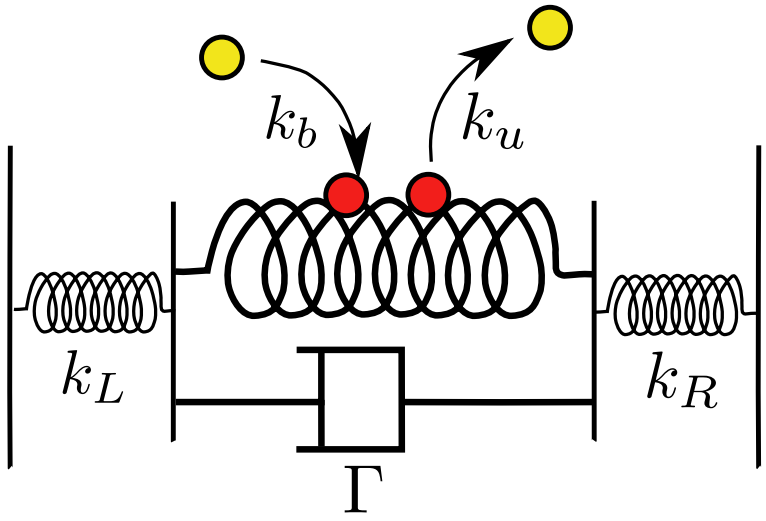

Figure 2.3. Schematic diagram of the active nonlinear spring: The active stress depends on instantaneous density of bound myosin motors (red circle) which is regulated by binding (with rate k_b) and unbindin (with rate k_u) processes. The dissipative element has viscosity Γ and the stiffness of the left and right boundary springs are given by k_L and k_R respectively.

Now we state the equation of motion for this active nonlinear spring in the next section.

2.3 Equation of motion

The variables of interest here is the length of the elastic element ($l(t)$) and density of bound myosin ($\rho_b(t)$). The force balance in over-damped limit (i.e., ignoring inertia) reduces to the balance between internal stresses which gives the dynamics of $l(t)$ as

$$\Gamma \frac{dl}{dt} = \sigma^e + \sigma^a \,. \tag{2.1}$$

The myosin motors go through turnover as stated earlier. The total amount of bound myosin is conserved in absence of turnover which brings us the condition $\frac{d}{dt}(l\rho_b) = 0$ for k_b, $k_u = 0$. This condition explains the last term on the right in the myosin density equation, given by

$$\frac{d\rho_b}{dt} = -k_u \rho_b + k_b - \frac{\rho_b}{l}\frac{dl}{dt} \,. \tag{2.2}$$

Here the unbinding of motors depends on the density of bound motors ($\propto \rho_b$) and we consider a constant binding of unbound motors (assuming a pool of unbound myosins). As we have already mentioned the total amount of bound myosin ($l\rho_b$) only changes by turnover.

In Eq.2.1 σ^e and σ^a stand for elastic stress and active stress respectively. We consider contribution from higher order elastic terms in the elastic free energy up to quartic order here. This nonlinearity in elastic stress is important to stabilize oscillatory behaviour in the system. The active stress can be the origin of this stabilizing effect and we discuss this in details in a later chapter. The elastic stress here has the following form :

$$\sigma^e = -k_1(l - l_0) - k_2(l - l_0)^2 - k_3(l - l_0)^3 + \sigma_L + \sigma_R \,. \tag{2.3}$$

Here σ_L and σ_R stand for elastic stresses from the left and right boundary elements respectively and l_0 and k_1, k_2, k_3 are the rest length for the elastic element and its stiffness constants respectively. The stresses from the boundary elastic elements are

$$\sigma_L = -k_L(l_L - l_{L0})$$
$$\sigma_R = -k_R(l_R - l_{R0})\,.$$

Here $k_{L,R}$, $l_{L,R}$ and $l_{L0,R0}$ are the stiffness, instantaneous length and rest length of the left and right boundary elements respectively. In further discussions we take $k_{L,R} = k$ and $l_{L0,R0} = l_0$ for simplicity.

The active stress (σ^a) generated in the active contractile element depends on the density of the force generating motors (ρ_b) and given by the following relationship,

$$\sigma^a = -\zeta_1 \Delta\mu(\rho_b - \rho_{b0})\,. \tag{2.4}$$

Where $\zeta_1 < 0$ for contractile active stress, ρ_{b0} is the steady state myosin density and $\Delta\mu$ is the change in free energy (chemical potential) during the process which facilitate the active stress generation in molecular motors. We shall discuss the concept of active stress in more details in coming chapters.

Now simplifying the equation of motion (Eq. 2.1 and Eq. 2.2) and writing them in dimensionless form in terms of $\frac{l}{l_0}$ and $\frac{\rho_b}{\rho_{b0}}$ we get

$$\frac{\Gamma}{k_1 k_b}\frac{d}{dt}(\frac{l}{l_0}) = (\frac{k}{k_1}-1)(\frac{l}{l_0}-1) - \frac{k_2 l_0}{k_1}(\frac{l}{l_0}-1)^2 - \frac{k_3 l_0^2}{k_1}(\frac{l}{l_0}-1)^3 + \frac{\zeta_1 \Delta\mu \rho_{b0}}{k_1 l_0}(\frac{\rho_b}{\rho_{b0}}-1) \tag{2.5}$$

and

$$\frac{d}{dt}(\frac{\rho_b}{\rho_{b0}}) = -(\frac{k_u}{k_b}(\frac{\rho_b}{\rho_{b0}}) - 1) - \frac{\frac{l}{l_0}}{(\frac{\rho_b}{\rho_{b0}})}\frac{d}{dt}(\frac{l}{l_0}) \tag{2.6}$$

We numerically solve the resulting equations and present the results in the next section.

2.4 Spontaneous oscillations and contractile instability

For small values of contractile stress ($\frac{\zeta_1 \Delta\mu \rho_{b0}}{k_1 l_0}$) the system relaxes to an unstrained state given by $l = l_0$ in steady state (Fig. 2.4a) but as we increase contractile stress we encounter oscillatory solutions (Fig. 2.4c) and finally at very high values (compared

to the stiffness values) of contractile stresses the system encounter a contractile instability (Fig. 2.4b). The oscillatory solution here is an emergent feature and a result of active forces exerted by the myosin motors. Any increase in myosin density further contracts the system and result in further increase in myosin density this positive feedback is balanced by the turnover of myosin which always tries to keep the myosin density in the steady state and these two competing effects gives rise to the oscillation in the bound myosin density and deformation of the system.

A phase diagram (Fig. 2.5) constructed in $\frac{k}{k_1}$ vs $\frac{-\zeta_1 \Delta\mu\rho_{b0}}{k_1 l_0}$ space shows the three phases discussed above. The already discussed effects of increasing contractile stress are evident from the phase diagram. Additionally we can also see the expected result- stabilization of instability and oscillatory behaviour to a stable unstrained state with increasing stiffness.

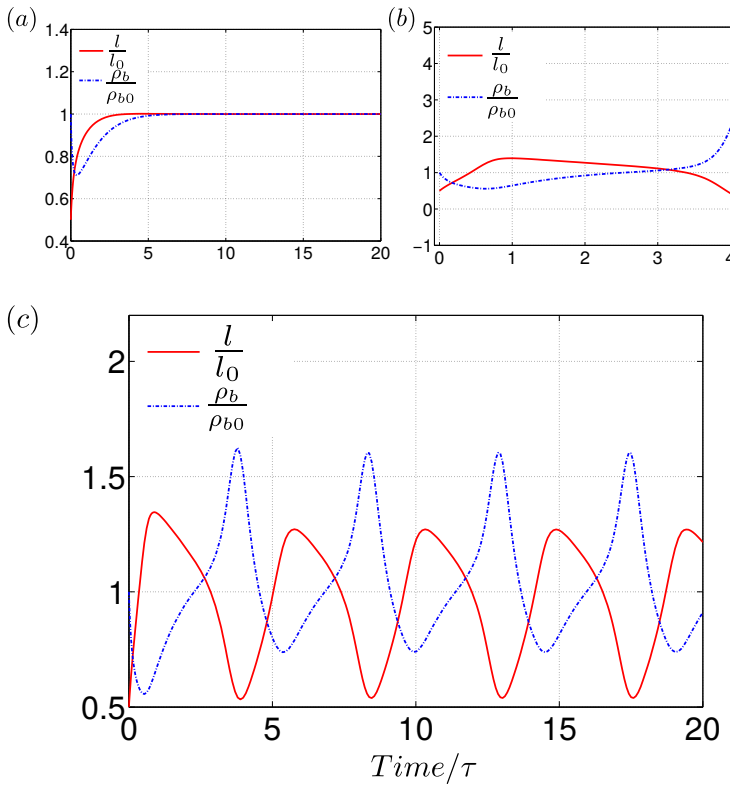

Figure 2.4. Spontaneous oscillation and contractile instability in active viscoelastic spring dynamics : Oscillatory and unstable solutions emerge as we increase the renormalized contractile stress ($\frac{\zeta_1 \Delta\mu\rho_{b0}}{k_1 l_0}$). (a) The unstrained state is stable at a low contractile stress $\frac{-\zeta_1 \Delta\mu\rho_{b0}}{k_1 l_0} = 0.1$ (b) the system encounter contractile instability for high values of contractile stress $\frac{-\zeta_1 \Delta\mu\rho_{b0}}{k_1 l_0} = 5.0$ (c) in the medium range, $\frac{-\zeta_1 \Delta\mu\rho_{b0}}{k_1 l_0} = 3.0$ we observe oscillatory solutions. For (a-c) the other parameters are kept constant at $\frac{\Gamma}{k_1 k_b} = 1$, $(\frac{k}{k_1} - 1) = 1$, $\frac{k_2 l_0}{k_1} = 1$, $\frac{k_3 l_0^2}{k_1} = 15$ and $\frac{k_u}{k_b} = 1$.

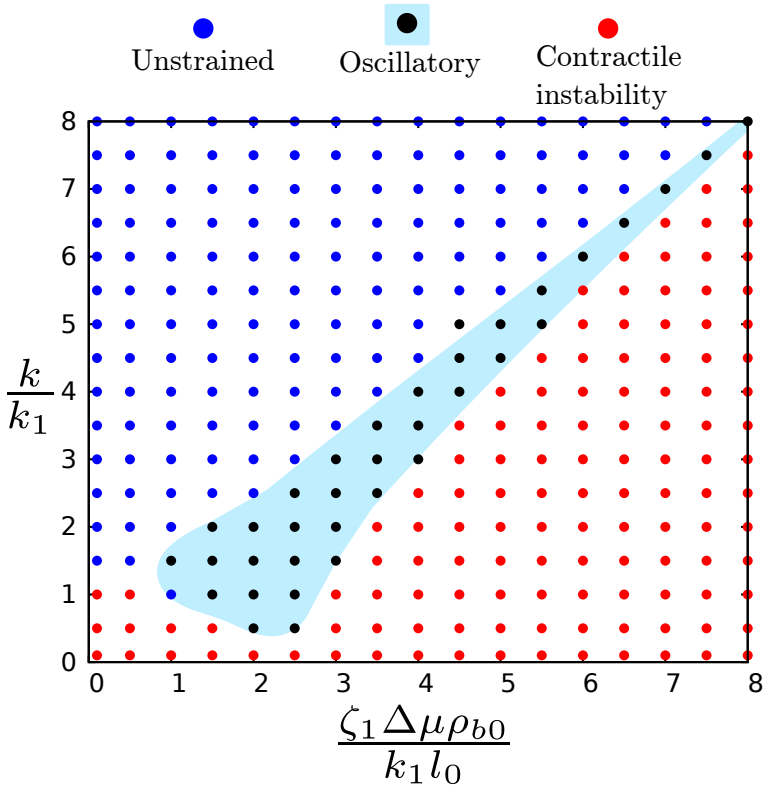

Figure 2.5. Phase diagram in renormalized contractile stress ($\frac{-\zeta_1 \Delta\mu\rho_{b0}}{k_1 l_0}$) and stiffness ratio ($\frac{k}{k_1}$) : Shows the unstrained stable state (blue dots), oscillatory state (black dots, blue shade) and the contractile instability (red dots). Other renormalized parameters was taken to be $\frac{\Gamma}{k_1 k_b} = 1$, $\frac{k_2 l_0}{k_1} = 1$, $\frac{k_3 l_0^2}{k_1} = 15$ and k_u, $k_b = 1$.

2.5 Need for a hydrodynamic description

This simple active nonlinear spring description of actomyosin network in the cell shows the emergence of sustained oscillations. This periodic solutions are spontaneously generated without any external drive and will not emerge in absence of active contractile forces generated by the molecular motors. Though this description has been used as a preliminary means to understand the cell area oscillation during dorsal closure in [49], it cannot explain the complex spatio-temporal features seen in the actomyosin dynamics in various tissue remodeling events during development. Thus to adequately describe the dynamics of apical actomyosin network, as we aim to, a continuum description will be necessary. We dedicate the next few chapters to develop an active hydrodynamic description for the actomyosin network.

End of Chapter

Chapter 3

Hydrodynamics of apical actomyosin as an active elastomer : Affine description

3.1 Different regimes of actomyosin dynamics during tissue morphogenesis

Before we start building up a theoretical description for actomyosin dynamics it is important to understand the different length scales and timescales involved in the actomyosin dynamics. A closer look into the experimental movies [73, 12, 11] will reveal an early time (0-5 s) nucleation of small actomyosin speckles (Fig.3.1) that grow in size with time and start moving in a timescale of 10-20 s (Fig.3.1). These medium sized actomyosin rich regions then coalesce to form large actomyosin rich region(s). This formation of the large high density actomyosin rich region happens in a timescale of 30-50 s (Fig.3.1) and this results in actomyosin pulsation at 50-80 s [12, 11](Fig.3.1).

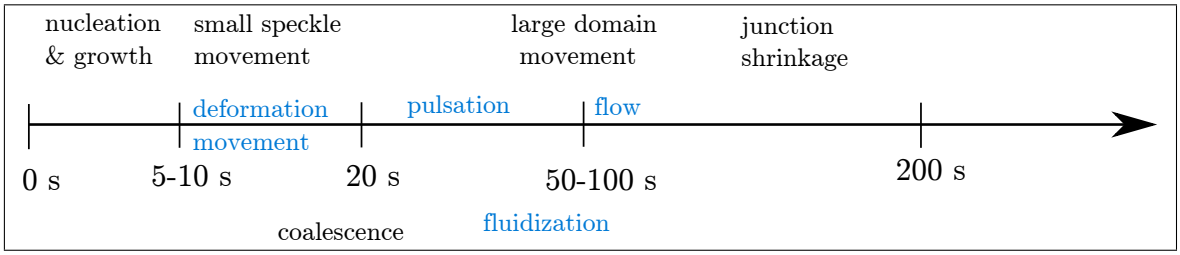

Figure 3.1. Different dynamical regimes in apical actomyosin dynamics in germband cell spans from early time elastomeric behaviour to the longer time fluid-like behaviour.

Fluorescence recovery after photo-bleaching(FRAP) measurements in germband cells, reveal an actin turnover time of around 10-20 s [12] and a myosin turnover timescale of 5-10 s [11]. These timescales are similar to the early time nucleation-growth and coalescence of actomyosin. Further in time the large actomyosin rich regions start moving giving rise to actomyosin flow in a timescale $\sim 100\,s$ [12, 11]. This actomyosin flow towards a vertical junction results in junction remodeling in a timescale of $120-150\,s$ [12, 85]. Thus the existence of different dynamical regimes in actomyosin dynamics in germband cells during tissue morphogenesis becomes clear.

This suggests that the appropriate description should span the short-time elastomeric and the longer time fluid-like regimes. We start our study of actomyosin network with an elastic description of the network, where the local deformations induced by myosin binding and release are affine. Increased myosin binding can lead to rapid turnover of actin and crosslinkers, resulting in loss of network integrity and its fluidization via intranetwork flows; we study this crossover to a nonaffine regime later in Chapter.5.

3.2 Hydrodynamic description of actomyosin

In this section we describe apical actomyosin network in germband cell as an active elastomer embedded in a viscous fluid and we build up a hydrodynamic description of the active elastomer from symmetry principles and introducing minimal phenomenologically inspired inputs. The elements of the active elastomer are conceived from the constituents of the actomyosin network. Then the *slow* variables are identified that describe the long time-large length scale dynamics of the elements of active elastomer. The active hydrodynamics description has been proposed in terms of these slow variables.

Later in this chapter we investigate the temporal behaviour of active elastomer using various approximate methods described in details in the respective sections.

3.2.1 Elements of the theory

The main elements of the actomyosin network considered here are the cross-linked f-actin network, myosin minifilaments which can bind to this network and exert contractile forces and finally the cytosol in which this actomyosin network is immersed

(see Fig. 3.2). Finally the actomyosin network is attached to the cadherin in cell boundary via linker proteins. Below we discuss the essential physical aspects of these constituents and how the active elastomer elements are conceived from these.

- We describe the cross-linked actin network as an elastomer network in the regime where active contractile forces are low. In this low active force limit the co-ordination of the elastomer network does not change over time ,i.e., the crosslinkers in actomyosin network do not undergo turnover. Thus the local deformation in the elastomer is considered to be homogeneous or *affine*. The hydrodynamic variables those describe this elastomer network are density of the network, $\rho(\boldsymbol{x}, t)$ and the displacement field of the network, $\boldsymbol{u}(\boldsymbol{x}, t)$.

- The non-muscle myosin minifilaments are the active force generators as they produce contractile forces when they are bound to the crosslinked actin network. The hydrodynamic variable used to describe myosin dynamics is the density of bound myosin, $\rho_b(\boldsymbol{x}, t)$ and unbound myosin, $\rho_u(\boldsymbol{x}, t)$.

- The cytosol is a highly viscous fluid in which the actomyosin network remains immersed. The appropriate hydrodynamic variables to describe this viscous fluid will arise from the mass and momentum conservation and those are the density, $\rho_f(\boldsymbol{x}, t)$ and velocity, $\boldsymbol{v}_f(\boldsymbol{x}, t)$ of the fluid respectively.

- The cadherin complexes are adhesive molecules that hold on to the actomyosin network. The cadherin population can be described by the density $\rho_{cad}(\boldsymbol{x}, t)$.

Here we consider affine deformations of crosslinked actin network in the timescale of the actomyosin dynamics. We describe a theory for *non-affine* elastomer allowing network turnover in a later chapter.

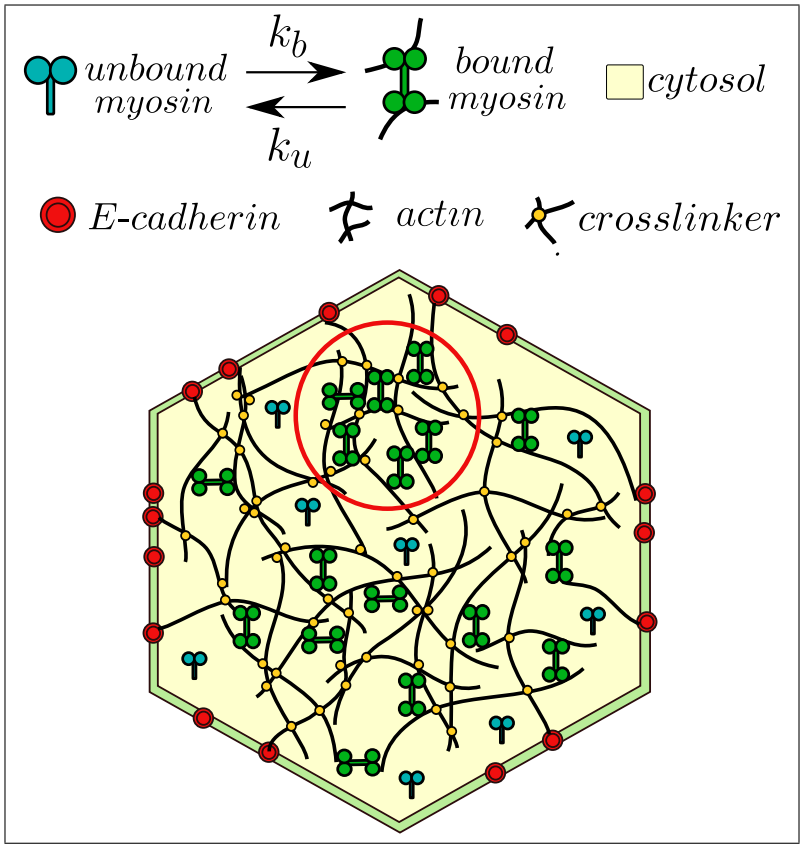

Figure 3.2. Schematic diagram to illustrate the main components of the active elastomer. Crosslinked actin network is attached to the cell boundaries by adhesive molecules like cadherin. The myosin minifilaments can bind (with rate k_b) to the network and unbind (with rate k_u) from it and exert contractile forces while they are in the bound state. This whole actomyosin network is immersed in the highly viscous fluid cytosol.

3.2.2 Dynamics of elastomer network

The elastomer network, conceptualized as a filament network crosslinked by *passive* crosslinker proteins, is described by the density $\rho(\boldsymbol{x}, t)$ and the displacement field $\boldsymbol{u}(\boldsymbol{x}, t)$. These quantities represent a coarse grained picture of the elastomer network at a length scale much larger than the mesh size (average distance between two crosslinking sites).

The force balance relation (Eq. 3.1) which dictates the spatial and temporal evolution of the displacement field $\boldsymbol{u}(\boldsymbol{x}, t)$ is given by

$$\rho\ddot{\boldsymbol{u}} + \Gamma(\dot{\boldsymbol{u}} - \boldsymbol{v}_f) = \boldsymbol{\nabla}\cdot(\boldsymbol{\sigma})\,. \tag{3.1}$$

Here $\boldsymbol{\sigma}$ is the total internal stress and Γ is the friction coefficient for the frictional force which acts upon the elastomer whenever there is a relative motion ($\dot{\boldsymbol{u}} - \boldsymbol{v}_f \neq 0$) with respect to the surrounding viscous fluid. The friction Γ between the mesh and cytosol can in principle depend on the mesh density. Later in this section we define the total stress $\boldsymbol{\sigma}$ in terms of internal stresses in details.

The network density $\rho(\boldsymbol{x}, t)$ dynamics (Eq. 3.2) is described here by taking into account the changes in density caused by advection, permeation and actin turnover :

$$\dot{\rho} + \boldsymbol{\nabla}\cdot(\rho\dot{\boldsymbol{u}}) = \mathcal{M}\nabla^2\frac{\delta F}{\delta\rho} + \mathcal{S}_a\,. \tag{3.2}$$

Here the actin turnover is given by $\mathcal{S}_a = (k_+ - k_-\rho)$ where k_+ and k_- are the binding and unbinding rates respectively. Permeation happens with mobility $\mathcal{M}$. We discuss the detailed form of free energy functional $F(\rho, \boldsymbol{u}, \ldots)$ later in this section.

3.2.3 Dynamics of active force generators

The myosin minifilaments play major role in producing contractile forces in actomyosin network of germband cells and conceived as active force generators in the active elastomer description. The myosin, while bound to the mesh, gets advected by local velocity field ($\dot{\boldsymbol{u}}$) of the elastomer network and diffuse on the network with a diffusion constant D. Unbound myosin diffuses through the medium with diffusivity D_u. The turnover of myosin is described by the term $\mathcal{S}_m$ while total amount of myosin ($\rho_b + \rho_u$) remains conserved. The resulting equations for bound and unbound myosin with the above described dynamics are given by

$$\begin{aligned}
\dot{\rho_b} + \boldsymbol{\nabla}\cdot(\rho_b\dot{\boldsymbol{u}}) &= D\boldsymbol{\nabla}^2\rho_b + \mathcal{S}_m \\
\dot{\rho_u} + \boldsymbol{\nabla}\cdot(\rho_u\boldsymbol{v}_f) &= D_u\boldsymbol{\nabla}^2\rho_u - \mathcal{S}_m\,.
\end{aligned} \tag{3.3}$$

We unfold the source term $\mathcal{S}_m$ later in this chapter.

3.2.4 Dynamics of ambient fluid

The cytosol conceived as a compressible Newtonian fluid with the hydrodynamic description given by the Naviers-Stokes equation as

$$\rho_f(\dot{\boldsymbol{v}}_f + \boldsymbol{v}_f \cdot \boldsymbol{\nabla}\boldsymbol{v}_f) = \eta_f^s \boldsymbol{\nabla}^2 \boldsymbol{v}_f + (\frac{\eta_f^s}{3} + \eta_f^b)\boldsymbol{\nabla}(\boldsymbol{\nabla}\cdot\boldsymbol{v}_f) - \boldsymbol{\nabla}P + \Gamma(\dot{\boldsymbol{u}} - \boldsymbol{v}_f)\,. \quad (3.4)$$

Here P is the pressure, ρ_f is the density and η_f^s and η_f^b are the shear and bulk viscosities of the fluid.

These equations (Eq. 3.1, 3.2, 3.3, 3.4) are the complete set of equations that describe the hydrodynamic description of the active elastomer. We shall further expand them and simplify them as we proceed to treat them with various analytical and numerical methods to understand the spatiotemporal dynamics of active elastomer. The hydrodynamical description discussed here bears resemblance to [45, 46].

3.2.5 Forces and stresses

The total internal stress $\boldsymbol{\sigma}(\boldsymbol{x}, t)$ in the Eq. 3.1 is the sum of the elastic stress ($\boldsymbol{\sigma}^e$), dissipative stress ($\boldsymbol{\sigma}^d$) and active stress ($\boldsymbol{\sigma}^a$) as given by

$$\boldsymbol{\sigma} = \boldsymbol{\sigma}^e + \boldsymbol{\sigma}^a + \boldsymbol{\sigma}^d\,. \quad (3.5)$$

The constitutive relations for the elastic ($\boldsymbol{\sigma}^e$) and dissipative ($\boldsymbol{\sigma}^d$) stresses are given by

$$\begin{aligned} \boldsymbol{\sigma}^e_{ij} &= \frac{\delta F}{\delta u_{ij}} \quad (3.6)\\ &= \left(\lambda + \frac{2\nu}{3}\right)\delta_{ij}\boldsymbol{\nabla}\cdot\boldsymbol{u} + 2\nu\left(\epsilon_{ij} - \frac{1}{3}\delta_{ij}\boldsymbol{\nabla}\cdot\boldsymbol{u}\right)\\ \boldsymbol{\sigma}^d_{ij} &= \eta_b\delta_{ij}\boldsymbol{\nabla}\cdot\dot{\boldsymbol{u}} + 2\eta_s\left(\dot{\epsilon}_{ij} - \frac{1}{3}\delta_{ij}\boldsymbol{\nabla}\cdot\dot{\boldsymbol{u}}\right)\,. \quad (3.7) \end{aligned}$$

Here λ, ν are the bulk and shear Lamé coefficients of the elastic mesh (Eq. 3.8)

and η_b, η_s are the bulk and shear viscosities of the mesh, respectively. F denotes the bulk free energy of the elastomer that governs the equilibrium dynamics of the elastomer and it is defined as $F(\boldsymbol{u}, \rho, \ldots) = \int_r \boldsymbol{dr} f_B$. Here f_B is the free energy density which is given by the following equation :

$$f_B = \frac{1}{2}\left(\lambda \epsilon_{ii}\epsilon_{jj} + 2\nu\epsilon_{ij}\epsilon_{ij}\right) + C\delta\rho\epsilon_{ii} + \frac{A}{2}\delta\rho^2 + \ldots \tag{3.8}$$

Here the linearized elastic strain is defined as $\boldsymbol{\epsilon} = \frac{1}{2}(\nabla\boldsymbol{u} + (\nabla\boldsymbol{u})^T)$ and C and A are positive constant co-efficients which appear in the relationship of mesh density variation and local strain as described in the next section. By taking this form of f_B we assume the isotropic elastic nature for the active elastomer.

The active stress $\boldsymbol{\sigma}^a$ should depend on the density of myosin ρ_b and actin ρ and it should increase with increasing myosin density and then saturate. Thus we find it reasonable to propose the following form :

$$\begin{aligned} \boldsymbol{\sigma}^a &= -\zeta(\rho, \rho_b)\Delta\mu\, \boldsymbol{I} \\ &= -\frac{\zeta_1\rho_b}{1+\zeta_2\rho_b}\chi(\rho)\,\Delta\mu\, \boldsymbol{I}\,. \end{aligned} \tag{3.9}$$

Here $\Delta\mu$ represent the change in chemical potential during *ATP-hydrolysis*, $\zeta(\rho, \rho_b)$ is a function of mesh density and bound myosin density. The parameters ζ_1 and ζ_2 determine how the active stress depends on myosin density and the values $\zeta_1 < 0$ [54], $\zeta_2 > 0$ together with the overall negative sign ensure that the active stress is contractile in nature i.e., active stress creates a local "negative pressure" which draws in surrounding material. Here $\chi(\rho)$ is a smooth, positive function of ρ and I is an identity matrix.

We now expand $\chi(\rho)$ about the steady state mesh density ρ_0 and obtain the following resulting form :

$$\chi(\rho) = \chi(\rho_0) + \chi'(\rho_0)\delta\rho + \frac{1}{2}\chi''(\rho_0)\delta\rho^2 + \ldots\,. \tag{3.10}$$

Now finally rewriting the active stress $\boldsymbol{\sigma}^a$ as a function of ρ and ρ_b in the expanded

form we get :

$$\boldsymbol{\sigma}^a = -\frac{\Delta\mu\zeta_1\rho_b}{1+\zeta_2\rho_b}\left(\chi(\rho_0)+\chi'(\rho_0)\delta\rho+\frac{1}{2}\chi''(\rho_0)\delta\rho^2+\ldots\right)\boldsymbol{I}\,. \tag{3.11}$$

3.3 Resulting equations

With the generic hydrodynamical description of active elastomer we now specify the final set of equations using problem specific considerations and reasonable simplifications as discussed below.

- The cell interior is a dense system with high viscosity. So expecting the elastomer network dynamics to be over-damped, we ignore inertia and drop the $\ddot{\boldsymbol{u}}$ term in Eq. (3.1).

- Here we reemphasize that we take the crosslinks in the elastomer network to be long lived, such that the turnover timescale of the crosslinkers are sufficiently large compared to the timescale of myosin motors turnover and contractile force generation. We shall present a detailed discussion on this crucial assumption later in this thesis but here we consider the above case to be true in low enough contractile stress. Thus in the absence of remodeling of the network co-ordination the local change in the density of elastomer network is slaved by local deformation , given by $\delta\rho \propto -\boldsymbol{\nabla}\cdot\boldsymbol{u}$. The negative sign carries the meaning that local compression (or extension) will condense (or dilute) the local network density.

- With the above discussion in mind we express the mesh density fluctuation by the local compression as $\delta\rho = -c\epsilon_{ii}$ using Eq.3.2 and Eq.3.8. Here c is a positive constant given by $c = \frac{C}{A}$. Now we express the active stress in terms of myosin density and local deformation as

$$\sigma^a = -\frac{\Delta\mu\zeta_1\rho_b}{1+\zeta_2\rho_b}\left(\chi(\rho_0)-c\chi'(\rho_0)\epsilon_{ii}+\frac{1}{2}c^2\chi''(\rho_0)\epsilon_{ii}^2+\ldots\right)\boldsymbol{I}\,. \tag{3.12}$$

- We assume a bath of unbound myosin and only consider the dynamics of the bound myosin density.

- The form of the turnover dynamics which dictates the binding and unbinding of myosin to the elastomer network, has been taken as $\mathcal{S}_m = -k_u(\epsilon)\rho_b + k_b\rho$. This form is obtained considering unbinding is proportional to the bound myosin density ρ_b and binding is more if there is more mesh available (i.e. proportional to ρ).
- We ignore the hydrodynamics of the fluid following Rouse dynamics [53]; this is suggested by experiments that show the actin mesh moves with respect to the fluid, and does not carry (advect) the fluid and other soluble molecules along with it, except for those which are bound to the mesh [11, 12]. Therefore we ignore the dynamics of the fluid (Eq.3.4) and the frictional dissipation in force balance (Eq.3.1) becomes $\Gamma\dot{\boldsymbol{u}}$.

With the above discussed considerations we describe the active elastomer by the dynamics of the displacement field $\boldsymbol{u}(\boldsymbol{x}, t)$ and bound myosin density $\rho_b(\boldsymbol{x}, t)$ given by

$$\Gamma\dot{\boldsymbol{u}} = \boldsymbol{\nabla} \cdot (\boldsymbol{\sigma}^e + \boldsymbol{\sigma}^a + \boldsymbol{\sigma}^d) \tag{3.13}$$

and

$$\dot{\rho_b} + \boldsymbol{\nabla} \cdot (\rho_b \dot{\boldsymbol{u}}) = D\boldsymbol{\nabla}^2\rho_b - k_{u0}e^{\alpha\boldsymbol{\nabla}\cdot\boldsymbol{u}}\rho_b + k_b\rho\,. \tag{3.14}$$

Here the unbinding rate $k_u(\epsilon)$ is taken to be strain dependent and we take a Hill-equation like form given by $k_u(\epsilon) = k_{u0}e^{\alpha\boldsymbol{\nabla}\cdot\boldsymbol{u}}$ [56, 55] where k_{u0} is the strain independent unbinding rate and α is a dimensionless quantity. The nature of strain dependence will depend on sign of α when $\alpha > 0$ a local extension (compression) of the mesh will increase (decrease) the myosin unbinding, while with $\alpha < 0$ we get an opposite effect. We explore all these possibilities and show that the sign of α does not change the qualitative behaviour of the dynamics (see Appendix.A.1).

3.4 Linear stability analysis of active elastomer

3.4.1 Linear equations

For the linear analysis, we consider Eq. 3.13 and Eq. 3.14, with the mesh density slaved to the elastic compression as described before. To keep this analysis simple,

we take the $\boldsymbol{\sigma}^a = -\zeta_1 (1 + \zeta' \rho) \Delta\mu\rho_b$, $\boldsymbol{\sigma}^e = B\boldsymbol{\nabla} \cdot \boldsymbol{u}$ and $\boldsymbol{\sigma}^d = \eta\boldsymbol{\nabla} \cdot \dot{\boldsymbol{u}}$. Since $\boldsymbol{\sigma}^a$ is contractile, we take $\zeta_1 < 0$. In this one-constants approximation, B and η are given by $\lambda + 2\nu$ and $\eta_b + \frac{4}{3}\eta_s$, respectively. For convenience, we set $\zeta' = 1$. These equations can be rewritten in dimensionless form with time (t) and space ($\boldsymbol{x}$) in units of k_b^{-1} and $l = \sqrt{\frac{\eta}{\Gamma}}$, respectively, leading to the following redefinitions described in Table. 3.1.

Table 3.1. Dimensionless redefinitions

$\frac{u}{l} \to u$	$\rho_b/\rho_{b0} \to \rho_b$	$\frac{B}{\Gamma k_b l^2} \to B$
$\frac{\zeta_1 \Delta\mu\rho_{b0}}{\Gamma k_b l^2} \to \zeta_1\Delta\mu$	$\frac{k_{u0}}{k_b} \to k$	$\frac{D}{k_b l^2} \to D$

The rescaled parameter k is referred as inverse lifetime. Using the above redefinitions we rewrite Eq. 3.13 and Eq. 3.14 in dimensionless form

$$\begin{aligned} (1 - \nabla^2)\dot{\boldsymbol{u}} &= (B + \zeta_1\Delta\mu)\nabla^2\boldsymbol{u} - \zeta_1\Delta\mu\boldsymbol{\nabla}\rho_b \\ \dot{\rho}_b + \boldsymbol{\nabla} \cdot (\rho_b\dot{\boldsymbol{u}}) &= D\boldsymbol{\nabla}^2\rho_b - ke^{\alpha\boldsymbol{\nabla}\cdot\boldsymbol{u}}\rho_b + \rho \end{aligned} \tag{3.15}$$

Upon linearizing about the unstrained, homogeneous fixed point (u_0, ρ_{b0}, ρ_0) , we obtain the following equations,

$$\begin{aligned} (1 - \nabla^2)\delta\dot{\boldsymbol{u}} &= (B + \zeta_1\Delta\mu)\nabla^2\delta\boldsymbol{u} - \zeta_1\Delta\mu\nabla\delta\rho_b \\ \delta\dot{\rho}_b + \nabla \cdot \delta\dot{\boldsymbol{u}} &= D\nabla^2\delta\rho_b - k(\alpha + c)\boldsymbol{\nabla} \cdot \delta\boldsymbol{u} - k\delta\rho_b \end{aligned} \tag{3.16}$$

where we have used the fact that the fluctuation in ρ is slaved to the compression, $\delta\rho = -c\epsilon_{ii}$ ($c > 0$). Now by taking Fourier transform of the above equations (Eq. 3.16) in space, $\tilde{f}(\boldsymbol{q}, t) = \int_{-\infty}^{\infty} f(\boldsymbol{x}, t)e^{-i\boldsymbol{q}\cdot\boldsymbol{x}}d\boldsymbol{x}$, we obtain the eigenvalue equation,

$$\begin{bmatrix} \delta\dot{\tilde{u}} \\ \delta\dot{\tilde{\rho}}_b \end{bmatrix} = \begin{bmatrix} -\left(\frac{q^2}{1+q^2}\right)(B + \zeta_1\Delta\mu) & -\left(\frac{iq}{1+q^2}\right)\zeta_1\Delta\mu \\ iq\left(\frac{q^2}{1+q^2}(B + \zeta_1\Delta\mu) - (\alpha + c)k\right) & -\left(k + \frac{q^2}{1+q^2}\zeta_1\Delta\mu + q^2D\right) \end{bmatrix} \times \begin{bmatrix} \delta\tilde{u} \\ \delta\tilde{\rho}_b \end{bmatrix} . \tag{3.17}$$

Solving (3.17) for the two eigenvalues, λ_+ and λ_-, we obain the general solution,

$$\begin{aligned}\delta\tilde{u}(\boldsymbol{q},t) &= u_1(\boldsymbol{q})e^{\lambda_+ t} + u_2(\boldsymbol{q})e^{\lambda_- t}\\ \delta\tilde{\rho_b}(\boldsymbol{q},t) &= \rho_{b1}(\boldsymbol{q})e^{\lambda_+ t} + \rho_{b2}(\boldsymbol{q})e^{\lambda_- t}\end{aligned} \tag{3.18}$$

where, $\lambda_\pm = \lambda_1 \pm \sqrt{\lambda_2}$, with

$$\begin{aligned}\lambda_1 &= \frac{-\left(k(1+q^2) + Dq^2(1+q^2) + q^2(B+2\zeta_1\Delta\mu)\right)}{2(1+q^2)}\\ \lambda_2 &= \frac{\left(k\left(1+q^2\right) + q^2\left(\left(B+D+Dq^2\right) + 2q^2\zeta_1\Delta\mu\right)^2 - 4q^2\left(1+q^2\right)\left(B\left(k+Dq^2\right) + \left(Dq^2 + k(1+c+\alpha)\right)\zeta_1\Delta\mu\right)\right.}{4(1+q^2)^2}\end{aligned} \tag{3.19}$$

Next we investigate the stability of the homogeneous, unstrained state with changing parameters.

3.4.2 Fastest growing mode : Instabilities of the homogeneous state

With the eigenvalues given by Eq. 3.19 now we can explore the stability of the unstrained, homogeneous fixed point (u_0, ρ_{b0}, ρ_0) and the nature of temporal evolution of the perturbations about this fixed point. We charaterize the dynamics of the solutions $\delta\tilde{\rho_b}(\boldsymbol{q},t)$ and $\delta\tilde{u}(\boldsymbol{q},t)$ using the eigenvalues as described below -

Table 3.2. Phases from linear stability analysis

$max\{\mathcal{R}e(\lambda_\pm)\} < 0$	$\mathcal{I}m(\lambda_\pm) = 0$	Stable (monotonic decay)
$max\{\mathcal{R}e(\lambda_\pm)\} < 0$	$\mathcal{I}m(\lambda_\pm) \neq 0$	Stable (damped travelling wave)
$max\{\mathcal{R}e(\lambda_\pm)\} > 0$	$\mathcal{I}m(\lambda_\pm) \neq 0$	Oscillatory
$max\{\mathcal{R}e(\lambda_\pm)\} > 0$	$\mathcal{I}m(\lambda_\pm) = 0$	Contractile instability

Here contractile instability refers to a state where the elastomer behaves like a material with a negative bulk modulus.

When $\lambda_2 < 0$ i.e., $\mathcal{I}m(\lambda_\pm) \neq 0$, then the real part of $\lambda_\pm = \lambda_1$. Now this real part reaches a maximum for the mode $q = q^*$ obtained by solving $\partial_q\lambda_1 = 0$ for q. This q^* is regarded as the *fastest growing mode* (the mode with the largest rate of amplitude

increase) in this problem and given by,

$$q^* = \sqrt{\frac{-D + \sqrt{-(B + 2\zeta_1 \Delta\mu)D}}{D}} \tag{3.20}$$

The homogeneous, unstrained state becomes unstable (solutions diverge in time) for $\mathcal{R}e(\lambda_\pm) > 0$. At the threshold solving $\mathcal{R}e(\lambda_\pm) = 0$ for q gives us the critical wave vector q_c and at the wake of the instability the fastest growing mode should be equal to q_c (see Fig. 3.3). Then this condition $q^* = q_c$ let us rewrite the fastest growing mode at the threshold when the instability first appears as

$$q_c = (\frac{k}{D})^{\frac{1}{4}} \tag{3.21}$$

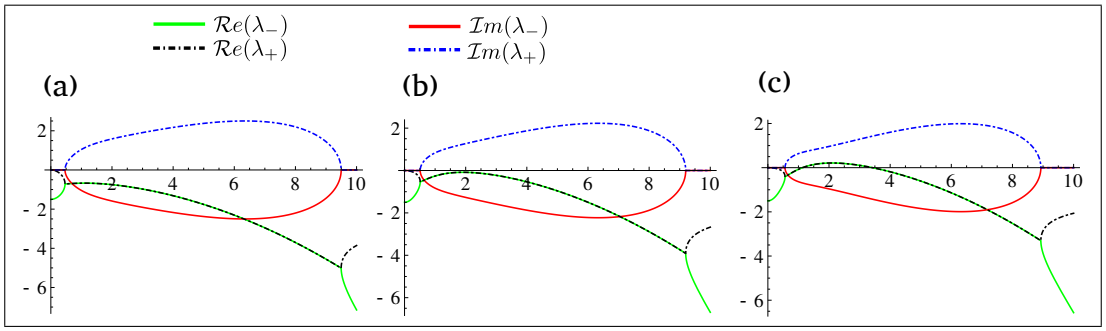

Figure 3.3. Fastest growing mode in linear stability : $\mathcal{I}m(\lambda_\pm)$ and $\mathcal{R}e(\lambda_\pm)$ values as function as wave number q shows the wake of the instability. The parameter values are (a) $-\zeta_1\Delta\mu = 3$, (b) $-\zeta_1\Delta\mu = 3.83$, (c) $-\zeta_1\Delta\mu = 4.2$, and other parameters are $B = 5.5$, $c = 0.1$, $D = 0.1$, $k = 1.5$, $\alpha = 0.1$. Using the relation $q_c = (\frac{k}{D})^{\frac{1}{4}}$ in this case, we get the rough value $q_c = 1.96$.

Using the value for q_c enables us to write the condition for emergence of the unstable behaviour in a mode independent way :

$$B + D + k\left(1 + \sqrt{\frac{4D}{k}}\right) < -2\zeta_1\Delta\mu\,. \tag{3.22}$$

We characterize the phases and present the phase diagrams in terms of the relevant parameters in the next section.

3.4.3 Phase diagram

Here we discuss the phase diagrams using conditions for four different states (Table. 3.2). The phase diagrams (Fig. 3.4) presented in terms of the rescaled parameters (Table.3.1) such as the bulk modulus B, contractile stress $-\zeta_1\Delta\mu$ and binding unbinding rate ratio or inverse lifetime k provide preliminary yet useful physical understanding of the active elastomer dynamics. In case of large rigidity of the mesh ($B \to$ large) or small lifetime ($k \to$ large) of bound myosin, the homogeneous, unstrained state is stable under perturbations (Fig. 3.4 a,b). In this scenario we see two different kinds of relaxation dynamics : either the disturbances decay exponentially in time regarded here as *monotonic decay* (S_d) or they decay through *damped travelling waves* (S_t). The homogeneous, unstrained state becomes unstable in the regime where the active contractile stress ($-\zeta_1\Delta\mu$) becomes large (Fig. 3.4 a,b). The unstable behaviour can be characterized in two states : the unstable oscillations where the travelling wave amplitude diverges in time regarded here as *oscillatory* (O) and another is regarded as *contractile instability* (CI) where the perturbations diverge exponentially in time. The typical behaviour of eigenvalues ($\lambda_\pm$) with the wave vector q is presented in Fig. 3.4 (c-f) to illustrate monotonic decay, damped travelling wave, oscillatory, contractile instability phases respectively.

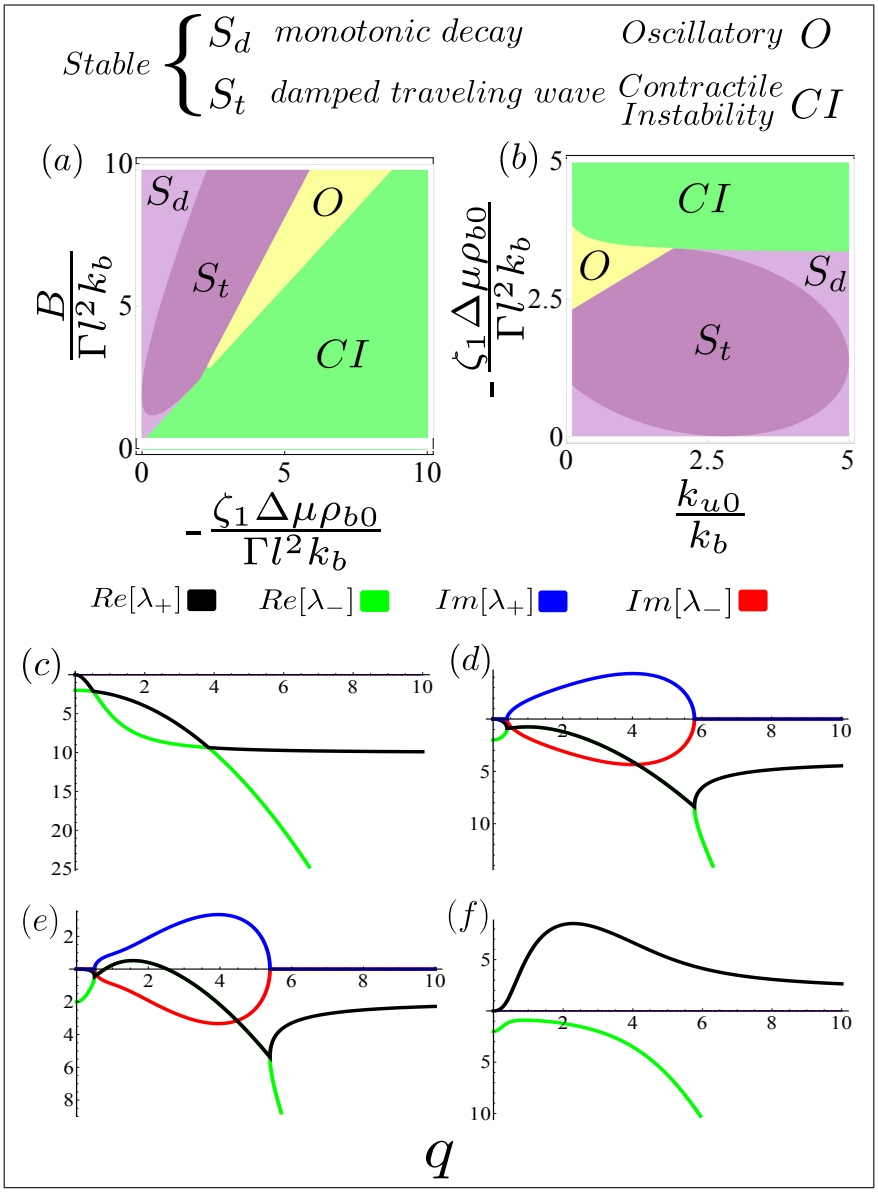

Figure 3.4. Phase diagram and dispersion relations from linear stability : (a-b) Linear stability phase diagrams in (a) effective elastic stress density vs. contractile stress density at $k = 1$ and (b) Effective contractile stress density vs. inverse lifetime of bound myosin at $B = 4$. The stresses are normalized by the frictional stress density, $\Gamma k_b l^2$. The phases are described in the legend. Rest of the dimensionless parameters are $\alpha = 0.1, c = 0.1, D = 0.1$. (c-f) Typical dispersion curves obtained from linear stability analysis, showing the complex roots $\lambda_\pm$ as a function of wave-vector q. Colour code displayed above. Panels shows typical behaviour in the (c) stable, (d) damped travelling wave, (e) unstable oscillations, and (f) contractile instability phases.

Now we again consider the case when the homogeneous, unstrained state first becomes unstable, i.e., $Re(\lambda_{\pm}) = 0$ is true only for the fastest growing mode, $q = q_c$. This condition corresponds to a point in the parameter space on the phase boundary between stable and unstable phases. On this phase boundary we can simplify the general solutions (Eq. 3.18) to show that we get stable travelling wave solutions with frequency $\omega_c = \sqrt{\frac{kB}{2}}$ and veloity $v_c = \frac{\omega_c}{q_c} = \left(\frac{kDB^2}{4}\right)^{\frac{1}{4}}$.

The onset of the oscillatory behaviour is dictated by $\mathcal{I}m(\lambda_{\pm}) > 0$ or simply $\lambda_2 < 0$. The threshold condition $\mathcal{I}m(\lambda_{\pm}) = 0$ define the phase boundary of the oscillatory behaviour and given by

$$\left(Bq^2 + (1+q^2)(k+qD)\right)^2 + 4q^2\zeta_1\Delta\mu(Bq^2 - k(\alpha+c)(1+q^2) + q^2\zeta_1\Delta\mu) = 0 \quad (3.23)$$

The frequency of oscillation in the oscillatory phase is given by $\omega = \sqrt{\lambda_2}$. Linear analysis predicts a non-monotonic dependence of frequency on bulk modulus of the mesh and contractile stress as presented in Fig. 3.5.

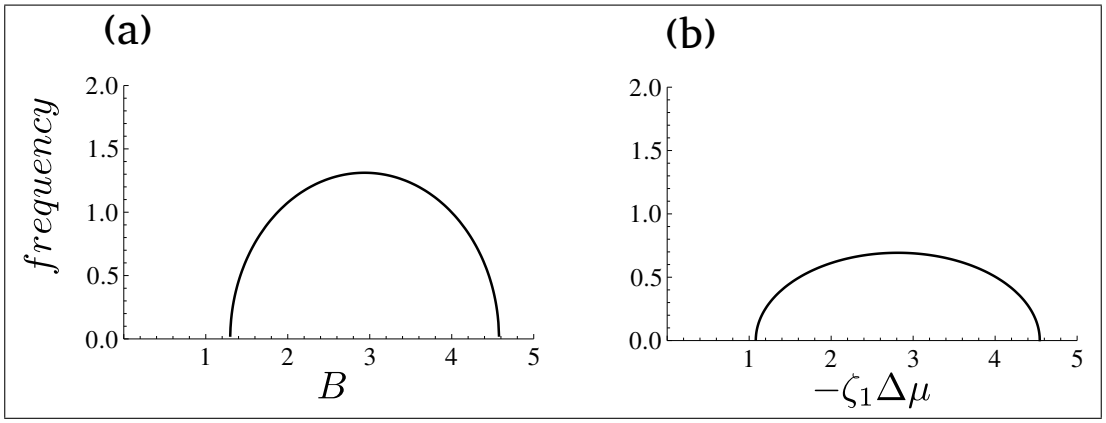

Figure 3.5. Frequency of oscillation from linear analysis shows non-monotonic behaviour with (a) changing bulk modulus B and (b) contractile stress $-\zeta_1\Delta\mu$. The parameter values are (a) $-\zeta_1\Delta\mu = 1$, $k = 0.25$ (b) $B = 6$, $k = 0.5$ and other parameters are $c = 0.1$, $D = 0.1$, $\alpha = 0.1$, $q = 2$ (same for both plots).

The contractile instability is a runaway instability and the behaviour is similar to a material with negative bulk modulus where the homogeneous, unstrained state becomes a unstable fixed point of the system. One would expect that including higher order elastic free energy terms will subdue this instability and give rise to stable contracted state. This is true in our case as we shall see later in this chapter.

While the insight gained from linear stability analysis is limited, the analysis indicates the possible existence of sustained oscillations when one includes the nonlinear terms which might stabilize the oscillatory phase and we investigate the effects of various nonlinear terms in the next few sections in this chapter as we deal the problem with mode truncated studies.

3.5 Active elastomer in one dimension

As already discussed, with the linear stability indicating unstable oscillations and contractile instability, we shall probe nonlinearities of the system and learn the essential feature they can bring to the dynamics. We perform the mode truncated analysis in one dimension so we shall briefly present the one dimensional description of the active elastomer for completeness.

Derived from Eq.3.13 and Eq.3.14, the one dimensional equations are given by

$$\Gamma \dot{u} = \partial_x \left(\sigma^e + \sigma^d + \sigma^a \right) \tag{3.24}$$

and

$$\dot{\rho}_b + \partial_x (\dot{u} \rho_b) = D \partial_x^2 \rho_b - k_{u0} e^{\alpha \partial_x u} \rho_b + k_b \rho \,. \tag{3.25}$$

Here the linearized strain is simply $\partial_x u$. With this we shall proceed to perform the mode truncated analysis for the active elastomer.

3.6 Mode truncated analysis

With the linear analysis results we can see the existence of unstable oscillations and it is possible that these unstable oscillatory behaviour might get stabilized when nonlinearities are introduced. To investigate this we perform mode truncated analysis (also known as *Galarkin truncation method* [59]) including nonlinearities arising from strain dependent unbinding of myosin, advective current of bound myosin, active stress and elastic stress. In this section we introduce the basic setup for the analysis and in the next few sections we discuss the effects of introducing various nonlinearities.

Now rewriting the equations (Eq. 3.24 and Eq. 3.25) in terms of the variation in

displacement field ($\delta u = u - u_0$) and bound myosin density ($\delta\rho_b = \rho_b - \rho_{b0}$) about the homogeneous, unstrained state (ρ_{b0}, u_0) and using the dimensionless parameters (Table.3.1) we get

$$\begin{aligned} (1+\partial_x^2)\delta\dot{u} &= \partial_x\sigma^e + \partial_x\sigma^a \\ \dot{\delta\rho_b} + \partial_x(\delta\dot{u}(1+\delta\rho_b)) &= D\partial_x^2\delta\rho_b - k\left(\alpha\partial_x\delta u + \frac{\alpha^2}{2}(\partial_x\delta u)^2\right)(1+\partial_x\delta\rho_b) - c\partial_x\delta u\,. \end{aligned} \tag{3.26}$$

Here for the strain dependent myosin unbinding we take an approximate form with leading order nonlinearity $k_{u0}e^{\alpha\partial_x u}\rho_b = k_{u0}(1+\alpha\partial_x u + \frac{1}{2}(\alpha\partial_x u)^2)\rho_b$ throughout all mode truncated analysis done in this section.

Now we assume an solution for $\delta u(x,t)$ and $\delta\rho_b(x,t)$ in terms of Fourier series in a region $x \in [-L, L]$ with periodic boundary conditions.

$$\begin{aligned} \delta u(x,t) &= \sum_{n=0}^{\infty} u_n(t)cos(\frac{n\pi x}{L}) + u_n'(t)sin(\frac{n\pi x}{L}) \\ \delta\rho_b(x,t) &= \sum_{n=0}^{\infty} \rho_{bn}(t)sin(\frac{n\pi x}{L}) + \rho_{bn}'(t)cos(\frac{n\pi x}{L}) \end{aligned} \tag{3.27}$$

With this general solution in terms of all individual modes we only consider a finite number of modes in mode truncated studies and plug these approximate solutions in the Eq. 3.26. Then considering the balance of each mode separately we find the resulting system of ordinary differential equations in terms of the amplitudes of the individual modes (i.e., $u_n(t)$, $u_n'(t)$, $\rho_{bn}(t)$, $\rho_{bn}'(t)$). This system of ODE's dictate the temporal dynamics of the appropriate system constituted of the selected modes. In the next sections we perform mode truncated analysis in terms of the largest length-scale and second largest length-scale modes to explore the features of active elastomer. This kind of analysis has been done previously to study active solids descriptions relevant to muscle cells [46] and active solid description used to understand area oscillation in dorsal closure [49].

3.7 One mode analysis

Now taking account of only the first nontrivial mode ($n = 1$) in the system we describe the single mode approximate solution of δu and $\delta\rho_b$ as

$$\begin{aligned}\delta u(x,t) &= u_1(t)cos(ax)\\ \delta\rho_b(x,t) &= \rho_{b1}(t)sin(ax)\end{aligned} \tag{3.28}$$

Here $a = \frac{\pi}{L}$ and we have taken $u_1' = 0$ and $\rho_{b1}' = 0$ for simplicity. Now we use the above stated single mode approximate solution to rewrite the active elastomer equation (Eq. 3.26). The elastic and dissipative stresses are given by $\sigma^e = B\partial_x u + B'(\partial_x u)^3$ and $\sigma^d = \eta\partial_x\dot{u}$ respectively. The active stress is given by $\sigma^a = -\zeta_1\Delta\mu\,(\rho_b - \zeta'\partial_x u)$. The nonlinearity in the elastic stress is coming from a quartic term in elastic free energy. We shall present a more formal discussion about the possible origin of these higher order terms in the elastic free energy in the next chapter. Here we mainly explore the effects of incorporating such nonlinearities. The resulting dynamical system in terms of the time dependent mode amplitudes $u_1(t)$ and $\rho_{b1}(t)$ is given below.

$$\begin{aligned}\dot{u_1} &= -\left(\frac{a^2}{1+a^2}\right)(B+\zeta_1\Delta\mu)u_1 - \left(\frac{a^4}{4(1+a^2)}\right)B'u_1^3 - \zeta_1\Delta\mu\left(\frac{a}{1+a^2}\right)\rho_{b1}\\ \dot{\rho_{b1}} &= a\dot{u_1} - k\rho_{b1} - \frac{3}{8}a^2\alpha^2 k u_1^2\rho_{b1} + a(c+\alpha k)u_1\end{aligned} \tag{3.29}$$

Here we have assumed $\zeta' = 1$ for simplicity. Next we show that this resulting dynamical system is similar to Van der Pol oscillator and stable limit cycle solutions appear at certain parameter range.

3.7.1 Mapping to Van der Pol oscillator

The resulting dynamical system can be mapped to a generalized Van der Pol oscillator of the form

$$\ddot{u}_1 = -A_1(u_1^2 + \frac{A_2}{A_1})\dot{u}_1 - P(u_1)u_1 \tag{3.30}$$

Here A_1, A_2 and $P(u_1)$ are given as following

$$\begin{aligned} A_1 &= \frac{3}{8}\left(\frac{a^2}{1+a^2}\right)\left(2a^2B' + (1+a^2)k\alpha^2\right) \\ A_2 &= \left(\frac{a^2}{1+a^2}\right)(B + 2\zeta_1\Delta\mu) + k \end{aligned}$$

$$\begin{aligned} P(u_1) = &\left(\frac{a^2}{1+a^2}\right)(Bk + \zeta_1\Delta\mu(c+k+\alpha k)) \\ &+ \left(\frac{a^4k}{8(1+a^2)}\right)\left(2B' + 3(B+\zeta_1\Delta\mu)\alpha^2\right)u_1^2 \\ &+ \left(\frac{3a^6}{32(1+a^2)}\right)(\alpha^2kB')u_1^4 \end{aligned} \tag{3.31}$$

From the resulting generalized Van der Pol equation (Eq. 3.30) solution we see the emergence of limit cycle when A_2 crosses zero. This provide us with the condition for sustained oscillations when $B + 2\zeta_1\Delta\mu + \left(1 + \frac{1}{a^2}\right)k < 0$ and $P(u_1) > 0$. The oscillatory behaviour emerges because of the nature of the dissipative term in Eq. 3.30 which provides negative dissipation (energy infusion into system) when $u_1^2 + \frac{A_2}{A_1} < 0$ and positive dissipation otherwise. This is only possible if $A_2 < 0$ as u_1 is real and A_1 is always positive.

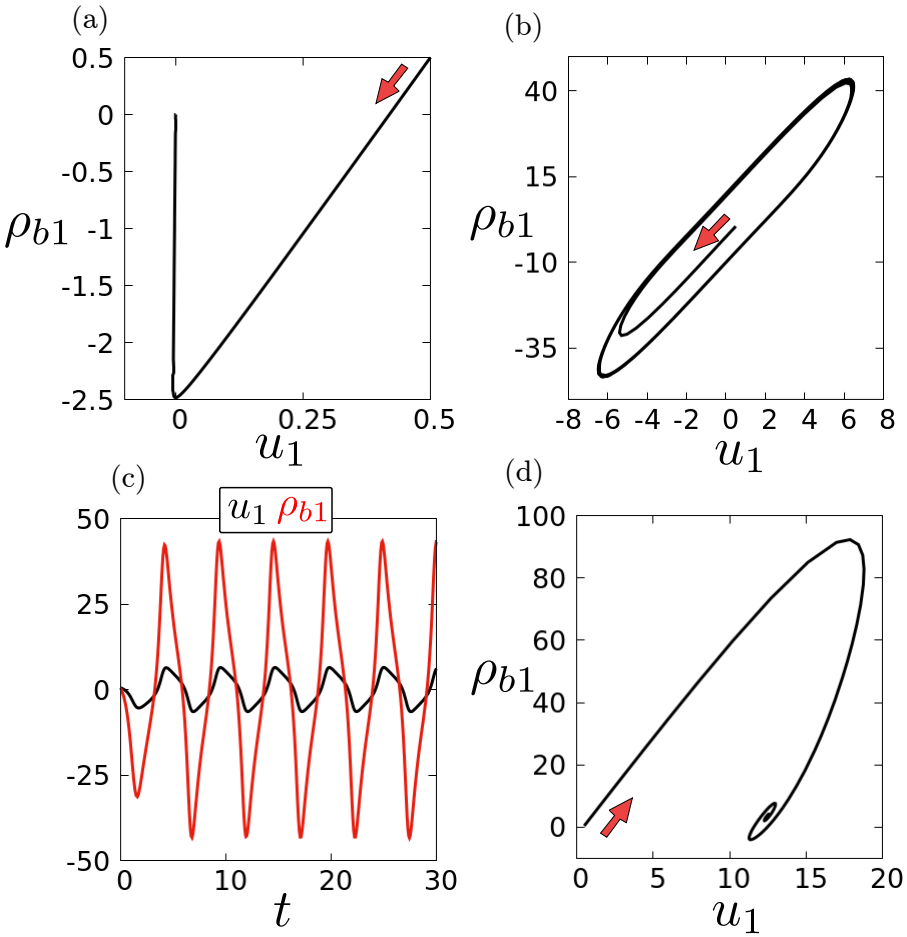

Figure 3.6. Temporal dynamics of u_1 and ρ_{b1} shows (a) stable, (b) oscillatory and (d) contracted steady state from one mode analysis. The u_1 and ρ_{b1} solution shows emergence of limit cycle (b) where these variables show spontaneous oscillation (c) resulting from the contractility of myosin motors. The red arrow marks the initial position and the direction of change of u_1 and ρ_{b1} with time. Parameter values : (a) $-\zeta_1\Delta\mu = 0.1$, (b) $-\zeta_1\Delta\mu = 5$, (d) $-\zeta_1\Delta\mu = 15$ and all other parameter values are $B = 8$, $B' = 0.005$, $\alpha = 0.1$, $c = 0.1$ and $k = 0.1$.

3.7.2 Limit cycle and Hopf-bifurcation

At low values of active contractile stress the homogeneous, unstrained state ($\delta u = 0,\ \delta\rho_b = 0$) is stable fixed point of the system (see Fig. 3.6 a). Oscillatory solutions appears with increasing contractile stress as the homogeneous, unstrained state becomes unstable and a stable limit cycle solution emerges, this marks a super-critical Hopf-bifurcation in the system at $-\zeta_1\Delta\mu = \frac{B}{2} + \left(1 + \frac{1}{a^2}\right)\frac{k}{2}$ (see Fig. 3.7 and Fig.3.6 b,c). At even higher values of contractile stress a stable fixed point with non-zero u_1

value emerges (see Fig.3.7 and Fig.3.6 d). This fixed point refers to the *contracted* state of the active elastomer. This deformed stable state is a result of including a higher order term (nonlinearity in elastic stress) in elastic free energy without this nonlinearity we would encounter contractile instability (see Fig.3.8 c).

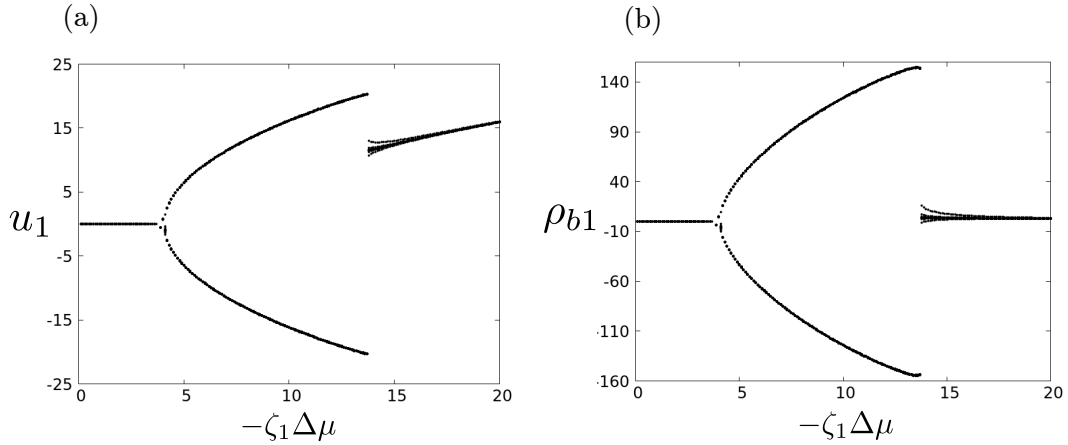

Figure 3.7. A supercritical Hopf-bifurcation shows emergence of limit cycles in (a) u_1 vs $-\zeta_1\Delta\mu$ and (b) ρ_{b1} vs $-\zeta_1\Delta\mu$. At higher values of $-\zeta_1\Delta\mu$ we see the system to settle in a fixed point with nonzero u_1 value. This fixed point correspond to the contracted state of the active elastomer. Parameter values used for this plot are $B = 8$, $B' = 0.005$, $\alpha = 0.1$, $c = 0.1$ and $k = 0.1$.

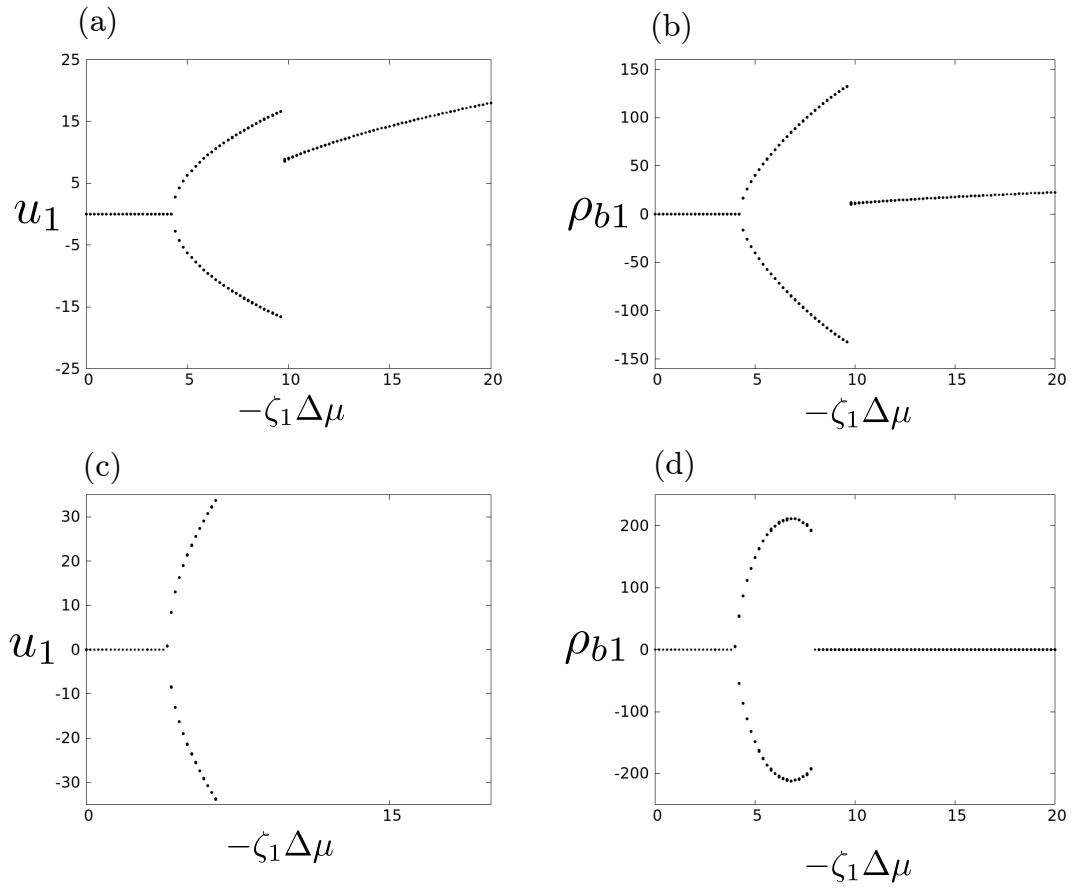

Figure 3.8. Emergence of limit cycle in bifurcation diagrams for (a) u_1 vs $-\zeta_1\Delta\mu$ and (b) ρ_{b1} vs $-\zeta_1\Delta\mu$ with $\alpha = 0$ shows that nonlinearity in elastic stress (from higher order terms in elastic free energy) is sufficient for sustained spontaneous oscillatory behaviour. Bifurcation diagrams in (c) u_1 vs $-\zeta_1\Delta\mu$ and (d) ρ_{b1} vs $-\zeta_1\Delta\mu$ with $B' = 0$ shows sustained spontaneous oscillations, proving that nonlinearity in strain dependent unbinding term can also give rise to oscillatory behaviour but it fails to stabilize the contractile instability. Parameter values used for this plot are $B = 8$, $B' = 0.005$ (a-b), $\alpha = 0.1$ (c-d), $c = 0.1$ and $k = 0.1$.

Probing the effects of the nonlinearities in elastic stress and unbinding rate (see Table.3.3) we conclude that both the nonlinear effects can support a sustained spontaneous oscillatory state but without the nonlinearity in elastic stress the contractile instability at high values of contractile stress can not be stabilized.

Table 3.3. One mode analysis

$\alpha = 0$	$B' = 0$	No spontaneous oscillation	Contractile instability
$\alpha \neq 0$	$B' = 0$	Spontaneous oscillation	Contractile instability
$\alpha = 0$	$B' \neq 0$	Spontaneous oscillation	Contracted state
$\alpha \neq 0$	$B' \neq 0$	Spontaneous oscillation	Contracted state

With the one mode approximation we could probe the above discussed nonlinear effects but some nonlinearities (e.g., advective nonlinearity) cannot be probed with this approximation and we need to include higher modes (smaller wavelength) in the approximate solution to capture the effects of such nonlinearities. So we proceed to perform a *two mode* analysis in the next section.

3.8 Two modes analysis

In this section we probe the advective nonlinearity and the nonlinearities in active stress along with the nonlinearities already probed in one mode analysis. The advective and active stress related nonlinearities cannot be captured with a single mode approximation as used in one mode analysis. To probe the these nonlinearities we take the simplest approximate solutions just adding a contribution from the second mode ($n = 2$) in myosin density variation $\delta\rho_b$ as stated here.

$$\begin{aligned} \delta u(x,t) &= u_1(t)cos(ax) \\ \delta\rho_b(x,t) &= \rho_{b1}(t)sin(ax) + \rho_{b2}(t)cos(2ax) \end{aligned} \tag{3.32}$$

This two mode analysis allows us to construct a 3-dimensional dynamical system description (u_1, ρ_{b1}, ρ_{b2}) of active elastomer to investigate existence of chaotic solutions which are not possible to probe in lower dimensional systems. The active stress in this case is defined as $\sigma^a = -\zeta_1\Delta\mu\,(\rho_b - \zeta'\partial_x u + \zeta''\rho_b\partial_x u + \zeta'''\rho_b^2)$. All other terms are same as defined in case of one mode analysis.

3.8.1 Resulting equations

Now using the above stated two mode approximation for the active elastomer dynamics (Eq. 3.26) and separating the resulting equations mode-wise we get the following dynamical systems description

$$\dot{u_1} = -\left(\frac{a^2}{1+a^2}\right)(B+\zeta_1\Delta\mu)u_1 - \left(\frac{a^4}{4(1+a^2)}\right)B'u_1^3 - \zeta_1\Delta\mu\left(\frac{a}{1+a^2}\right)\rho_{b2} + \left(\frac{a}{1+a^2}\right)\zeta_3\Delta\mu\rho_{b1}\rho_{b2} - \left(\frac{a^2}{1+a^2}\right)\zeta_2\Delta\mu u_1\rho_{b2}$$

$$\dot{\rho_{b1}} = a(1+\frac{\rho_{b2}}{2})\dot{u_1} - a^2D\rho_{b1} + acu_1 - \left(\frac{ak\alpha}{2}\right)u_1\rho_{b2} - \frac{3}{8}a^2\alpha^2ku_1^2\rho_{b1} \tag{3.33}$$

$$\dot{\rho_{b2}} = a\rho_{b1}\dot{u_1} - 4a^2D\rho_{b2} - \left(\frac{ak\alpha}{2}\right)u_1\rho_{b1} - \frac{1}{4}a^2\alpha^2ku_1^2\rho_{b2}$$

Here we have taken $\zeta' = 1$, $\zeta_1\zeta'' = \zeta_2$ and $\zeta_1\zeta''' = \zeta_3$. We solve the above dynamical system and probe the effects of various nonlinearities and show that the system, in addition to the spontaneous oscillations already seen, takes a period doubling route to chaos. In the next section we present these results and determine the essential nonlinearities that drive the system to chaotic solutions.

3.8.2 Bifurcation and limit cycle

We probe the time evolution of the system with increasing contractile stress and for low values of contractile stress the behaviour of the system is similar as found in the one mode analysis earlier, i.e. the homogeneous unstrained state is a stable fixed point of the system. With increasing contractile stress we encounter emergence of limit cycles (see Fig. 3.9 a) as the system exhibit spontaneous oscillations. With further increase in contractile stress we encounter period doubling (see Fig. 3.9 b,c) and eventually the system run into chaos (see Fig. 3.9 d) and with very high values of contractile stress we find the system to reach a stable contracted state (see Fig. 3.9 f). The bifurcation diagrams (see Fig. 3.10) for u_1, ρ_{b1} and ρ_{b2} in $-\zeta_1\Delta\mu$ shows the emergence of the limit cycle and chaos. The limit cycle orbits can take complecated shapes in the three dimensional phase space as shown in Fig. 3.11.

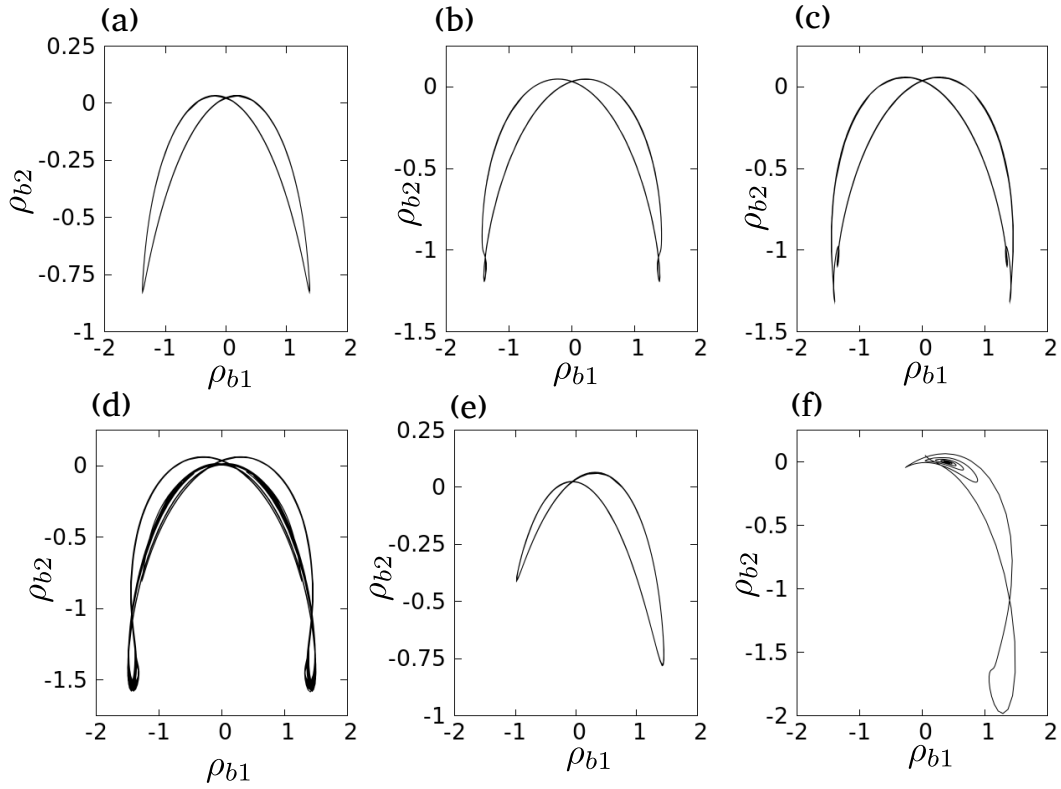

Figure 3.9. Spontaneous oscillations and chaos in two mode analysis : The ρ_{b1}-ρ_{b2} projection of the three dimensional trajectory shows (a) oscillatory solutions ($-\zeta_1\Delta\mu = 7.0$), (b-c) period doubling ($-\zeta_1\Delta\mu = 8.0$ and 9.0), (d) chaotic solution ($-\zeta_1\Delta\mu = 9.5790$), (e) asymmetric limit cycle ($-\zeta_1\Delta\mu = 10.0$) and (f) contracted stable state ($-\zeta_1\Delta\mu = 11.0$). The other parameters are $B = 8$, $B' = 0.05$, $\zeta_1 = -1$, $\zeta_2 = 0.1$, $\zeta_3 = 0.1$, $\alpha = 0.1$, $c = 0.1$, $D = 0.1$ and $k = 0.1$.

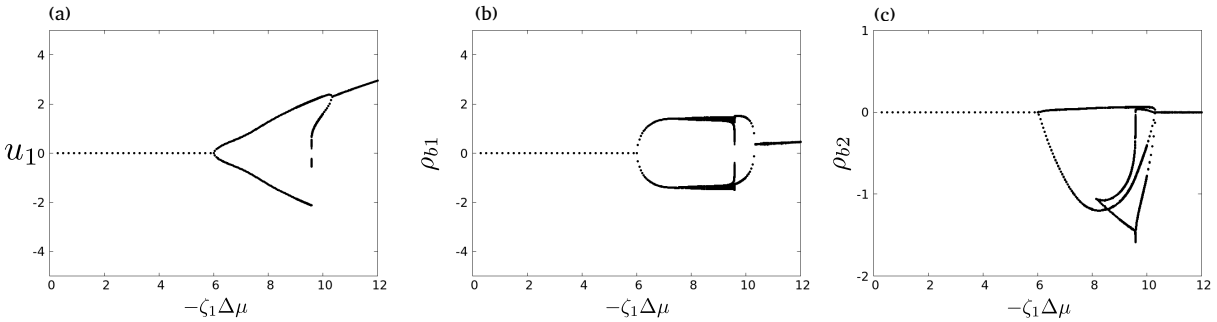

Figure 3.10. Bifurcation diagrams from two mode analysis : Bifurcation diagrams numerically constructed for (a) u_1, (b) ρ_{b1} and (c) ρ_{b2} with increasing contractile stress shows emergence of limit cycle, period doubling. Though the existence of chaotic solution is not apparent here as in this case the chaotic solutions are found in small window around $-\zeta_1\Delta\mu = 9.5$. This will be more evident in further analysis. The parameters are $B = 8$, $B' = 0.05$, $\zeta_1 = -1$, $\zeta_2 = 0.1$, $\zeta_3 = 0.1$, $\alpha = 0.1$, $c = 0.1$, $D = 0.1$ and $k = 0.1$.

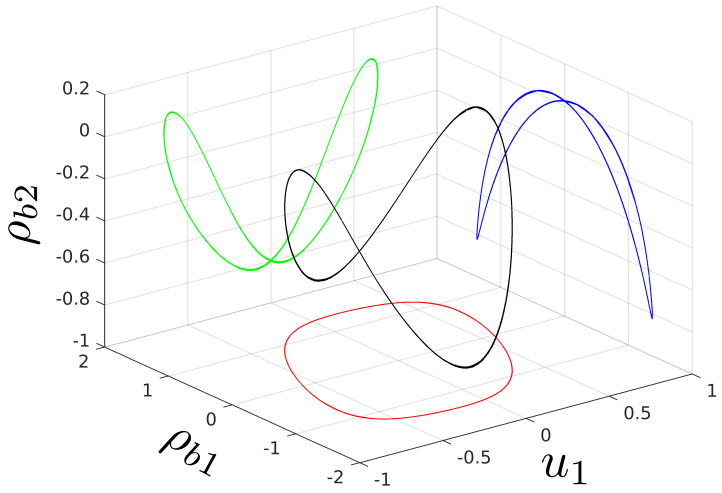

Figure 3.11. Limit cycle in phase space of u_1, ρ_{b1}, ρ_{b2} : The three dimensional orbit (black) shows a typical limit cycle solution. The projections of this limit cycle in $u_1 - \rho_{b1}$ (red), $u_1 - \rho_{b2}$ (blue) and $\rho_{b1} - \rho_{b2}$ (green) plane has also been presented. The parameters are $B = 8$, $B' = 0.05$, $-\zeta_1\Delta\mu = 7.0$, $\zeta_1 = -1$, $\zeta_2 = 0.1$, $\zeta_3 = 0.1$, $\alpha = 0.1$, $c = 0.1$, $D = 0.1$ and $k = 0.1$.

3.8.3 Chaos

Apart from the spontaneous oscillations the system shows chaotic solution (see Fig. 3.9 d). Further investigation reveals that the chaotic behaviour in the system appears within one (or more) thin window (short ranges of $-\zeta_1\Delta\mu$) and this becomes more apparent as we zoom into the bifurcation diagram. We take the bifurcation diagram in ρ_{b1} (Fig. 3.10 b) and we look more closely into the region $-\zeta\Delta\mu = [7,\ 10]$ (see Fig. 3.12). We find many chaotic windows in the range $-\zeta\Delta\mu = [9.575,\ 9.58]$ (see Fig. 3.12 c). Within the chaotic window the bifurcation diagram becomes space filling which indicates chaotic time evolution of the quantities. A look into the time evolution of phase space trajectories (see Fig. 3.13) and the variables (see Fig. 3.14) also points towards aperiodic, chaotic solutions and exhibit space filling trend in phase space with the possibility of existence of strange attractor.

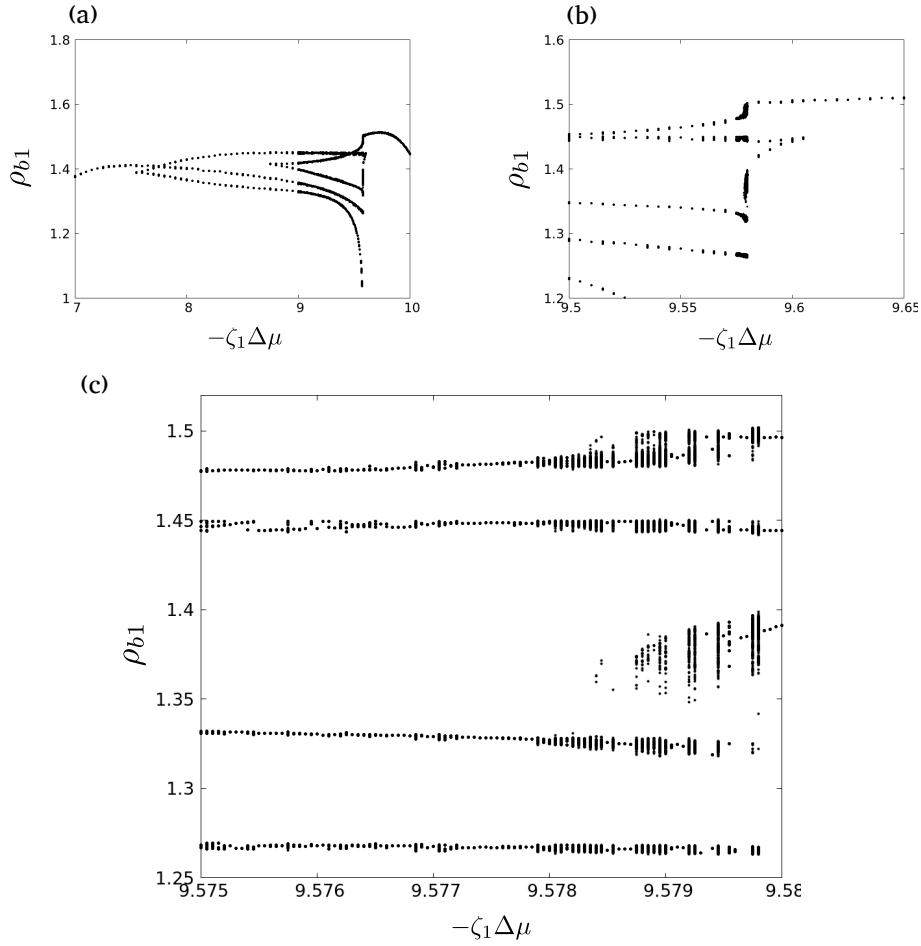

Figure 3.12. A closer look into bifurcation diagram for ρ_{b1} in the range (a) $-\zeta_1\Delta\mu = [7, 10]$, (b) $-\zeta_1\Delta\mu = [9.5, 9.65]$ and (c) $-\zeta_1\Delta\mu = [9.575, 9.58]$ reveals many windows of apparently chaotic solutions with space filling nature. The parameters are $B = 8$, $B' = 0.05$, $\zeta_1 = -1$, $\zeta_2 = 0.1$, $\zeta_3 = 0.1$, $\alpha = 0.1$, $c = 0.1$, $D = 0.1$ and $k = 0.1$.

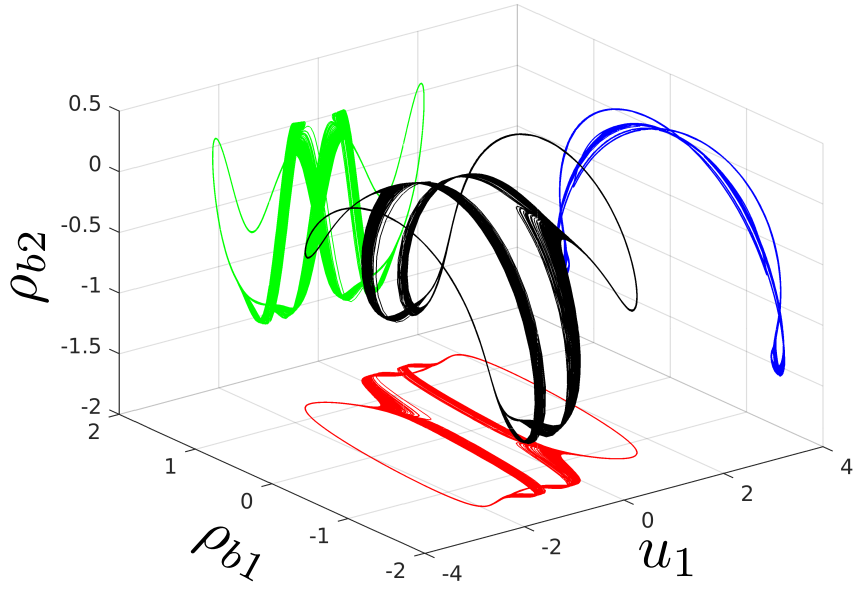

Figure 3.13. The phase portrait (black) in u_1, ρ_{b1}, ρ_{b2} shows space filling structures those indicate chaotic solutions and possible existence of strange attractor. The projections of the three dimensional trajectories are shown in $u_1 - \rho_{b1}$ (red), $u_1 - \rho_{b2}$ (blue) and $\rho_{b1} - \rho_{b2}$ (green) planes respectively. The parameters are $B = 8$, $B' = 0.05$, $-\zeta_1 \Delta\mu = 9.579$, $\zeta_1 = -1$, $\zeta_2 = 0.1$, $\zeta_3 = 0.1$, $\alpha = 0.1$, $c = 0.1$, $D = 0.1$ and $k = 0.1$.

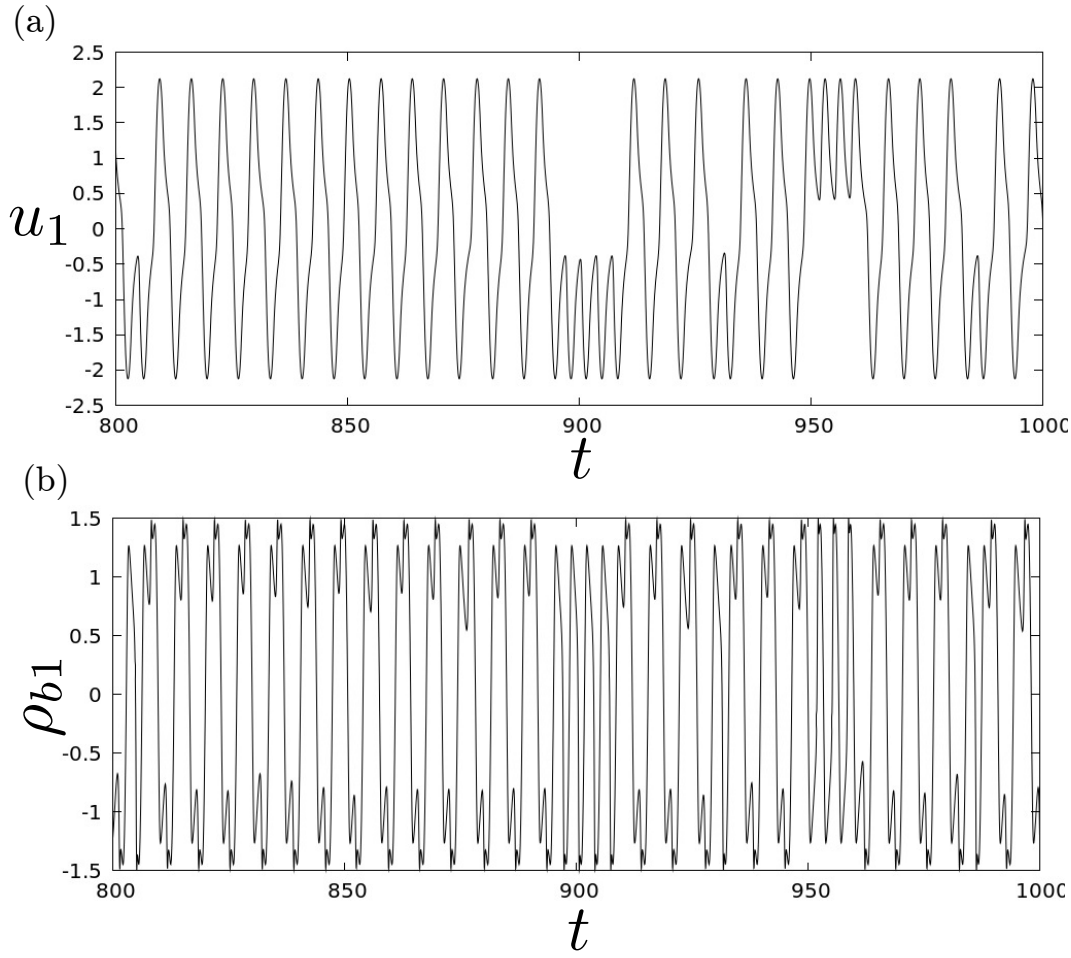

Figure 3.14. Aperiodic chaotic solutions in (a) u_1 and (b) ρ_{b1} in a time stretch (800-1000). The parameters are taken to be $B = 8$, $B' = 0.05$, $-\zeta_1\Delta\mu = 9.579$, $\zeta_1 = -1$, $\zeta_2 = 0.1$, $\zeta_3 = 0.1$, $\alpha = 0.1$, $c = 0.1$, $D = 0.1$ and $k = 0.1$.

Now we calculate the largest Lyapunov constant [60, 61] ($\mathcal{L}e$) for u_1, ρ_{b1} and ρ_{b2} time evolution to investigate the chaotic solutions in the range $-\zeta\Delta\mu = [9.575, 9.58]$ and find many windows of positive Lyapunov exponent (see Fig. 3.15) indicating existence of exponentially diverging neighbouring trajectories in phase space.

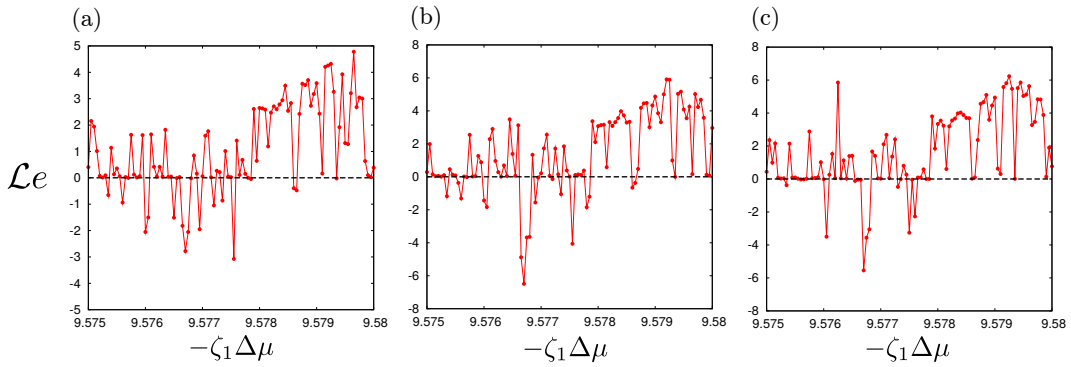

Figure 3.15. Maximal Lyapunov exponent ($\mathcal{L}e$) calculated in the window defined by $-\zeta_1\Delta\mu = [9.575, 9.58]$ for (a)u_1, (b) ρ_{b1}, (c) ρ_{b2}. Existence of many windows with positive Lyapunov exponent confirms the chaotic behaviour of the solutions in these particular range of contractile stress values. The parameter values used are $B = 8$, $B' = 0.05$, $\zeta_1 = -1$, $\zeta_2 = 0.1$, $\zeta_3 = 0.1$, $\alpha = 0.1$, $c = 0.1$, $D = 0.1$ and $k = 0.1$.

Now that we can see the existence of chaotic behaviour in the active elastomer dynamics with the inclusion of nonlinear effects. To be more specific about which nonlinearities are important for chaotic behaviour we solve the two mode system (Eq. 3.33) with one or more specific nonlinearities and present the result below (Table. 3.4) which clearly indicates the role of convective nonlinearity ($\rho_{bi}\,\dot{u}_1$ terms, $i = 1, 2$) is important for chaotic solutions.

Table 3.4. Two mode analysis

$\alpha \neq 0$	$\zeta_2,\ \zeta_3 \neq 0$	$B' \neq 0$	$\rho_{bi}\dot{u}_1 \neq 0$	Chaos
$\alpha \neq 0$	$\zeta_2,\ \zeta_3 = 0$	$B' \neq 0$	$\rho_{bi}\dot{u}_1 \neq 0$	Chaos
$\alpha \neq 0$	$\zeta_2,\ \zeta_3 \neq 0$	$B' \neq 0$	$\rho_{bi}\dot{u}_1 = 0$	No chaos

3.9 Concluding Remarks

Here we summarize the results presented in this chapter and pose the possible shortcomings and scope for future developments.

- We discussed how actomyosin network can be described as an active elastomer where each element of the active elastomer reasonably represent the constitutive elements of actomyosin network.

Hydrodynamics of apical actomyosin as an active elastomer : Affine description

- An active hydrodynamic theory was developed with minimal phenomenological inputs to understand the dynamics of active elastomer.
- Stability analysis was performed for a linear theory and existence of unstable oscillation and contractile instability was found.
- Inclusion of nonlinear effects for a theory only in terms of largest modes (resulting in a two dimensional dynamical system) showed emergence of sustained spontaneous oscillations through a supercritical Hopf-bifurcation.
- Further investigation for the mode truncated theory led us to a three dimensional dynamical systems description of active elastomer and we could study the emergence of aperiodic, chaotic behaviour in the system.

In this chapter we see emergence of sustained oscillation and chaos in active elastomer. But these approximate analysis provide information about temporal evolution only as the spatial degrees of freedom do not exist in these descriptions. Thus to explore the spatiotemporal dynamics of actomyosin pulsation and flow, we numerically solve the resulting system (Eq. 3.13 and Eq. 3.14) for active elastomer in the next chapter and present the findings.

End of Chapter

Chapter 4

Numerical solution of affine active elastomer : Spatiotemporal features

4.1 Introduction

We have proposed a hydrodynamical theory for active elastomer to understand actomyosin dynamics during morphogenesis of cell and tissue. This description was derived from symmetries of the system with phenomenologically inspired inputs as we presented in the previous chapter. We also attempted to understand the dynamical behaviour of active elastomer from linear stability analysis and mode truncated studies. These studies enabled us to understand the emergence of sustained spontaneous oscillations which can be related to the spontaneous periodic density variation (i.e., the pulsation) in apical actomyosin during germband extension [12, 11] and mesoderm invagination [8, 4]. But the analysis done in the previous chapter brings out the features of temporal dynamics only so the features of spatiotemporal dynamics of the actomyosin could not be explained from such approximate methods. In this chapter we treat the resulting equations of the active elastomer system numerically with all the nonlinearities and explore the spatiotemporal features.

Let us recapitulate the essential features of actomyosin dynamics in the context of germband extension that we are interested in. During germband extension, intercalation in germband cells drive the tissue elongation [5] and the contractile forces generated through actomyosin pulsation and flow inside the individual cells drive junction remodeling [12, 31] which results in T_1 intercalation. Now a closer look at the spatiotemporal dynamics of the actomyosin network will reveal that *pulsation* and *flow* (see Fig.4.1) emerges from dynamics of f-actin network and non-muscle

myosin at smaller length scales. As in the case of any *in vivo* process these actin and myosin dynamics are regulated locally via many chemical signalling pathways (conserved Rho1-ROCK pathway is one major example[11]). Having said this, the work by akankshi et al [11] has presented an important analysis to show that mechanics play a vital role in flawless completion of cell and tissue morphogenesis and the dynamics of actomyosin in germband cell is truly a mechano-chemical in nature.

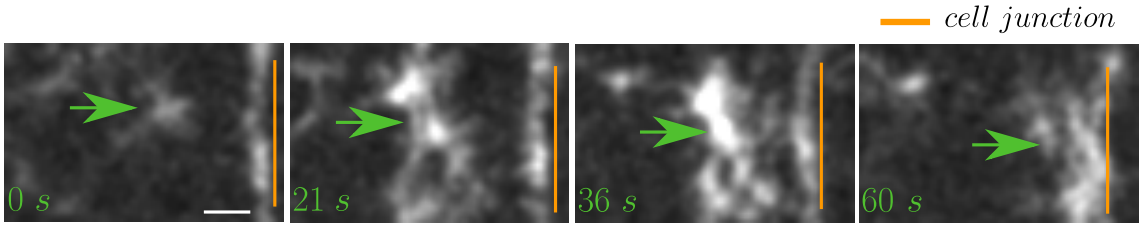

Figure 4.1. Actomyosin Pulsation and flow seen in fluorescent myosin (RLC-mCherry) shows *emergence* of an actomyosin rich region(s). Periodic assembly (0-21s), flow (21-60s) and disassembly (36-60s) of these actomyosin rich regions result in remodeling of the cell junctions [12]. The green arrow highlights the actomyosin rich region and the scale bar size is $1\,\mu m$ (leftmost panel).

Next we reiterate the hydrodynamic theory briefly then we present the features of active elastomer dynamics from the numerical solution.

4.2 Equation of motion

In this section we reiterate some basics of the active hydrodynamic description that we proposed earlier and then discuss the form of active stress and how it can be understood in terms of the *effective elastic free energy* and a purely myosin dependent active stress.

Derived from Eq.3.13 and Eq.3.14, the one dimensional equations are given by

$$\Gamma \dot{u} = \partial_x \left(\sigma^e + \sigma^d + \sigma^a \right) \tag{4.1}$$

and

$$\dot{\rho}_b + \partial_x (\dot{u} \rho_b) = D \partial_x^2 \rho_b - k_{u0} e^{\alpha \partial_x u} \rho_b + k_b \rho \,. \tag{4.2}$$

The hydrodynamic variables here are the actin mesh displacement field $u(x,t)$, the actin mesh density $\rho(x,t)$ and the density of the bound myosin minifilaments

$\rho_b(x,t)$. Now at a coarse graining length scale larger than the dissipative length scale l_d where the internal viscous dissipation of the mesh becomes comparable to the frictional dissipation from the ambient fluid ($l_d = \sqrt{\frac{\eta}{\Gamma}}$), we can take the frictional dissipation to be the dominant dissipative mechanism in the system ($\Gamma\dot{u} >> \partial_x\sigma^d$) and neglect internal viscous dissipation. We also take mesh density to be slaved by local deformation as mentioned earlier.

The elastic stress is $\sigma^e = B\epsilon$ where the strain is defined as $\epsilon = \partial_x u$. Now the the active stress is given by

$$\sigma^a = -\frac{\Delta\mu\zeta_1\rho_b}{1+\zeta_2\rho_b}\left(\chi(\rho_0) - c\chi'(\rho_0)\epsilon + \frac{1}{2}c^2\chi''(\rho_0)\epsilon^2 + \dots\right). \tag{4.3}$$

Now separating the ϵ dependent terms and combining them with the elastic stress already defined, we can rewrite an *effective elastic free-energy* given by

$$\Phi(\epsilon) = \frac{1}{2}K_2(\rho_b,\rho_0)\epsilon^2 + \frac{1}{3}K_3(\rho_b,\rho_0)\epsilon^3 + \frac{1}{4}K_4(\rho_b,\rho_0)\epsilon^4\,. \tag{4.4}$$

Here K_i $(i = 1,2,3)$ are density dependent coefficients given by $K_2 = B + \frac{\zeta_1\Delta\mu\rho_b}{1+\zeta_2\rho_b}c\chi'(\rho_0)$, $K_3 = -\frac{\zeta_1\Delta\mu\rho_b}{1+\zeta_2\rho_b}c^2\frac{\chi''(\rho_0)}{2}$ and $K_4 = \frac{\zeta_1\Delta\mu\rho_b}{1+\zeta_2\rho_b}c^3\frac{\chi'''(\rho_0)}{6}$. Here $\zeta_1 < 0$ and $\chi'(\rho_0) > 0$, so K_2 goes from being positive to negative as contractility increases. The signs of the other constants are: $\zeta_2 > 0$, $\chi''(\rho_0) > 0$ and $\chi'''(\rho_0) < 0$, so that K_3 and K_4 are always positive. The quartic term with $K_4 > 0$ ensures that the local compressive strain does not grow without bound, as a consequence of steric hinderance, filament rigidity or crosslinking myosin.

The effective elastic free-energy $\Phi(\epsilon)$ that emerges as a consequence of activity, has three important features : (i) for weak active contractile stress, the minima at $\epsilon = 0$ gets shallower, indicating that the elastic stiffness B decreases, (ii) as we increase the active stress, there appears another minimum at $\epsilon = \epsilon_0$ (iii) for large active stresses, the $\epsilon = 0$ state can be unstable, with $K_2 < 0$ (see Fig.4.2). The last scenario presents a case of strained stable state ($\epsilon \neq 0$) [45] which we have already encountered and defined as contracted state.

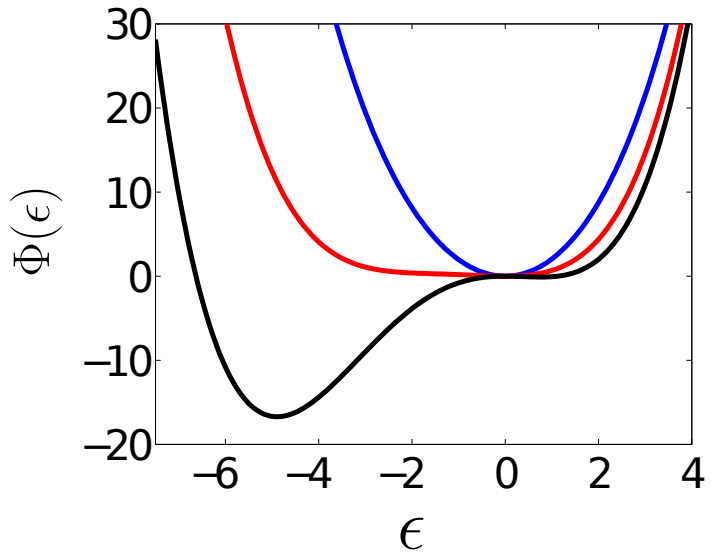

Figure 4.2. Effective elastic free-energy of the active elastomer : Effective elastic free energy $\Phi(\epsilon)$ as a function of strain for three different values of active stress. At low active stress, Φ has a single minimum at $\epsilon = 0$, the free-energy profile has a lower curvature (corresponding to lower renormalized elastic modulus) than the passive elastomer. At intermediate values of active stress, there appears a second minimum at $\epsilon = \epsilon_0$. At higher values of active stress, the minimum at $\epsilon = 0$ becomes unstable.

We define the remaining purely ρ_b dependent part of active stress as $\bar{\sigma}^a(\rho_b) = \frac{-\zeta_1 \Delta\mu \rho_b}{1+\zeta_2 \rho_b} \chi(\rho_0)$. Finally we arrive at the resulting equation of motion given by

$$\Gamma \dot{u} = \partial_x \Phi'(\epsilon) + \partial_x \bar{\sigma}^a(\rho_b) \tag{4.5}$$

and

$$\dot{\rho_b} = -\partial_x(\rho_b \dot{u}) + D\partial_x^2 \rho_b - k_{u0} e^{\alpha \partial_x u} \rho_b + k_b \rho \,. \tag{4.6}$$

Next we present the results of numerical solutions of these above equations.

4.3 Steady state phases and phase diagram

The final set of equation of motion (Eq.4.5 - 4.6) is numerically solved with periodic boundary conditions using a finite difference scheme (see Appendix.A.2 for details). Initial conditions are small amplitude random fluctuations about the homogeneous unstrained state. The numerical phase diagram, displayed in Fig. 4.3, shows several

new features compared to the linear phase diagram, which we discuss below.

The two features that are expected to arise from nonlinear effects, namely, the tempering of the linear instabilities to obtain both finite-amplitude oscillatory and finite-amplitude contractile collapse phases at intermediate and high contractile stresses, respectively, show up in the steady state phase diagram, Fig. 4.3. The corresponding kymographs in the bound myosin density (Fig. 4.4) show the appearance of these steady state at late times. The time development of configurations in these phases can be summarized as follows - starting from a generic state with small random fluctuations about the homogeneous unstrained state, the configuration quickly results in a spatially heterogenous (un)binding of myosin filaments onto the actin mesh, transiently generating localized compression. This will increase the local concentration of actin, which in turn will facilitate more myosin recruitment and hence more compression. This local compression will be resisted by an elastic restoring force, and the resulting strain can lead to an enhanced myosin unbinding. If it does, this will lead to a relaxation of the compressed region, to be followed by another round of binding-compression-unbinding leading to the observed oscillations. In this spontaneous oscillating phase, the frequency gets smaller with increasing the active stress or decreasing unbinding rate [11]. On the other hand, if myosin unbinding does not occur fast enough, the elastomer will undergo a contractile instability, to be eventually stabilised by nonlinear effects such as steric hinderance and filament rigidity.

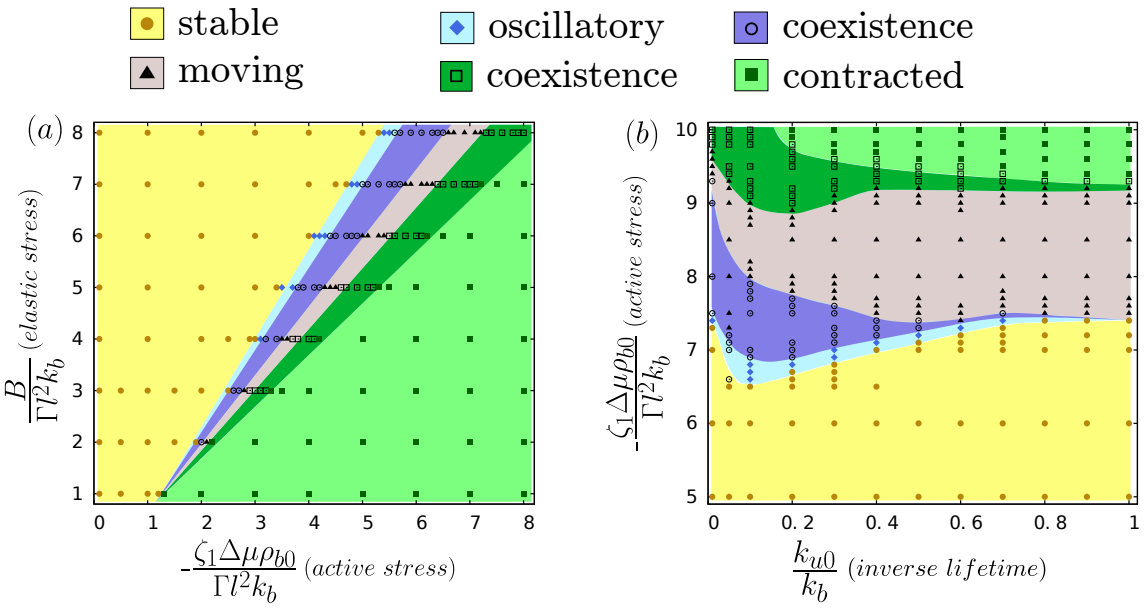

Figure 4.3. Phase diagram obtained from numerical solutions of Eqs. (4.5-4.6) : (a) Effective elastic stress density vs. contractile stress density, with $k = 0.1$. (b) Effective contractile stress density vs. inverse-lifetime, with $B = 5$. The phases are (i) Stable (yellow), (ii) spontaneous Oscillatory (blue), (iii) spontaneous Moving (grey) and (iv) contractile Collapse (light-green). The regions marked violet and dark-green are the coexistence phases - the oscillatory-moving coexistence (open circle) and the collapse-moving coexistence (open square). Apart from the new phases, the topology of the phase diagrams are roughly similar to the linear stability diagram (Fig. **??**b), except for the upturn of the phase boundaries towards larger active stress in (b), which arises from the non-linear strain-dependent unbinding. Symbols are points at which numerical solutions have been obtained. Rest of the dimensionless parameters are, $\alpha = 3$, $c = 0.1$, $\chi(\rho_0)\zeta_1 = -0.5$ and $\zeta_2 = 0.1$.

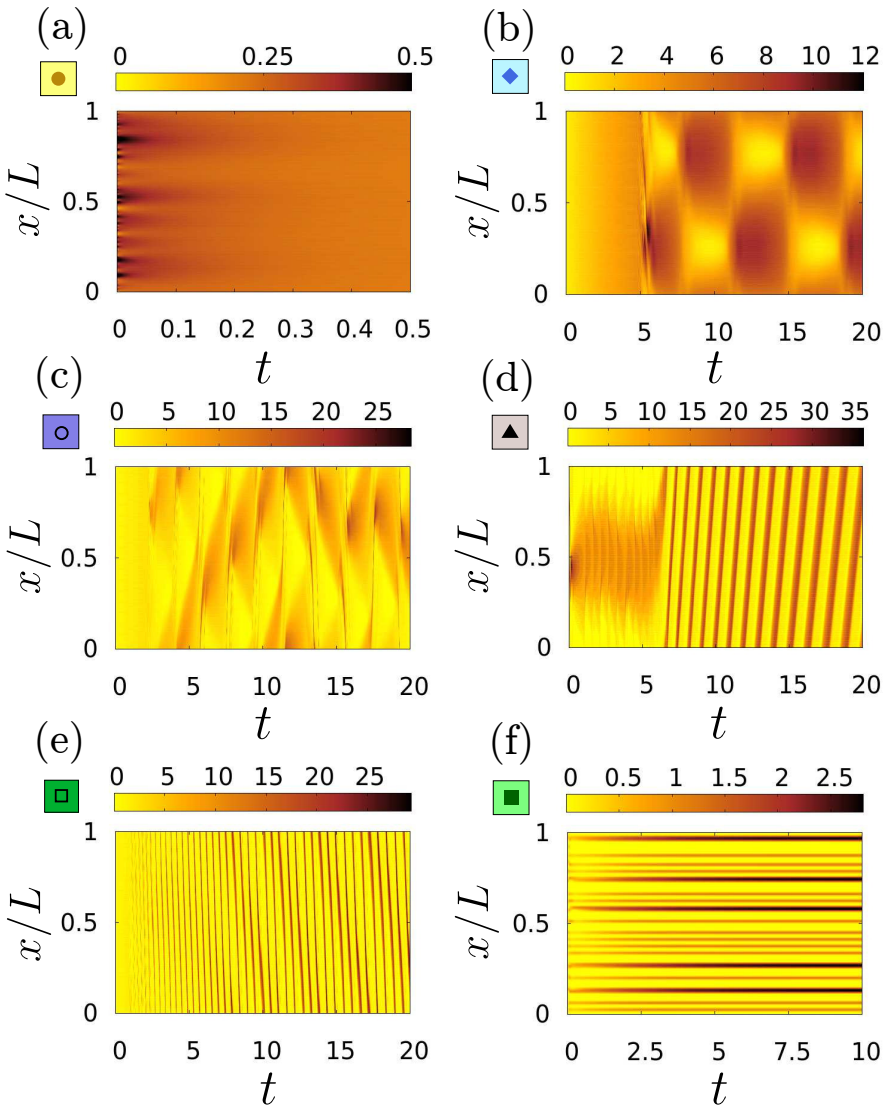

Figure 4.4. Kymographs of the bound myosin density for Stable (yellow), spontaneous Oscillatory (blue), spontaneous Moving (grey) and contractile Collapse (light-green) phases (indicated by the colour and symbol on the upper left corner) is shown in (a), (b), (d) and (f), respectively. The kymographs for the coexistence phases - the oscillatory-moving coexistence (violet, open circle) and the collapse-moving coexistence (dark-green, open square) are shown in (c) and (e) respectively.

Additionally, there is a wholly unexpected feature that emerges from a numerical solution of the full nonlinear equations. In the parameter regime between the oscillatory and the contractile collapse phases, there appears a moving phase (Fig. 4.3), where spatially localized actomyosin-dense regions (which we later identify as traveling fronts) spontaneously move to either the left or right boundary. In the regimes

between the pure moving phase and the oscillatory and collapse phases, lie the coexistence phases where the moving phase coexists with oscillations and collapse, respectively. The corresponding kymographs in the bound myosin density (Fig. 4.4) show the appearance of these steady state at late times. We may understand the occurrence of these phase transitions using a simple argument based on the relative time scales of these dynamical events, as displayed in Fig.4.5.

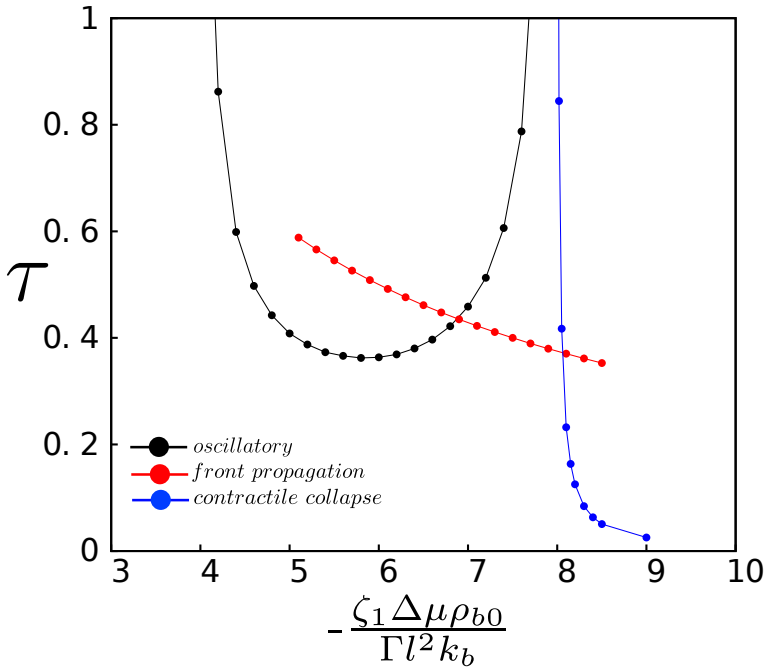

Figure 4.5. Time scale of various events - oscillation, front propagation and contractile collapse - as a function of the active stress, obtained from theory, shows that with increasing active stress one first encounters the oscillatory phase, then the pulse propagation and finally the collapse. The boundaries of these transitions support coexisting behaviours. The oscillatory and contractile collapse timescale values are calculated from the one mode analysis with the rest of the parameters fixed at $B = 8$, $\alpha = 1$, $c = 0.1$ and $k = 5$.

Several qualitative assertions follow immediately from the affine theory, such as : (i) the existence of bounded (finite-amplitude) oscillations requires both strain-dependent unbinding and turnover of myosin, (ii) the coexisting oscillation-moving and collapse-moving phases cannot be obtained in the absence of strain-dependent unbinding, (iii) advection is a necessary condition for front movement. We now look more closely at the dynamics of actomyosin dense regions and compare the results

of the affine theory with early time dynamics of myosin dense regions in-vivo.

4.4 Nucleation, growth and coalescence

During the observed *pulsation* and *flow* in the germband cells, actomyosin rich regions form through a process of nucleation, growth and coalesce. This starts with nucleation of small actomyosin rich regions(Fig.4.6a 0-10s) then these regions grow and subsequently coalesce (Fig.4.6a 10-20s) to form a big actomyosin rich region which then proceed to flow and finally disassociate near a vertical junction.

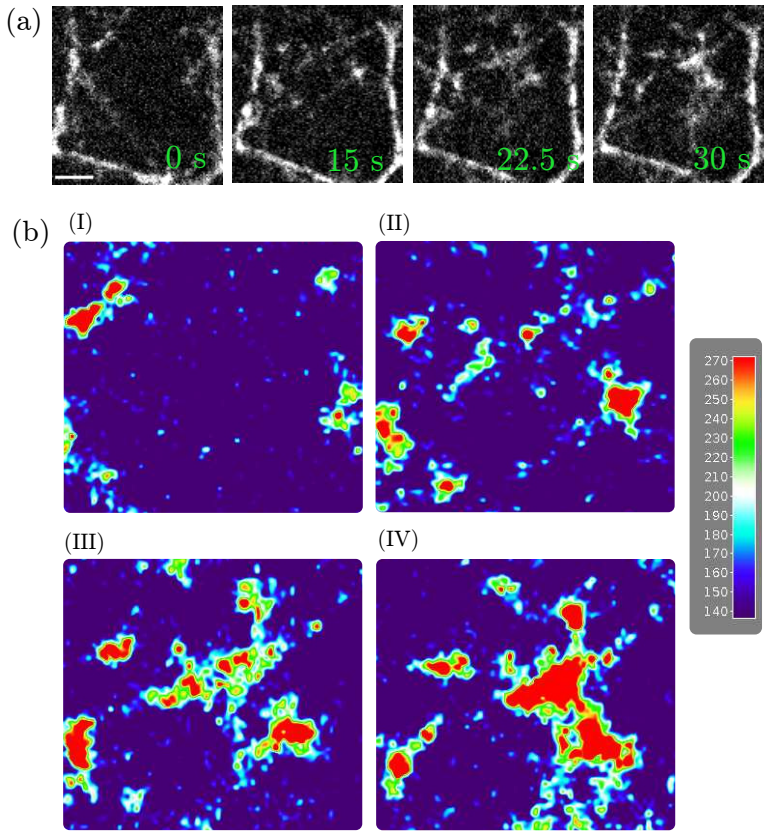

Figure 4.6. (a) Nucleation (0-10s), growth (10-15s) and coalescence (15-20s) during actomyosin *pulsation* and *flow* in germband cells observed via intensity variation of fluorescently tagged myosin (RLC-mCherry). (b) A closer look into the process of nucleation, growth and coalescence, (I-IV) refer to a zoomed in version of the four panels above starting the leftmost panel.

In the moving regime, the effective 'elastic free-energy' functional $\Phi(\epsilon)$ develops

a second minima at $\epsilon = \epsilon_0$ corresponding to a local compression due to contractility (Fig.4.2). Initiation of movement starts with the nucleation of actomyosin-dense regions, which grow and coalesce to form larger actomyosin-dense regions. This is best seen using a space-time analysis of Eqs. 4.5-4.6 with initial conditions stated above. Kymographs of the spatial profile of bound myosin density, calculated from the theory, show nucleation and growth ($0 < t < 0.15$) followed by coalescence ($0.15 < t < 0.7$) and eventual movement ($t > 0.7$) (Fig. 4.7 a,b). This space-time behaviour accurately recapitulates the early time dynamics of medial myosin in-vivo as seen from the experimental kymographs, Fig. 4.7 c,d.

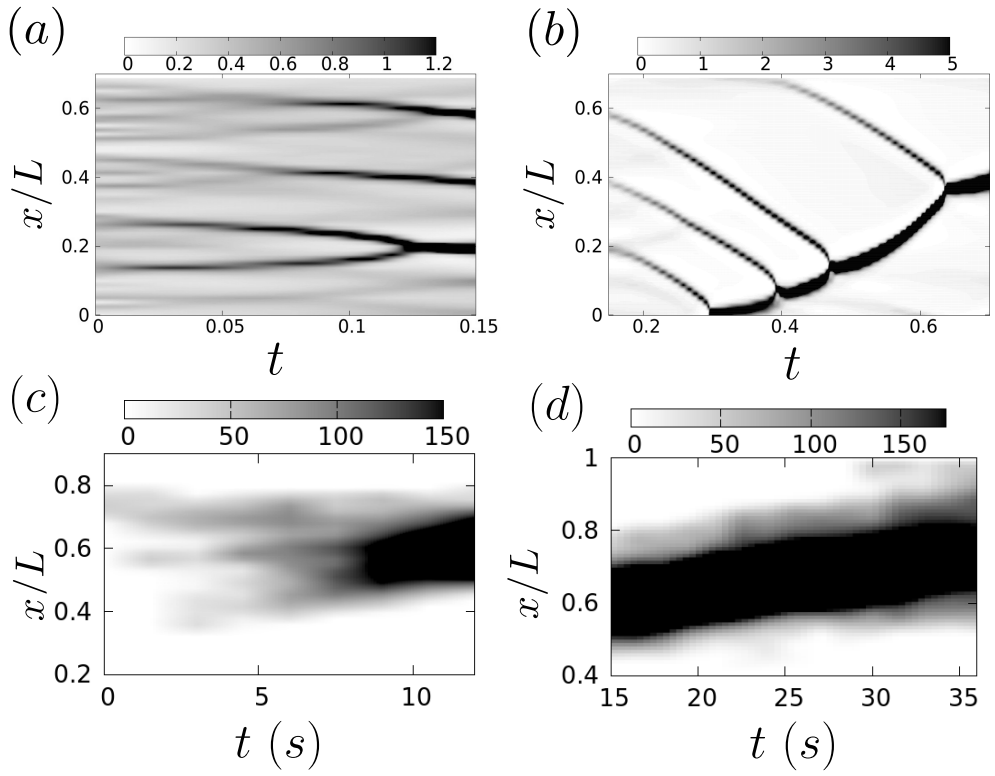

Figure 4.7. Kymographs of bound myosin density from theory and experiment : (a-b) Kymograph of the spatial profile of bound myosin density from theory, shows nucleation and growth ($0 < t < 0.15$), followed by coalescence ($0.15 < t < 0.7$) and movement ($t > 0.7$). Here $B = 6$, $-\zeta_1 \Delta\mu = 5.5$, $k = 0.5$, $\alpha = 1$ and $D = 0.15$. Rest of the parameters as in Fig. 4.3. (c) Kymograph of the spatial profile of labeled myosin from experiment, shows nucleation and growth ($0 < t < 5$s), followed by coalescence ($5 < t < 10$s) and (d) eventual movement of the formed actomyosin rich region ($t > 10$s).

4.5 Asymmetric profile of traveling front

Here we investigate the origins of the spontaneous movement of the actomyosin-dense region. We study the configuration of the localized actomyosin-dense region just prior to movement, and find that it assumes a symmetric localized profile (Fig. 4.8a) within which the strain $\epsilon = \epsilon_0$ (the second minimum) where $\Phi'(\epsilon) = 0$. The active stress within this region is higher than outside, the resulting gradient in stress should induce inflowing myosin currents from either side of it. We verify this by monitoring the fluxes J_L and J_R, coming from the left and right of this symmetric profile. Over time, owing to stochasticity either in the initial conditions or the dynamics, there is a net flux,$J_L + J_R$, from either the left or the right (Fig. 4.8b), leading an asymmetric profile (Fig. 4.8c), and hence a gradient of ρ_b across the profile. This marks the onset of the traveling front. This feature also appears to be present in the early time dynamics of the moving myosin profiles observed in-vivo, as seen in Fig. 4.8d-f.

The affine theory predicts that the myosin density profile is asymmetric and moves as a traveling front, with a constant velocity while maintaining its shape (as long as there are no further coalescence events). We confirm this using a variety of initial conditions of the bound myosin density ρ_b, including starting with a single symmetric gaussian profile. We analyze the asymmetric profile of the traveling front by transforming to the co-moving frame $x \pm vt$ (Fig. 4.9).

We find that within the traveling front, the strain takes a value slightly more compressed relative to ϵ_0, the value of the strain at the second minima, where $\Phi' = 0$. The traveling front is stably compressed in a force-free state (Fig. 4.9a,b). The asymmetric myosin profile gives rise to a gradient in the active stress (Fig. 4.9c), which provides the propulsion force for the traveling front to move to the right in Fig. 4.9c.

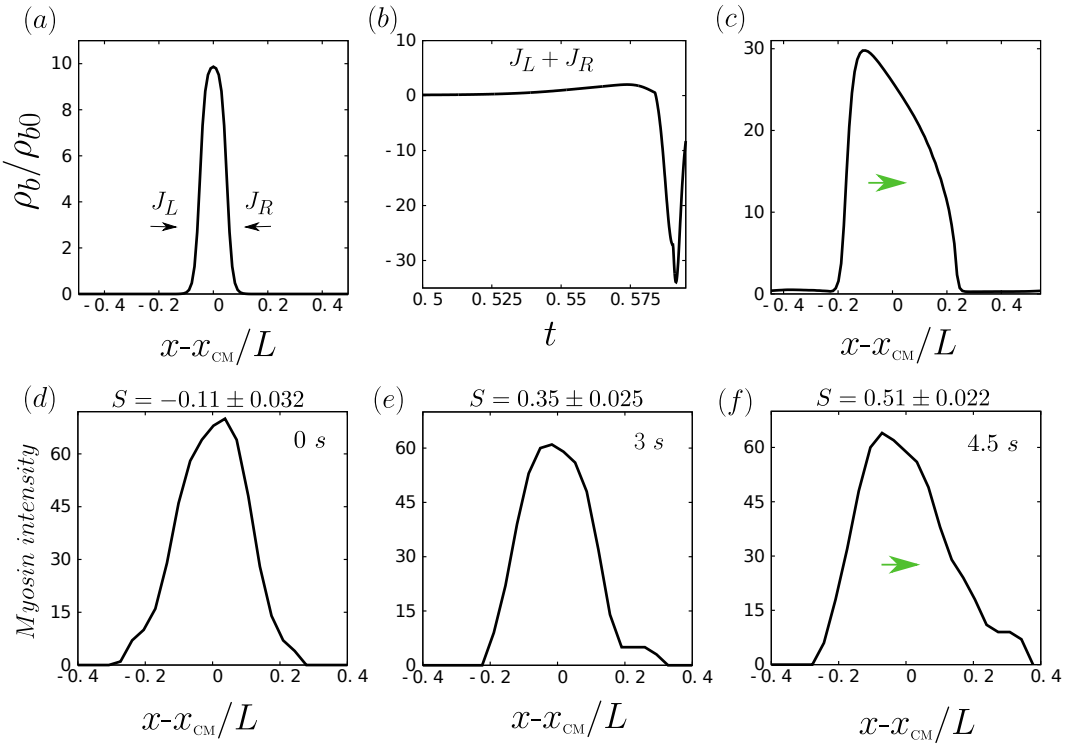

Figure 4.8. Time evolution of ρ_b, the density profile of bound myosin in a cluster prior to movement : (a) Prior to movement the myosin density profile is seen to be symmetric, following which we compute the instantaneous left-right fluxes, $J_{L,R}$ of myosin drawn into it. (b) Time evolution of the algebraic sum $J_L + J_R$, shows that after a while, there develops a net flux in one direction as a precursor to the asymmetric traveling front. (c) Emergence of the asymmetric traveling front which moves towards the right in a shape-invariant manner. (d-f) Myosin intensity profiles from experiments, which shows how an initial stationary symmetric myosin profile at $t = 0$, finally evolves to an asymmetric profile at $t = 4.5\,\mathrm{s}$, which then travels to the right. The degree of shape asymmetry of the profiles is described by the skewness S, the standard error of mean(s.e.m.) reported is due to projection of the images to one dimension.

4.6 Dynamics of traveling front

The dynamics of the traveling front that emerges from the affine theory is local, its propulsion is therefore independent of the boundary or the distance from the boundary. We calculate the velocity of the traveling front by integrating Eqs. (4.5-4.6) across the scale Ω of the traveling front in the co-moving frame. This leads to the formula, $v = \Gamma^{-1} \int_\Omega \partial_x \sigma^a \equiv \Gamma^{-1} f_{act}$, which states that the velocity depends only

on the shape asymmetry of the front; if the shape is maintained over time, then the velocity is a constant. In Fig. 4.9d, we plot the f_{act} versus the velocity and show that they are proportional to each other over a large range of active and elastic stresses. We will later make connection with experiments, where it is convenient to use the shape-asymmetry or skewness of the myosin profile, $S \equiv \frac{\int_\Omega (x-x_{CM})^3 \rho_b(x)}{\left(\int_\Omega (x-x_{CM})^2 \rho_b(x)\right)^{3/2}}$, as a proxy for the driving force. We find that the traveling front velocity increases with increasing skewness before saturating at larger velocities (inset of Fig. 4.9d).

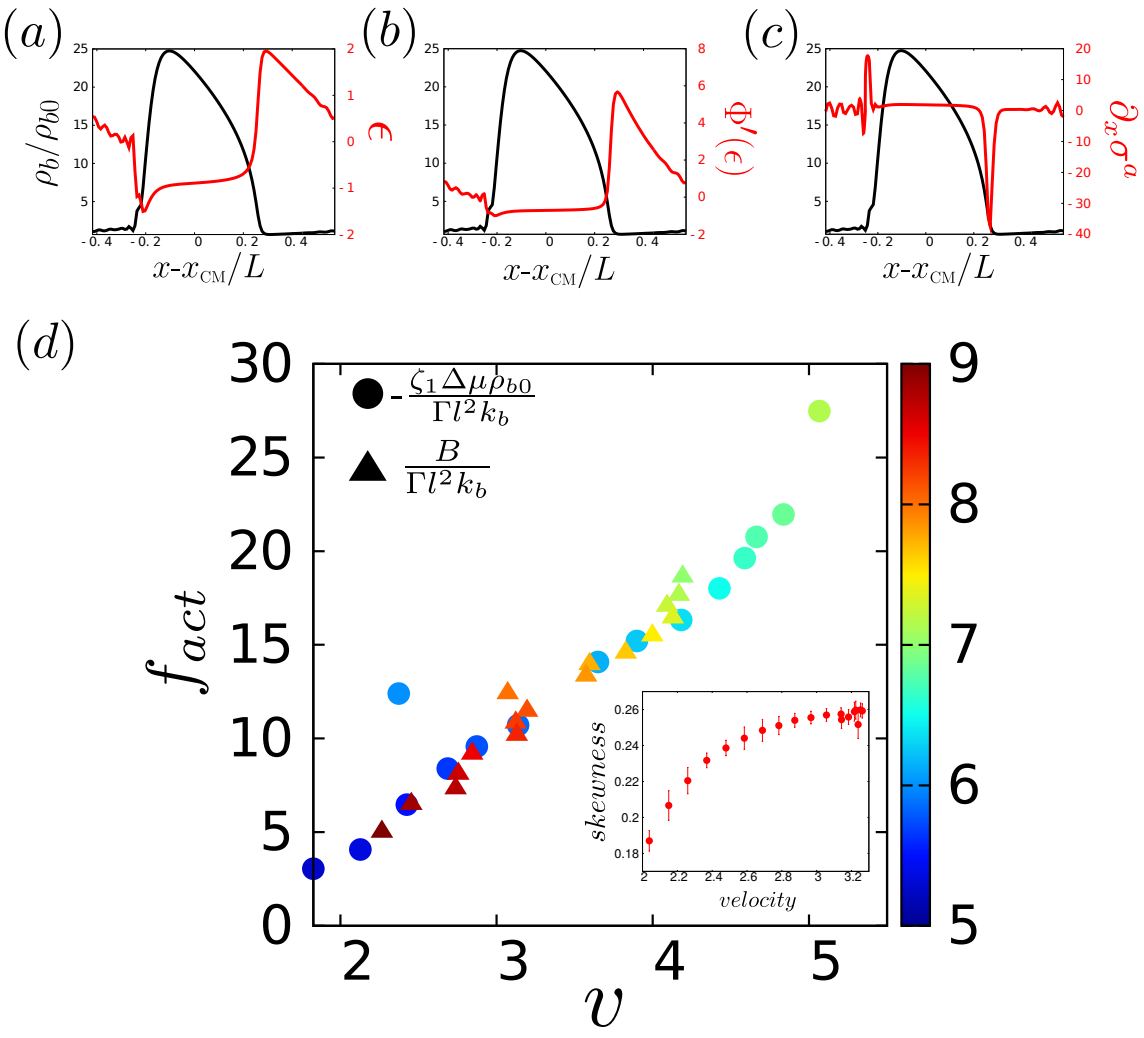

Figure 4.9. Anatomy of the traveling front in the co-moving frame : (a) Spatial profile of Excess bound myosin density (black) and strain ϵ (red) profile, (b) Spatial profile of Myosin density and derivative of the effective elastic free energy $\Phi'(\epsilon)$ (red), (c) Spatial profile of myosin density and active force (red). Horizontal axis is distance from centre of mass position, x_{CM}. Here $B = 6.0$, $-\zeta_1\Delta\mu = 4.8$, $k = 0.2$, $\alpha = 1.0$ and $D = 0.25$. (d) Theory predicts that the traveling front velocity is proportional to the net active force integrated over the front profile across the moving front. We demonstrate this fact from a numerical solution of the dynamical equations by varying the parameters of the active stress (circle) and the elastic stress (triangle). for different values of B (with $-\zeta_1\Delta\mu = 6.0$, $k = 0.2$ and $D = 0.15$ fixed) and $-\zeta_1\Delta\mu$ (with $B = 8.0$, $k = 0.2$ and $D = 0.15$ fixed). Rest of the parameters as in Fig. 4.3.The colour bar shows the magnitude of these stresses in dimensionless units. (inset) Skewness of bound myosin profile in the traveling front versus velocity, obtained by varying the contractile stress $-\zeta_1\Delta\mu$ from $3-4$, shows a linear increase followed by saturation. The other dimensionless parameters are : $B = 4$, $k = 0.2$, $D = 0.1$, $\alpha = 1$ and $c = 0.1$. The error bars are calculated as s.e.m.

Affine theory predicts moving deformation :
It is important to note that the movement of the actomyosin-dense region arising from affine deformations of the active elastomer is a moving deformation of the actomyosin mesh, and once established, is not contingent on myosin turnover, as shown in Fig 4.10a. One could also sustain a traveling front or moving deformation of the actomyosin mesh by ensuring a differential myosin binding and unbinding rates at the leading and trailing edges of the front, in a kind of treadmilling movement, Fig 4.10b. None of these however is associated with mass flow of actin and myosin. Indeed, the dynamical equations describing the active affine elastomer, Eqs. 4.5-4.6, bear a close resemblance to the generalized FitzHugh-Nagumo model, an excitable system which is known to exhibit traveling front solutions [48].

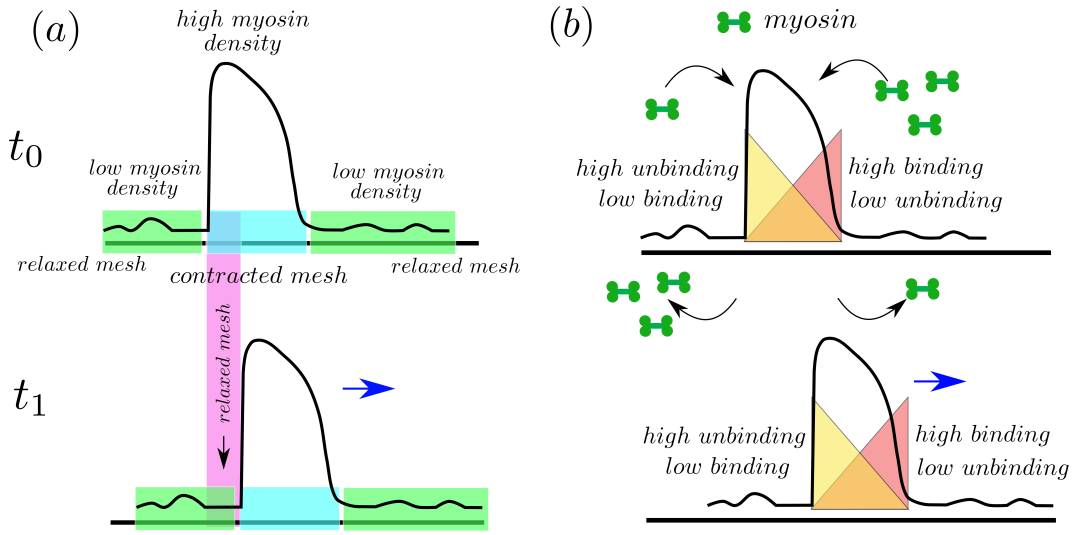

Figure 4.10. Possible mechanisms for the movement of actomyosin-dense structures in an active affine elastomer : (a) moving deformation of the actomyosin mesh without turnover, implying a traveling front, and (b) moving deformation of the actomyosin mesh with differential myosin binding unbind rates at the leading and trailing edges of the front.

4.7 Spatiotemporal Chaos in coexistence phase

We found two dynamical phases where coexisting oscillation-movement and movement-collapse can be observed (see Fig.4.4 c,e). Now to understand these phases better we carry on further analysis. Irregular and aperiodic dynamics of the bound myosin

density and displacement field poses a possibility of spatiotemporal chaos in the coexistence phases. We have already seen emergence of chaotic behaviour in mode truncated studies (*Chapter 3*) upon introducing advective nonlinearity. Here we see long-time spatiotemporal chaotic behaviour in the coexistence phases, probably as a result of competing oscillatory-advective and collapse-advective effects in the system.

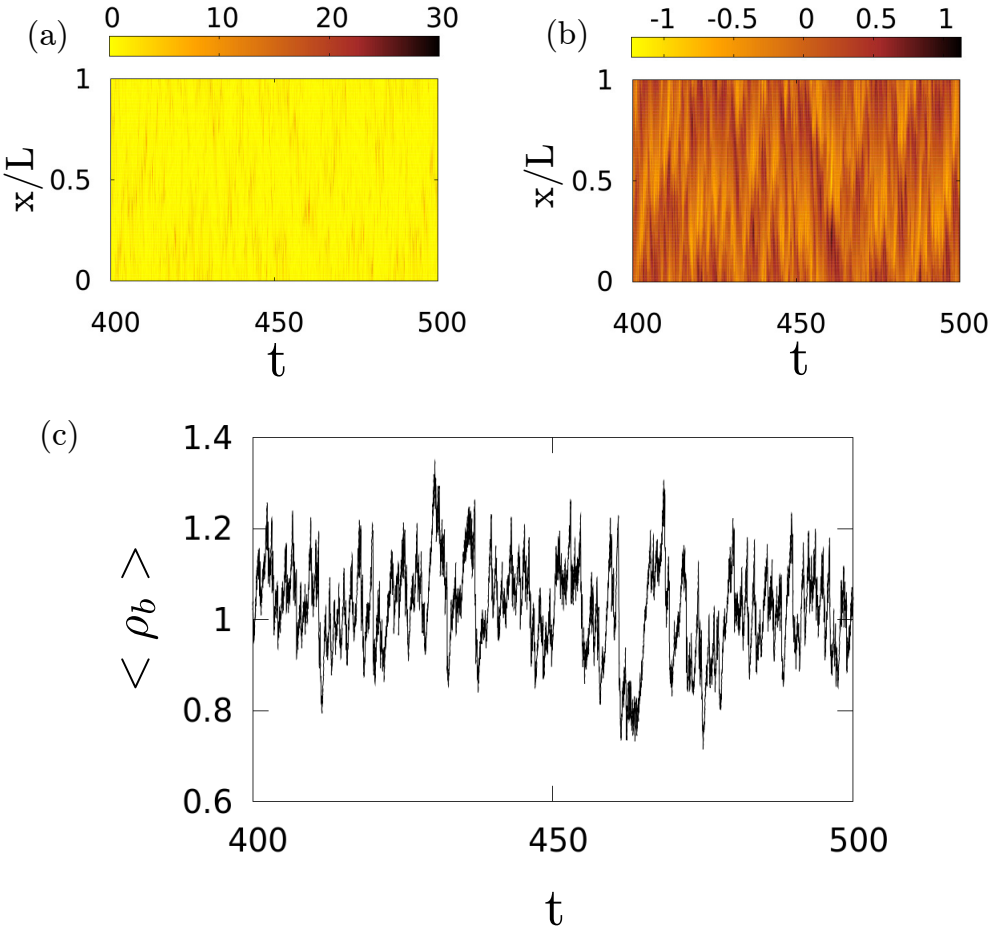

Figure 4.11. Spatio-temporal chaos in the kymograph of (a) bound myosin density and (b) displacement field. (c) Time series of the mean bound myosin density shows aperiodic, chaotic behaviour in long times. Parameter values used for the above are $B = 8$, $-\zeta_1 \Delta\mu = 7.5$, $\alpha = 3$, $k = 0.2$, $D = 0.1$ and other parameters are same as in Fig.4.3.

Proceeding further with the analysis of the chaotic behaviour we calculate the subsystem Lyapunov spectra [64, 62, 63] from bound myosin density space-time

evolution in coexistence phase. The results show increasing number of positive Lyapunov exponents (N_L) (Fig.4.12 a) and value of the maximum Lyapunov exponent (L_{max}) (Fig.4.12 b) with increase in sub-system size (n_s), features of spatiotemporal chaotic behaviour[65].

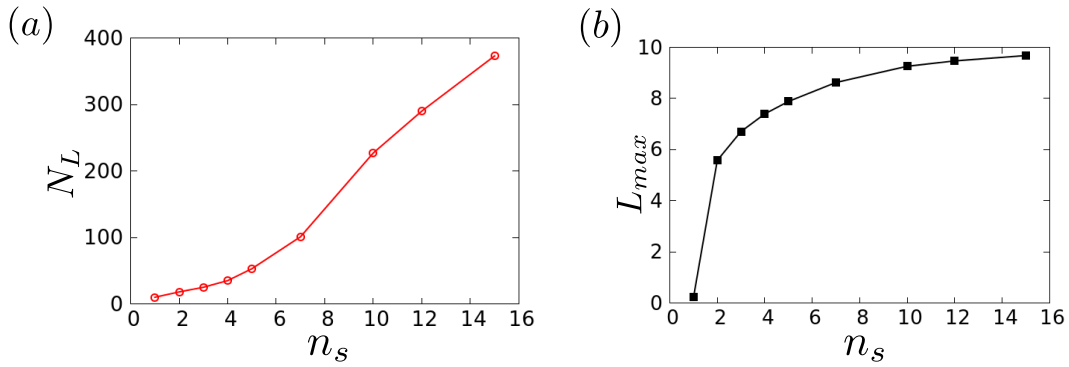

Figure 4.12. Lyapunov spectra calculated from bound myosin density space-time evolution in coexistence phase shows (a) increasing number of positive Lyapunov exponents and (b) increase in the value of the maximum Lyapunov exponent with increasing sub-system size. These features indicate spatiotemporal chaotic behaviour in coexistence phases.

4.8 Concluding remarks

Here We conclude our study of the affine hydrodynamical description of actomyosin as active elastomer. While we allowed turnover of only active force generator myosin motors and assumed no turnover for the elastomer network, this description could successfully bring out important features like spontaneous oscillation and spontaneously propagating fronts which bears similarity with the observed *pulsation* and *flow* during morphogenesis of germband tissue. This description could explain the actomyosin dynamics in low contractility regime where an actomyosin rich region form through nucleation, growth and coalescence and we established that moving actomyosin regions are driven by local contractile forces generated by an asymmetric myosin density profile.

This study of the affine hydrodynamics of active elastomer predicts deformation flow in actomyosin and it is very important to understand the validity of this prediction. We finally address this concern in the next chapter where we take forward this theory to include turnover of the network and present a comprehensive comparison

of the theoretical results and the *in vivo* experiments.

End of Chapter

Chapter 5

Non-affine dynamics of apical actomyosin : Transient network description

5.1 Introduction

In this study we have described the medial actomyosin crosslinked mesh as an active elastomer embedded in a viscous fluid, subject to active contractile stresses arising from the binding of myosin minifilaments [84, 43, 35, 44]. So far we have only considered affine deformation of the mesh (neglecting the network remodeling) and turnover of myosin motors only. Here in this chapter we argue the regime of validity of this affine description and propose an active elastomer with network remodeling. This new feature of network remodeling in the elastomer mesh involves breakage and reformation of crosslinks, allowing *non-affine* deformations [71, 72] to take place. We discuss the importance of perceiving the actomyosin system as a *transient active elastomer network* then present a rudimentary theoretical description of active elastomer with turnover of all of its components. Finally we compare the features of active elastomer dynamics that we have developed so far with *in vivo* experiments on *Drosophila* germband extension.

5.2 Where the affine theory works and where we need a non-affine description

Here we provide a justification for treating this as an active elastomer with turnover, rather than directly as an active fluid, as was done in the context of *C. elegans* embryo [51, 52].

We first note that, when the time scales of turnover of the actin mesh or crosslinkers are much smaller than the time scales of macroscopic processes of interest, then the stress relaxation is set by the turnover time scale, and the system should be treated as a fluid. Alternatively, when the actin mesh or crosslinker turnover time scales are much larger than the time scales of macroscopic processes, then the system should be treated as a dissipative elastic medium. The interpretation in these two extreme regimes is unambiguous. However, Fluorescence recovery after photobleaching(FRAP) measurements in germband cells, reveal an actin turnover time of around $10 - 20\,\mathrm{s}$ [12], which is the same order as the time scale of nucleation and growth, around $10 - 20\,\mathrm{s}$, and the period of medial actomyosin pulsation, around $50 - 100\,\mathrm{s}$ [12, 83, 11]. Indeed a more detailed look at the movies of myosin [73], show a distribution of time scales and a range of dynamical regimes, starting from the appearance and disappearance of small myosin-rich speckles over a time scale of 5-10 s. This suggests that the appropriate description should span the short time elastomeric and the longer time fluid-like regimes. As mentioned in the Introduction, we do this by starting out with an elastic description of a mesh, where the local deformations induced by myosin binding and release are affine. Increased myosin binding can lead to rapid turnover of actin and crosslinkers, resulting in loss of network integrity and its fluidisation via intranetwork flows; we study this crossover to a non-affine regime. Indeed this strategy of going from the short time elastic to long time fluidisation, as a function of increasing turnover, opens up novel rheological possibilities, such as correlated strain fluctuations and power-law response, which we take up later.

There are several other empirical reasons for starting with an elastomeric description and allowing for turnover of components :

- Current high resolution images of medial actin filaments, both in the germband cells and in the amnioserosa, show two distinct populations of actin filaments - a cell-spanning actin filamentous network which appears connected to the cell boundary and a possibly more rapidly turning over pool of shorter actin filaments (T. Lecuit and B. Dehapiot, unpublished observations). The relative levels of these two architectures of actin filaments is likely to be context dependent.

- The medial actin mesh is connected to the cell junctions; consistent with this, modulating the strength of the coupling of medial actin to the junction via β-catenin affects the pulsation [11].
- Finally, the pulsation of medial actomyosin in these systems appears to be correlated with the oscillations in the area of the apical surface [8, 11, 37, 49].

With this in mind, we will next explore the consequences of actin turnover and network remodeling, the hydrodynamics of a nonaffine elastomer, giving rise to intranetwork flows and consequent fluid-like behaviour.

5.3 Nonaffine elastomer with network remodeling and intranetwork flow

As time progresses and the myosin-dense clusters grow, the local contractile stresses can become large. Such large contractile stresses may dramatically enhance actin turnover and crosslinker unbinding. In Fig. 5.1a, we give a schematic plot of the actin turnover time as a function of contractile stress, and compare it with the time scales of oscillation, front propagation and contractile collapse obtained from the affine theory. Indeed there is experimental evidence that actin turnover times at first increase with increasing contractility [69, 67, 68] - this is likely due to the fact that bound myosin might occupy the binding sites of actin remodeling proteins such as cofilin. There is also evidence that for large levels of contractility, the actin turnover rates are large, possibly because of destabilisation of actin or unbinding of crosslinkers at large contractile stress. We make the plausible assumption that the qualitative change in turnover rates is sudden at a stress scale $\sigma^\star$ (Fig. 5.1a), beyond which the deformation of the mesh can no longer be considered affine and one needs a description of *nonaffine* deformations of the active elastomer.

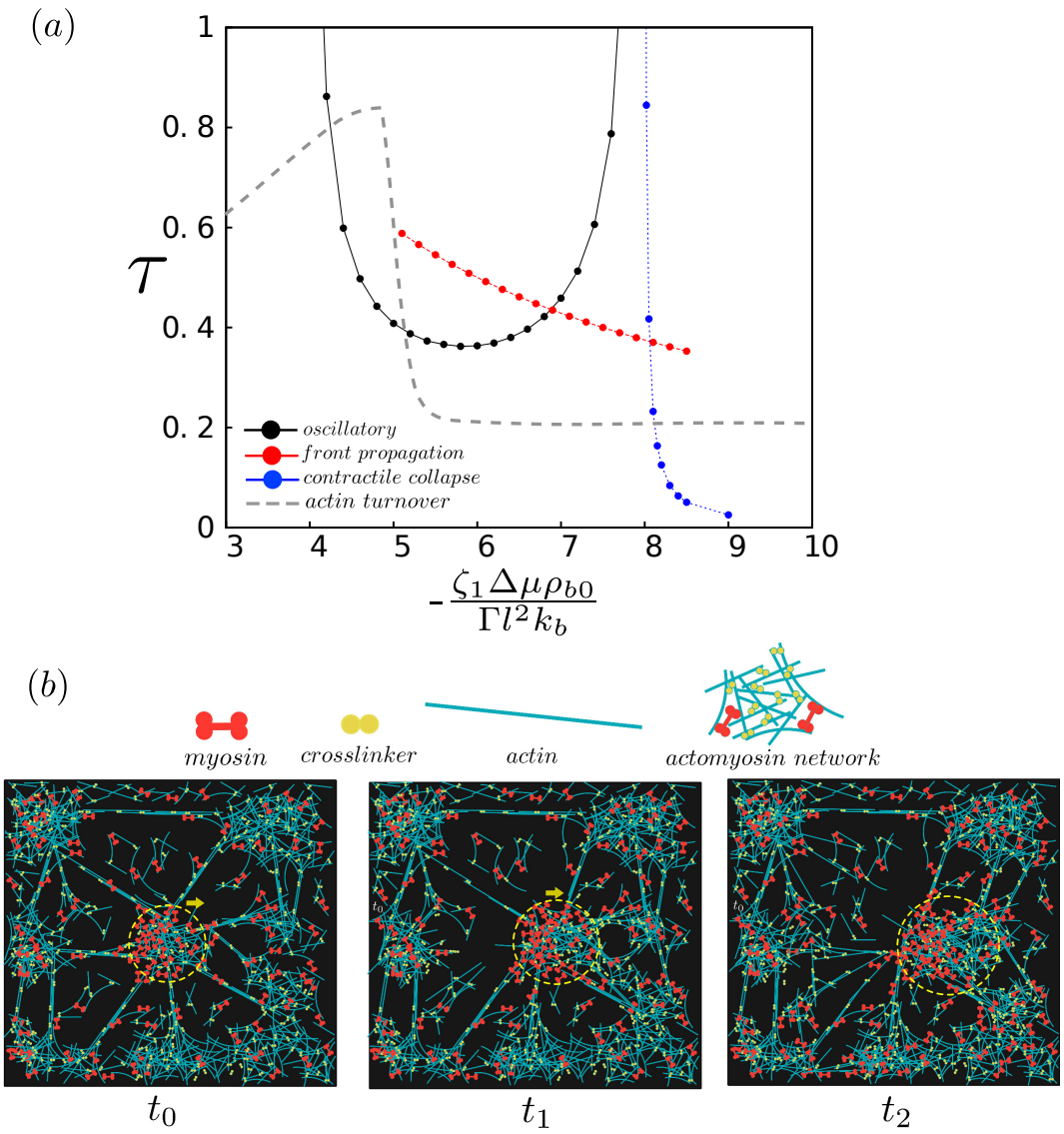

Figure 5.1. Enhanced actin turnover results in nonaffine deformation of the elastomer : (a) Qualitative behaviour of the actin turnover time as a function of contractile stress, consistent with data from [69, 67, 68]. This should be compared with the time scales of oscillation, front propagation and contractile collapse obtained from the affine theory (see, Supplementary Fig. 5). Based on the discussion in the text, we have placed the crossover stress $\sigma^\star$ in the moving regime, thus implying that the crossover to the nonaffine description occurs in this regime. (b) Schematic showing the intranetwork flow of an actomyosin-dense region (enclosed within the yellow circle) resulting from active stress induced unbinding and rapid turnover of the actin in a transient actomyosin network.

We use this insight to arrive at a nonaffine description of the active elastomer.

Consider a disordered mesh comprising actin filaments linked to each other by crosslinkers such as α-actinin and myosin (we will assume that this is an unentangled network). The bound myosin locally compresses the mesh here and there, recruiting more myosin in the process. When the local bound myosin concentration goes beyond a threshold (so that the configuration now samples the second minimum of the effective free energy, $\Phi(\epsilon)$), the local compression is high and the mesh surrounding this myosin-dense region gets significantly stretched. This could lead to a tearing or ripping of the mesh, either via the unbinding of crosslinkers, destabilisation of actin or by the sliding and slipping of filaments past each other. This mesh breakage subsequently heals by the rebinding of crosslinkers or actin itself.

With this picture in mind, we refer to several seminal studies on thermally activated reversibly crosslinked networks in the context of the dynamic properties of physical gels [70, 71, 50]. The most dramatic feature of such reversible networks is its internal fluidity, where each chain can diffuse through the entire network due to the finiteness of the crosslinker life time, in spite of being partially connected to the macroscopic network structure in the course of movement. These systems thus flow under an external stress on time scales longer than the crosslinker dissociation time.

In the context of actomyosin networks, the disrupting influence of filament turnover and the ultimate fluidisation has been the subject of some study [74]. In a very recent submission, the healing effect of turnover has also been investigated, and long range network flows have been demonstrated in simulations of a model actomyosin network [75].

In the present context, when the local bound myosin concentration rises beyond a threshold and attains an asymmetric density profile, it induces mesh breakage in its surrounding regions. This actomyosin-dense region can move through the entire network due to the finiteness of the crosslinker life time, in spite of being partially connected to the macroscopic network structure in the course of movement. These systems should thus exhibit flow under an internal active contractile stresses on time scales longer than the crosslinker dissociation time. This is depicted in Fig 5.1b.

To describe this mathematically, it is convenient to define physical quantities coarse-grained over the scale of the actomyosin-dense region Ω, such as $\bar{\rho}_b = \Omega^{-1} \int_\Omega \rho_b$ and $\mathbf{p} = \Omega^{-1} \int_\Omega \boldsymbol{\nabla} \cdot \boldsymbol{\sigma}^a$, the net force-dipole associated with the anisotropy of the myosin profile. We may decompose myosin density configuration $\bar{\rho}_b$ into a sum of

actomyosin-dense clumps (contributing to nonaffine deformations) with volume fraction ϕ and a background (contributing to affine deformations). The equation for the $\bar{\rho}_b$ may now be written as,

$$\dot{\bar{\rho}}_b = -\boldsymbol{\nabla} \cdot (\bar{\rho}_b \mathbf{v}) + D(1-\phi)\nabla^2 \bar{\rho}_b + \mathcal{S}_m(\bar{\rho}_b) \tag{5.1}$$

where, $\mathbf{v} = \phi\beta\left(\mathbf{p} + \gamma \mathbf{p} \cdot \boldsymbol{\epsilon}\right) + (1-\phi)\dot{\mathbf{u}}$, and β is the mesh breakage probability and γ is a strain-alignment parameter.

Flow described here is a consequence of internal active deformations in a transient actomyosin network. We believe this is a new physical phenomenon; unlike the flow observed in physical gels under external load, this active flow is generated by internally generated stresses even in the absence of an external load.

In general, the interplay between actively generated contractile stresses and stress-dependent turnover of components that shows up in many cellular contexts, promises a rich phenomenology with novel rheological consequences. The constant remodeling and turnover of the actin mesh could drive the system from an elastic regime to a fluid-like behaviour via a critical elastic state, characterised by correlated strain fluctuations which might be intermittent. A more complete hydrodynamic theory of nonaffine deformations of a actomyosin network with turnover is a task for the future.

5.4 Comparison with experiments

In making comparisons of the theory presented here with experiments in germband cells in-vivo, it is important to demarcate the affine and nonaffine regimes of the elastomer. The difficulty in doing this, is that we do not know the detailed physical mechanism that would allow us to compute the form of the actin turnover time as a function of contractile stress (Fig. 5.1a). Nevertheless it is clear that starting from an unstrained elastomer, the early time dynamics should be described by the linear and leading nonlinear analysis of the affine theory, as described earlier. The dynamical behaviours described by this analysis include oscillations and contractile collapse, from which we make the following qualitative assertions : (i) the existence of bounded (finite-amplitude) oscillations requires advection, strain-dependent unbinding and turnover of myosin, (ii) the coexisting oscillation-moving and collapse-

moving phases cannot be obtained in the absence of strain-dependent unbinding and advection. As the kymographs in Fig. 4.4 show, these dynamical behaviours start emerging at $t \approx 2$ - which translates to a real time of $\approx 6\,\mathrm{s}$ (*Methods*) -smaller than the actin turnover time of around $10 - 20\,\mathrm{s}$ [12].

The stable, oscillatory and the collapse phases of the affine theory compare favourably with *in-vivo* experiments in germband cell [11]. First, our phase diagram showing the stable, oscillatory and contractile collapse phase is grossly consistent with the experimental phase diagram that appears in [11]. Pulsatory solutions are obtained over a wide range of parameters which include the pure oscillatory and the coexistence phases (panels (b),(c),(e) of Fig. 4.4). In addition, we compare the finer aspects of the oscillatory phase with the pulsation seen in experiments (Fig.5.2). Consistent with [11], we see that advection is crucial to obtain oscillations of bound myosin, both locally (Fig.5.2(a),(b)) and cell-averaged (Fig.5.2(c)). We find a strong correlation between convergent (divergent) advection velocities and increased (decreased) myosin density (Fig.5.2(a)-(c)). Moreover, the amplitude of the oscillation decreases when we reduce actin density ρ_0 (Fig.5.2(d)), consistent with the actin perturbation experiments in [11].

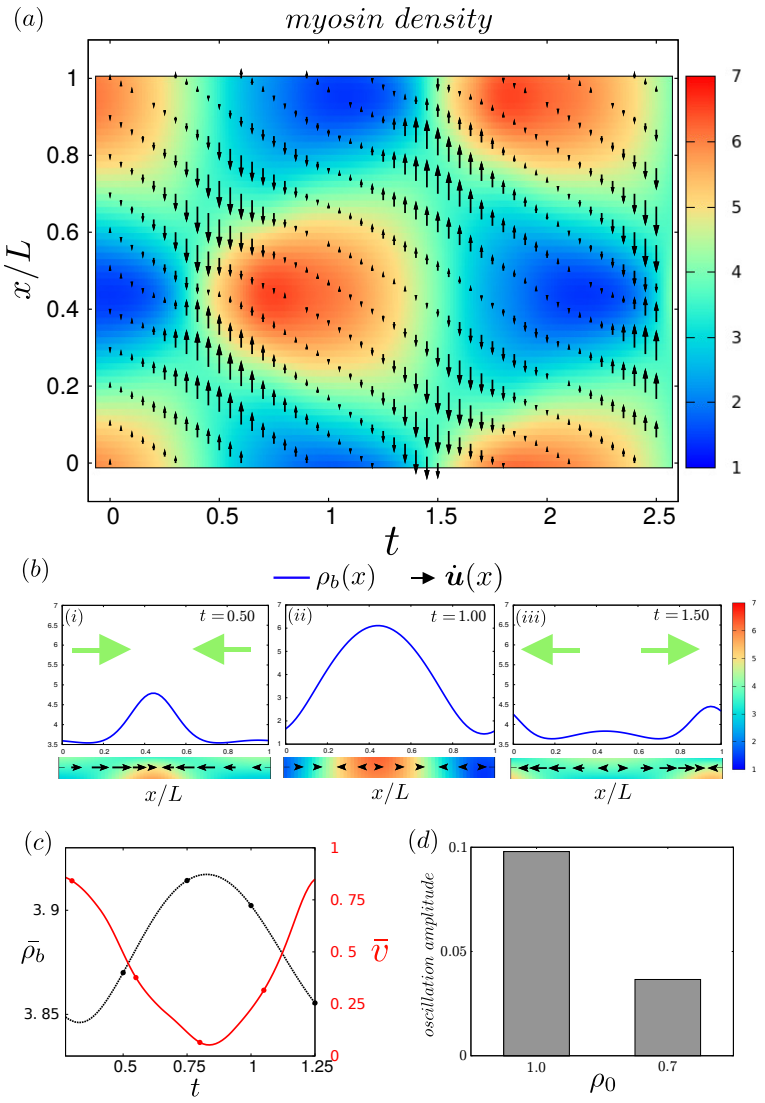

Figure 5.2. We compare the characteristics of the oscillatory phase with the pulsation seen in experiments on germband cells as reported in [11] (specifically Fig. 4 of [11]). (a)-(c) shows that *advection* is crucial to obtain oscillations of bound myosin. (a) Space-time plot (kymograph) of the bound myosin density (colour bar) against a foreground of arrows indicating the local velocity vector $\dot{\boldsymbol{u}}$ (whose magnitude is given by the size of the arrows). This velocity vector describes the advection of myosin by the actin mesh, and shows that local convergence of velocity is associated with increased myosin density (and vice versa). This recapitulates the advection-myosin density profiles shown in Fig. 4a of [11]. (b) This panel shows spatial profiles extracted from the above figure at three specific time instants. There is a definite correlation between convergent velocity vectors (black arrows) and increased myosin density (blue graph) between $t = 0.5$ and $t = 1$, and divergent velocity vectors (black arrows) and reduced myosin density (blue graph) between $t = 1$ and $t = 1.5$. Green arrows show overall convergence (divergence) of advection. Our results here are consistent with Fig. 4a-c of [11]. (c) Time variation of spatially averaged myosin density $\bar{\rho}_b$ (black line) and advection speed $\bar{v}$ (obtained from magnitude of $\dot{\boldsymbol{u}}$, red line) during an oscillation cycle. The graph of $\bar{v}$ is shifted to the left with respect to the myosin density graph by an amount 0.2, indicating that the advection is a cause for local enhancement of myosin density. Our results are entirely consistent with Fig. 4m of [11]. (d) The amplitude of the oscillation decreases when we reduce actin mesh density ρ_0, here we compare $\rho_0 = 1$ with $\rho_0 = 0.7$. Compare this to the actin perturbation experiments, Fig. 4f of [11]. Parameter used here are, $B = 8$, $-\zeta_1 \Delta\mu = 5.2$, $k = 0.2$, $D = 0.25$, $\alpha = 3$, $c = 0.1$.

Now the nucleation, growth and coalescence events of the myosin-dense clusters, precursors to the eventual moving phase of the affine theory, also take place over these time scales - and compare well with the in-vivo kymographs (Fig. 4.7). The establishment of the asymmetric profile of the myosin-dense cluster at the onset of movement also appears to be present in the early time dynamics of the moving myosin profiles observed in-vivo, Fig. 4.8d-f.

The moving (traveling front) solution is the one significant prediction of the full nonlinear affine theory, and appears at later times. By this stage the local contractile stresses are high, opening up the possibility of a crossover to the nonaffine regime. Both the affine and nonaffine theories predict movement - the affine theory predicts a moving deformation or a traveling front, while the movement in the nonaffine theory is associated with mass flow as a consequence of the steady turnover of actin filaments.

To test which of these pictures is true in-vivo, we appeal to FRAP experiments performed on a small region within the actomyosin-dense cluster [12]. These preliminary experiments show loss of recovery upon FRAP, suggesting the possibility of actual mass flow, consistent with the predictions of the nonaffine theory (see Supplementary Information in [12]).

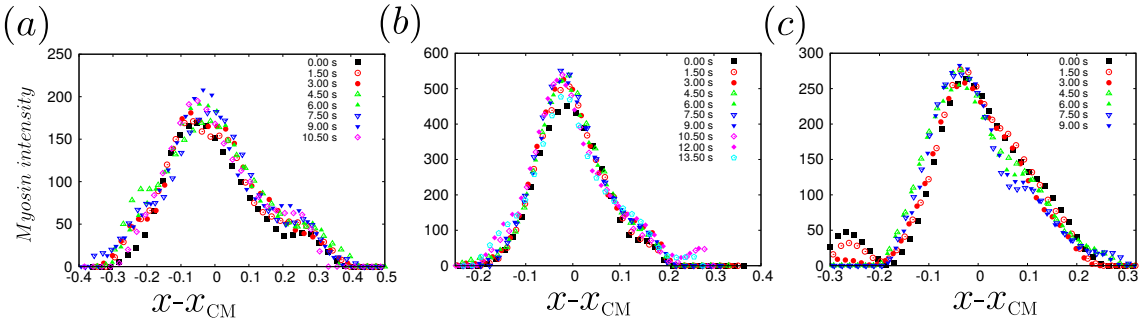

Figure 5.3. Spatial profile and movement of myosin dense regions : Excess bound myosin density in the moving frame. (a-c) Three separate examples of the spatial profile of myosin intensity in the co-moving frame of the flowing actomyosin-dense cluster displayed at different times. Note that the actomyosin-dense cluster hardly changes its shape as it flows towards a junction.

The fact that the actomyosin-dense region commences to move with a constant velocity when it has attained an asymmetric profile, is common to both the affine and nonaffine theory. It moves with a constant velocity in the direction where the

leading edge has the smoother slope and maintains its asymmetric shape as it moves. This appears to be consistent with the situation in-vivo, Fig. 5.3a-c.

The driving force for this movement is established within the medial actomyosin-dense cluster and not the cell boundary. Its propulsion is therefore independent of the boundary or the distance from the boundary. We ask whether this is true of the moving actomyosin-dense regions in-vivo. Figure 5.4a shows that irrespective of its initial position at the commencement of the flow, the moving actomyosin-dense region travels to the left or right cell boundary with equal probability. Further, Fig. 5.4b shows that the moving actomyosin-dense region travels with a constant velocity as it moves towards a given cell boundary, its speed does not depend on the distance from the cell boundary.

From the myosin intensity, we compute the shape-asymmetry via the skewness, $S \equiv \frac{\int_\Omega (x-x_{CM})^3 \rho_b(x)}{\left(\int_\Omega (x-x_{CM})^2 \rho_b(x)\right)^{3/2}}$, of the myosin profile, and find that it is proportional to the speed of the moving myosin-dense cluster (Fig. 5.4c). To our mind, this establishes unambiguously that the flow towards the junctions is spontaneous with the driving force coming from the gradient in myosin established within the front. The boundary does not affect the flow speed, at best, weak asymmetries that may arise at the boundary (for instance due to an asymmetry in functional cadherin) may bias the direction of the flow [84]. One consequence of this is that a cluster moving to the right, might reverse its direction following a coalescence with another moving cluster; such reversals are observed in in-vivo experiments (see Fig.5.5).

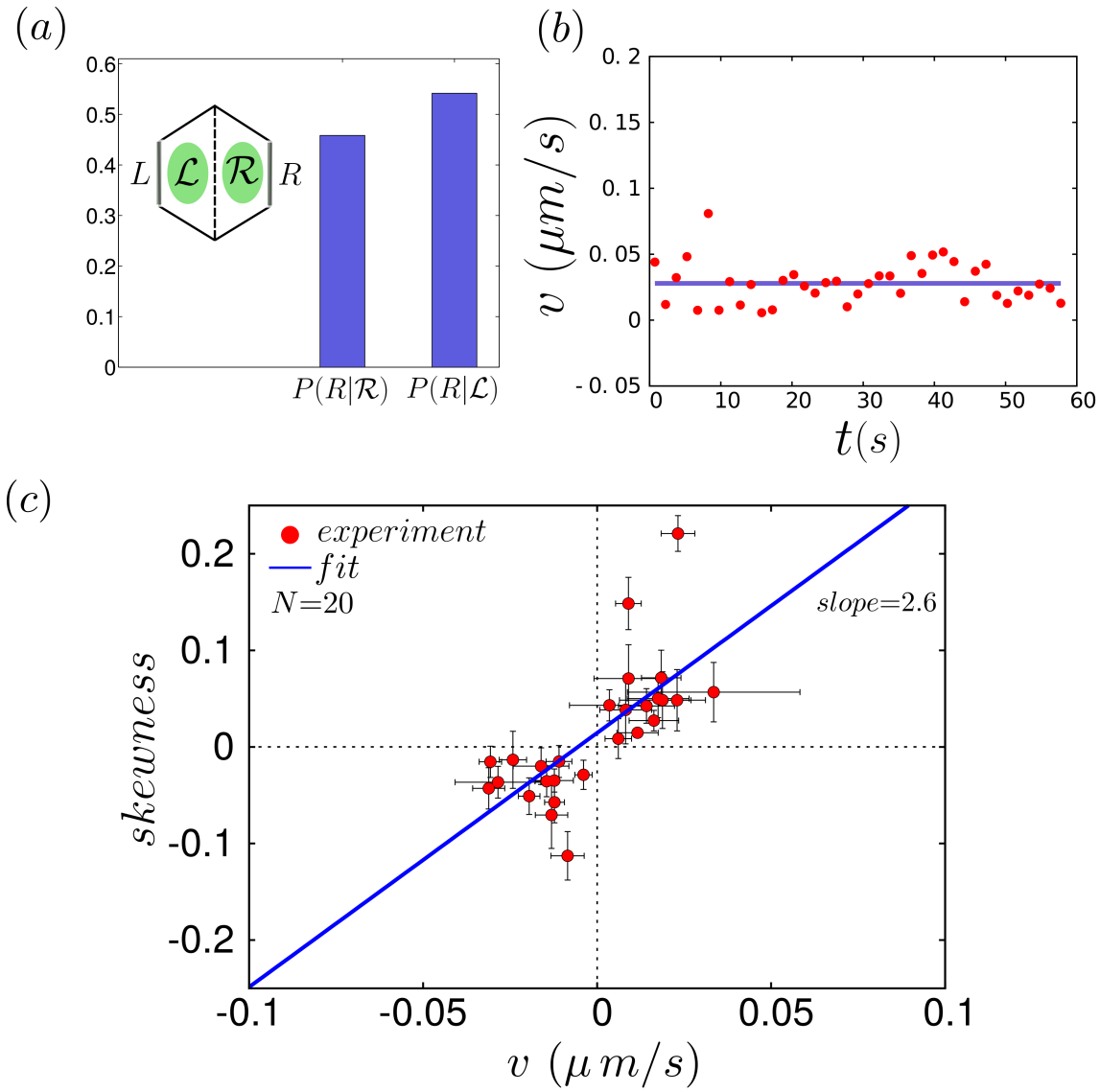

Figure 5.4. Velocity and profile of myosin dense regions : (a) Histogram of the number of flows that move to the right junction R starting from either the right $\mathcal{R}$ ($P(R|\mathcal{R})$ or the left $\mathcal{L}$ ($P(R|\mathcal{L})$ region of the cell (inset shows schematic). Data collected from 24 actomyosin-dense clusters over 18 cells. The fact that the histograms are similar is consistent with the theoretical prediction that the flow is spontaneous and not driven by the cell boundaries. (b) Velocity of an isolated flowing actomyosin-dense cluster monitored over time shows that it is a constant, as predicted by theory. (c) Here we present average skewness values of 28 different pulses plotted against average velocities of the respective pulses. The linear behaviour is quite clear from the data and a linear fit produced a slope value of 2.6 ± 0.5. This intensity data set was prepared from 20 myosin-mCherry tagged germband cells (N=20). Error bars indicate s.e.m. of fluctuation of skewness and velocity values of a pulse in time.

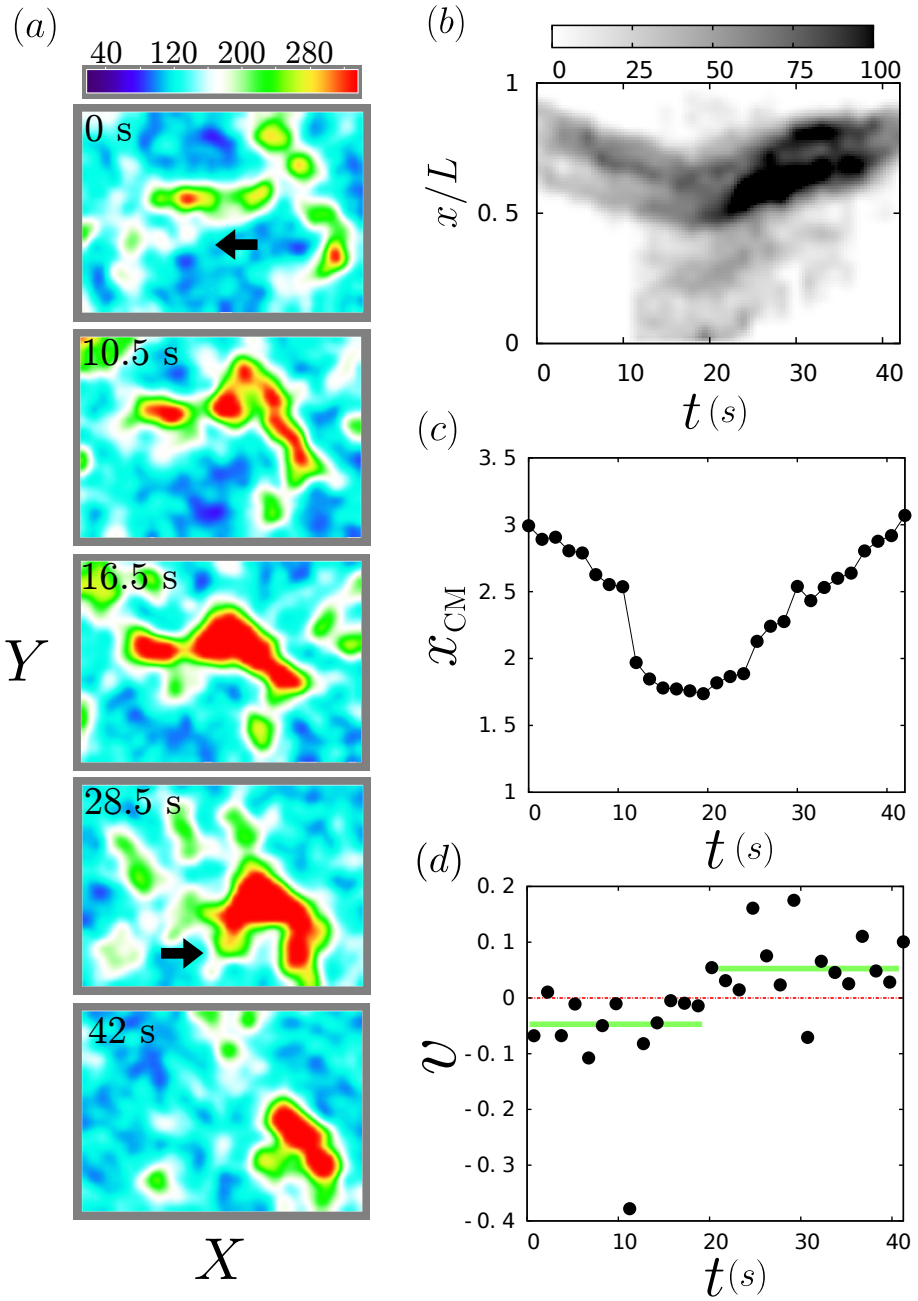

Figure 5.5. Direction reversals of the moving myosin-dense cluster indicate that the driving force for flow does not come from the boundary but is intrinsic to the myosin-dense regions. (a) The 2d intensity maps at different time instants, shows a myosin-dense cluster moving towards the right, which following coalescence, then reverses its direction (movement is along the direction of arrow). (b) Corresponding kymograph clearly shows this velocity reversal. From the projected intensity maps, we quantify the velocity reversals by (c) the center of mass of the myosin-dense cluster x_{CM} versus time and (d) the moving cluster velocity versus time. There is some reorganisation of the myosin-dense cluster upon coalescence.

5.5 Physical values of rescaled parameters

Here we relate the values of the dimensionless parameters to real units extracted from a variety of experimental measurements. For the unit of length, $l = \sqrt{\eta/\Gamma}$ or the actin mesh size, we take 0.5μm (consistent with the rough estimates in [12]) The unit of time, k_b^{-1}, can be estimated from the myosin FRAP data [11] - we find $k_u = 0.2 \pm 0.08\,\mathrm{s}^{-1}$, and taking the ratio $k = k_u/k_b$ to be 1.0, we obtain a binding rate, $k_b = 0.2\,\mathrm{s}^{-1}$. The viscosity of the mesh is taken to be 50 Pa.s [74].

We can now convert all the dimensionless values into real values, and check for consistency with other experimental estimates. Thus, a dimensionless value of the bulk modulus $B = 5$ translates to $B = 42\,\mathrm{Pa}$ (consistent with what can be estimated from [76]). Similarly, a dimensionless value of the magnitude of the active stress, $|\zeta_1 \Delta\mu| = 5$ translates to $|\zeta_1 \Delta\mu \rho_{b0}| = 42\,\mathrm{Pa}$ (roughly the order of magnitude estimated from [76]). Finally, the dimensionless diffusion coefficient $D = 0.25$ implies a real value of $D = 0.01\mu\mathrm{m}^2/s$.

This implies that a dimensionless front velocity $v = 1$ (see, Fig. 5.4c) translates to a real velocity of $v = 0.08\mu$m/s (consistent with the flow velocity of actomyosin reported in [12], also see *Supplementary Fig.8*). Likewise, the time period of oscillation obtained in the section on 'Leading order nonlinearities', $T = 2\pi\left(\eta/k_{u0}(B + \zeta_1 \Delta\mu\rho_{b0})\right)^{1/2}$ translates to be $\sim 20s$ and the active propulsion force f_{act} is estimated at $30 - 60pN$ (consistent with [76]).

5.6 Concluding remarks and future directions

Although simplified, in that it has completely ignored the coupling of actomyosin dynamics to local chemical signalling such as Rho [11], we believe this active elastomer model with strain-dependent turnover of components, admitting both affine and nonaffine deformations, captures the essential physics of actomyosin pulsation and flows observed in a wide variety of tissue remodeling contexts such as *Drosophila* germband extension and dorsal closure in the amnioserosa. The minimal ingredients for actomyosin pulsation and flow are mesh-elasticity, actomyosin contractility, advection and turnover of both myosin and actin.

In this study, we have modelled the medial actin mesh during apical constriction

and germband extension in the *Drosophila* embryo as an active elastomer embedded in a solvent [84, 43, 35, 44], which undergoes turnover of all its components. Our description goes from the hydrodynamics of an affine elastomer to a nonaffine elastomer, the latter incorporating network rupture and remodeling, resulting in intranetwork flows. It thus goes from an elastomer to a fluid-like description. Together, the affine and nonaffine active elastomer model captures the range of dynamical regimes exhibited in this system.

To make a detailed comparison of the spatiotemporal actomyosin patterns with experiments generated using quantitative imaging, we will need to extend this numerical study to 2-dimensions, using appropriate (anisotropic) boundary conditions and allowing for shear. The nucleation and growth of the actomyosin-rich domains are similar to that seen in 1-dim, with the difference being that domains can move around each other in 2-dim and can exhibit anisotropic movement.

In future, we would like to extend this framework to understand the dynamical coupling of the medial actomyosin with degrees of freedom (concentration of E-cadherin) attached to a deformable cell junction. Though the emergence of actomyosin flows does not depend on specific boundary conditions, cell boundaries may directionally bias the intrinsic ability of actomyosin networks to generate flow, as proposed before [84].

End of Chapter

Chapter 6

Dynamics of junction shrinkage

6.1 Introduction

A central problem in tissue morphogenesis is to understand how the noisy dynamics of local molecular force generators ultimately results in reliable and robust shape changes at the cellular and tissue scale. A striking example is the myosin driven cell shape changes in developing tissues across organisms. For instance, tissue extension in the *Drosophila* embryo proceeds by the intercalation of cells, which is initiated by the active step-wise shrinkage of the vertical cell junctions (Fig. 6.1(a)). This junctional shrinkage is driven by the enrichment of myosin at this junction and resisted by the trans-clusters of the cell adhesion proteins, E-cadherin [83, 12]. The noisy step-wise shrinkage of junction length observed in experiments suggests a ratchet-like driving mechanism (Fig. 6.1(b)).

In this chapter we *derive* a precise dynamical model for the ratchet based on basic phenomenology of myosin and cadherin at the junction. More significantly, we identify a novel molecular mechanism, based on two pools of myosin working in tandem, that provide a robust and reliable ratchet.

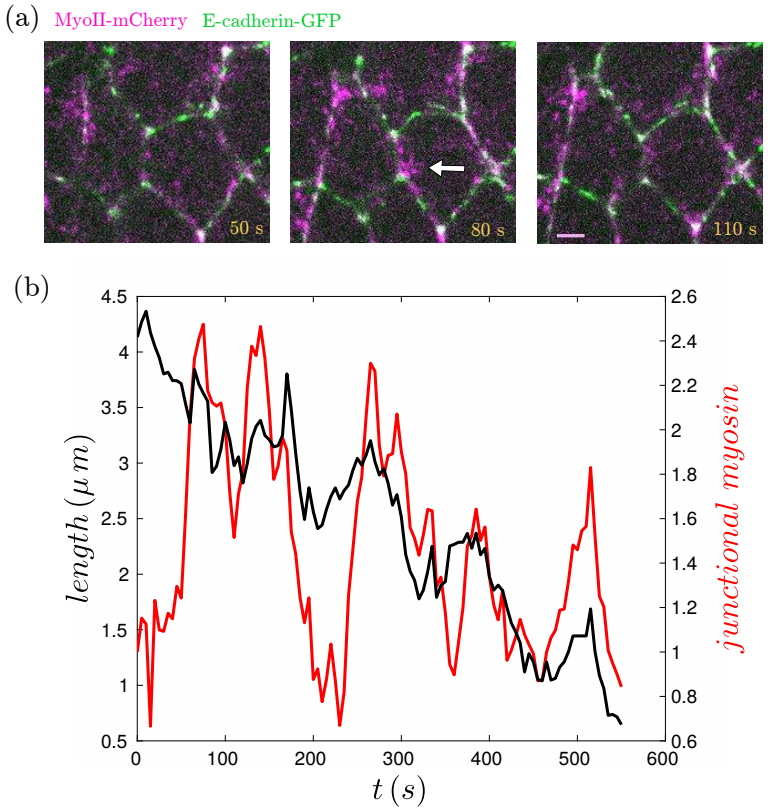

Figure 6.1. Junction shrinkage from actomyosin pulsation and flow : (a) Pulsation and subsequent flow of myosin (in magenta) dense regions towards vertical junctions (in green) shrinks the junction in stepwise manner. The white arrow marks a convergence of actomyosin dense region with the junction, following the convergence the dense region decay. (b) Measurement of total junctional myosin intensity (renormalized by the initial intensity) and length of the above shown junction throughout shrinkage of the whole junction shows that shrinkage happens in a stepwise manner upon convergence of myosin pulse with the junction. The total junctional myosin intensity was normalized by the initial intensity value.

6.2 Theoretical description of a junction

Here we develop a theoretical description of the cell junction to understand the junctional remodeling dynamics during junction shrinkage in terms of the following dynamical variables - the length of the junction $L(t)$, total amount of myosin at junction $\rho_m(t)$ and total amount of E-cadherin cluster $\rho_c(t)$ and monomer $\rho_1(t)$ at the junction. The dynamics of a junction in terms of these dynamical variables is a result of the spatial and temporal evolution of local quantities. Thus to arrive

at the dynamical description we identify the important local quantities and derive the dynamical equations from the local dynamics by integrating over the spatial degrees of freedom. We begin with the description of the junction in the plane of the tissue (*thick junction*) then arrive at a reduced description of an interface in the plane (*thin junction*). Then we finally derive the resulting dynamical system from the thin junction description. We elaborate on these steps below.

To elucidate the thick junction description we first consider the apical actomyosin layer of the germband cell which is anchored to the E-cadherin molecules in the cell membrane. The E-cadherin molecules play major role in cell adhesion and inter-cellular force transduction via forming *trans*-homophilic clusters with cadherin molecules from the neighbouring cells in the adjacent membrane (see Fig.6.2a) [86]. They also form *cis*-homophilic clusters with the same-membrane cadherin molecules (see Fig.6.2a) [86]. The dynamics of E-cadherin clusters are modulated by its interactions with actomyosin mesh [90] via linker proteins (see Fig.6.2a) such as α-Catenin, vinculin which physically link the cadherin adhesive complexes to actomyosin network [91].

The the actomyosin network near the cell membrane of both the cells connected via trans-clusters provide the structural rigidity to the cell junction and this inter-cellular structure is important in determining the mechanical properties of the cell junction. This connected structure spanning the region near cell membrane of both the cells is referred as thick junction here (Fig.6.2a). The part of actomyosin network away from the junction (medial, see Fig.6.2a) is transiently connected to the thick junction and exert contractile forces on the junction. Material transfer takes place between junctional and medial actomyosin in germband cells via actomyosin flow [12].

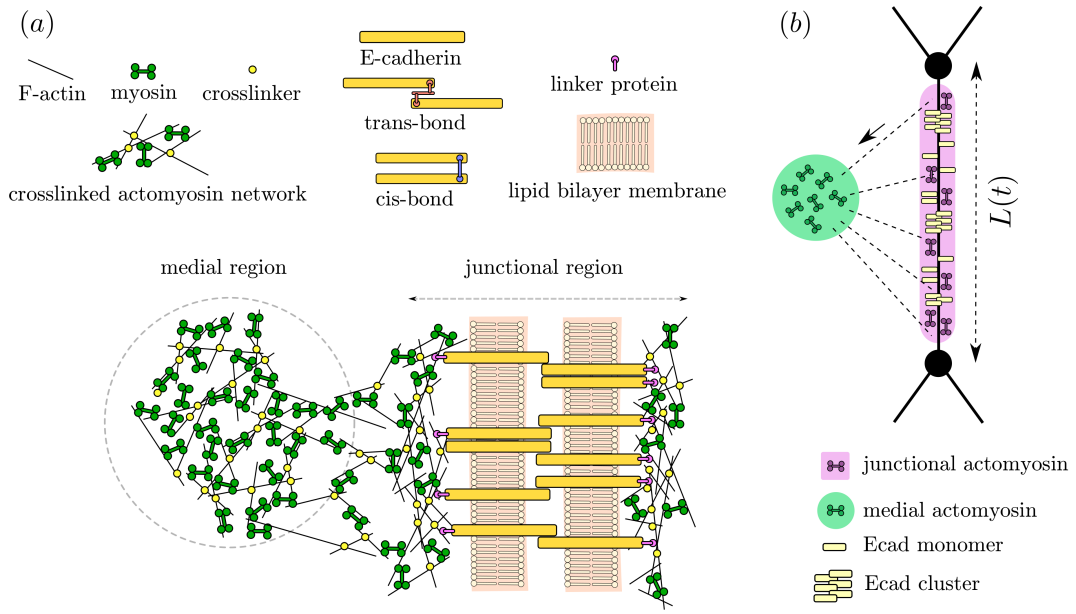

Figure 6.2. (a) The thick junction is the two dimensional description of cell junction formed by inter-cellular actomyosin network connected via cadherin trans-clusters which anchor to the actomyosin via linker proteins. (b) The one dimensional thin junction description

Now integrating on the thick junction structure along the thickness lead us to a one dimensional description of actomyosin mesh described by displacement field $u(x,t)$ and bound myosin density $\rho(x,t)$ and similarly cadherin can be described by monomer and trans-cluster density profile along the length ($\rho_1'(x,t)$ and $\rho_c'(x,t)$ respectively). Now we can use the previously developed hydrodynamic description for actomyosin network [73] to describe this thin junction (Fig.6.2b). The overdamped Rouse dynamics of the actomyosin network is described by force balance given by

$$\Gamma(\partial_t u - v) = \partial_x \sigma(x,t), \tag{6.1}$$

dynamics of the myosin density (ρ) given by

$$\partial_t \rho + \partial_x J = k_b - k_u \rho + P(x,t) \tag{6.2}$$

and dynamics of cadherin trans-cluster(ρ_c') and monomer (ρ_1') as

$$\begin{aligned}\partial_t \rho_c' + \partial_x J_c &= -\frac{\rho_c'}{\tau_f} + \frac{\rho_1'}{\tau_a} + s_c(x,t) \\ \partial_t \rho_1' + \partial_x J_1 &= -\frac{\rho_1'}{\tau_a} + \frac{\rho_c'}{\tau_f} + s_1(x,t)\,. \end{aligned} \tag{6.3}$$

Here v is the velocity of fluid in the lipid bilayer, the total internal stress σ is the sum of elastic, dissipative and active stresses, $\sigma = \sigma^e + \sigma^d + \sigma^a$ and Γ is the friction resulting from relative motion of the actomyosin network with respect to the cytosol and the movements of cadherin molecules in lipid bilayer membrane. The myosin flux along the junction, given by J, arises from advection and diffusion along the length of the junction. The turnover of myosin occurs with binding and unbinding rates given by k_b and k_u respectively. In the myosin dynamics (Eq.6.2) $P(x,t)$ acts as a source term representing inflow of myosin into the junction from the medial region as a result of actomyosin flow towards vertical junctions. The cadherin monomer and trans-cluster density dynamics is dictated by respective currents (J_1, J_c) and a aggregation-fragmentation dynamics where monomers aggregate to form cluster in a timescale τ_a and clusters break into monomers in a timescale τ_f. The source terms s_1 and s_c in cadherin dynamics can originate from the processes such as endocytosis, recruitment and flow of cadherin. For details of the derivation please refer to the additional calculations (Appendix.A.5).

6.3 Dynamical equations for junction

Now we can derive the dynamical equations from the thin junction description by integrating the equations (Eq.6.1-6.3) along the length of the interface.

Junction length dynamics follows from force-balance applied to an elastomer subject to active stresses

$$\dot{L} = -\frac{1}{\tau_L}\left(L - L_0\right) + F^a \tag{6.4}$$

where the junction length relaxes in a timescale τ_L which depends on stiffness and viscosity of the elastomer (thus in principle it can depend on ρ_m and ρ_c), the junction

rest length L_0 depends on ρ_c, and the active contractile force F^a depends on the junctional myosin ρ_m.

Junctional myosin undergoes turnover at the junction and get replenished by the periodic pulsation

$$\dot{\rho}_m = -\frac{1}{\tau_m}(\rho_m - \rho_{m0}) + \Delta_J \tag{6.5}$$

where the time dependent influx to the junction or the *junctional pulse*, arising from the flow of medial myosin, is defined as Δ_J and ρ_{m0} is the steady state distribution of junctional myosin in the absence of the medial myosin flow and is set by the binding-unbinding rates of myosin at the junction.

Cadherin trans-cluster and monomer undergoes turnover and fragmentation-aggregation

$$\dot{\rho}_1 = -\frac{\rho_1 - \rho_{10}}{\tau_c} + S_1 \tag{6.6}$$

$$\dot{\rho}_c = -\frac{\rho_c - \rho_{c0}}{\tau_c} + S_c \tag{6.7}$$

with rates (τ_a, τ_f) that depend on the density of junctional myosin and the turnover of cadherin via flows from the boundary or endocytosis is described by S_1 and S_c. It is important to note that in the aggregation-fragmentation dynamics there is actually a single timescale that determine the relaxation to steady state of cadherin cluster and monomer (ρ_{c0}, ρ_{10}). This relaxation time for cadherin dynamics is given by $\tau_c = \frac{\tau_a \tau_f}{\tau_f + \tau_a}$. Here $\rho_{10} = \left(\frac{\tau_c}{\tau_f}\right) n$ and $\rho_{c0} = \left(\frac{\tau_c}{\tau_a}\right) n$, where we set total amount of cadherin $n(t) = \rho_1(t) + \rho_c(t)$ at any point of time. For details of the derivation please refer to the additional calculations (Appendix.A.5).

6.3.1 Constitutive formulae: dependence of phenomenological parameters on myosin and cadherin

Now we define the constitutive relations for junction rest length (Fig.6.3 a) and active force (Fig.6.3 b) derived from phenomenology. Active force is given by

$$F^a(\rho_m) = \zeta_1 \Delta\mu \left(\frac{\rho_m}{1 + \zeta_2 \rho_m}\right) \tag{6.8}$$

and the rest length is given by

$$L_0(\rho_c) = L^* + \beta_1 \left(\frac{\rho_c^\theta}{1 + \rho_c^\theta} \right) . \tag{6.9}$$

Here $\Delta\mu$ is the difference in the chemical potential of ATP and its hydrolysis products, $\zeta_1 < 0$ for contractile active stress and ζ_2 is positive. The rest length has a cadherin independent residual part L^* and the cadherin trans cluster dependent part has two parameters, a length contribution factor β_1 and a dimensionless positive constant θ that controls the cadherin dependence of L_0 at low values of cadherin cluster amount.

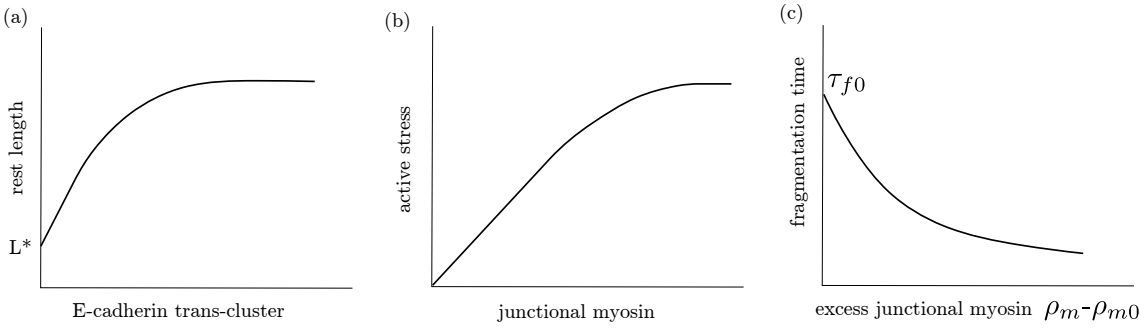

Figure 6.3. Phenomenological dependence of (a) junction rest length, (b) active stress and (c) fragmentaion time on myosin/cadherin.

The junctional pulse signal $\Delta_J(t)$ is defined by four parameters namely the amplitude of the pulse (A), duration of the pulse (τ_p), waiting time between two pulses (τ_w) and noise in the signal (δ) (see, Fig. 6.4a) as

$$\Delta_J(t) = A \sum_{i=1}^{n_p} \left(H(t - t_i) - H(t - (t_i + \tau_p)) + \delta(t) \right. . \tag{6.10}$$

Here $H(t)$ is an *Heaviside step function* defined as $H(x) = \frac{d}{dx} max\{x, 0\}$ and $t_i = t_0 + (i-1)(\tau_p + \tau_w)$ where the pulses start from $t = t_0$ and n_p is the number of actomyosin flow event (a single pulse) that the signal contains (see, Fig. 6.4a).

The aggregation-fragmentation dynamics is dictated by the timescales τ_a and τ_f and as we have already mentioned the cadherin dynamics is modulated by contractile forces from actomyosin dynamics. So these timescales can be written as a function

of medial and junctional myosin. Here we specifically consider the effect of the junctional myosin pool on the cadherin aggregation-fragmentation dynamics. We consider a enhanced de-clustering of cadherin trans-clusters upon increasing active force in the junction (Fig.6.3 c) and this is incorporated as active force dependent fragmentation time given by

$$\tau_f = \tau_{f0} e^{\gamma_1 (F^a - F_0^a)} \,. \tag{6.11}$$

Here γ_1 is a negative constant that represents the strength of active force dependence of fragmentation time, τ_{f0} is the force independent fragmentation time and $F_0^a = F^a(\rho_{m0})$. So γ_1 being negative, excess active forces will reduce τ_f resulting in enhanced fragmentation of cadherin clusters.

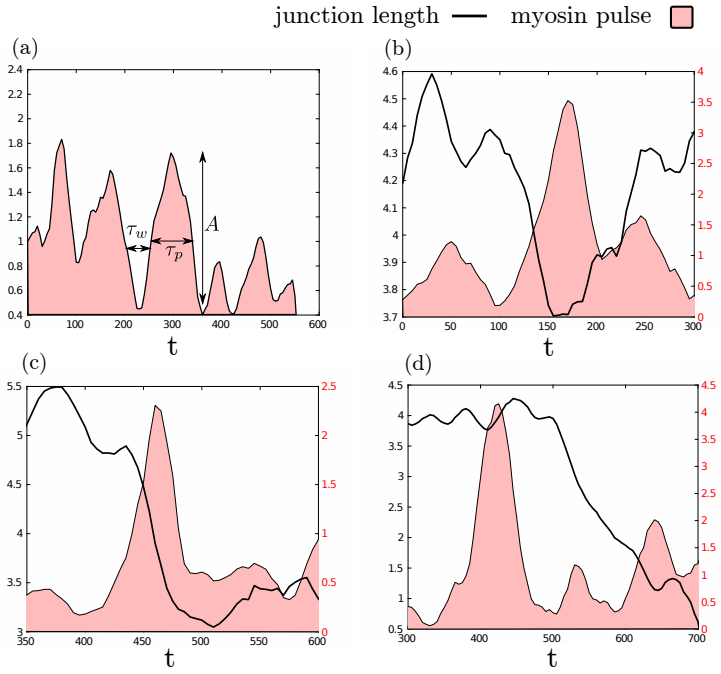

Figure 6.4. Dynamic phases of junction shrinkage dynamics from experiments: (a) A typical junctional myosin pulse signal (in myosin intensity as $\frac{I(t)}{<I>}$) containing multiple pulses. The pulse amplitude A, pulse duration τ_p and waiting time between two pulses τ_w are marked for one of the pulses. Dynamical phases of junction shrinkage in terms of junction length (in μm) and myosin pulse intensity (in $\frac{I(t)}{<I>}$) show example of (b) reversible, (c) reliable stepwise shrinkage and (d) junction collapse.

6.3.2 Steady state of the junction

We consider the junction to be in steady state given by $(L = L^s, \rho_m = \rho_m^s, \rho_c = \rho_c^s)$ in absence of any myosin pulses ($\Delta_J = 0$) with no cadherin turnover ($\dot{n} = 0$). Note that the constraint of total cadherin conservation allows us to reduce the cadherin dynamics to only cadherin cluster (ρ_c) dynamics. Thus the steady state of the junction is given by

$$\begin{aligned} \rho_m^s &= \rho_{m0} \\ \rho_c^s &= \left(\frac{\tau_c}{\tau_a}\right) n \\ L^s &= L^* + \beta_1 \left(\frac{(\rho_c^s)^\theta}{1+(\rho_c^s)^\theta}\right) + \tau_L \zeta_1 \Delta\mu \left(\frac{\rho_m^s}{1+\zeta_2 \rho_m^s}\right). \end{aligned} \tag{6.12}$$

6.3.3 Classification of dynamical phases

In our analysis we encounter three distinct dynamical phases in response to forces exerted by myosin pulses which we describe below. Here we describe the shrinkage of the junction in terms of its steady state length in response to a junctional myosin pulse which is "ON" ($\Delta_J \neq 0$) during $t_1 \leqslant t \leqslant t_2$. We can define three possible cases (see, Fig. 6.4 b-d) in terms of deformations of the junction length to be

- Unreliable shrinkage (reversible) : junction shrinks in response of pulse but when the applied pulse is removed it relaxes back to steady state length(L^s). So away from the pulse the junction is always at same length L^s.
- Reliable stepwise shrinkage (irreversible) : junction shrinks in response of pulse but when the applied pulse is removed it does not relax back to steady state length (L^s) but to a reduced steady state length and remain in this reduced length unless perturbed again. So $L^s(t > t_2) < L^s(t < t_1)$.
- Junction collapse : junction shrinks in response of a pulse (while $t \leqslant t_2$) to a length $L^s \to 0$.

6.4 Junction shrinkage with fixed cadherin level : Unreliable shrinkage

Here we explore the junction shrinkage using the description given by the equations Eq.6.4-6.7 with constitutive relations described in Eq.6.9-6.11. The imposed constraint of fixed cadherin level or the absence of cadherin turnover can be described by the condition $\dot{n} = 0$. Let us rewrite the dynamical equations for this particular case.

Using the condition $\dot{n} = 0$ we can describe the dynamics of cadherin by only ρ_c (or ρ_1). It is also clear that the said condition imply $S_1 + S_c = 0$. The resulting dynamical equations will be given by

$$\begin{aligned} \dot{L} &= -\frac{L - L_0}{\tau_L} + F^a \,, \\ \dot{\rho}_m &= -\frac{1}{\tau_m}\left(\rho_m - \rho_{m0}\right) + \Delta_J(t) \,, \\ \dot{\rho}_c &= -\frac{1}{\tau_c}\left(\rho_c - \rho_{c0}\right) \end{aligned} \tag{6.13}$$

In the following subsection(s) we treat this resulting system analytically (with few simplifications for analytical tractability) and compare the results with numerical solutions. The results bring out interesting effect of conserved cadherin dynamics in junction shrinkage.

6.4.1 No reliable stepwise shrinkage in junction with fixed cadherin level

We study the system analytically for a single pulse ($n_p = 1$) and for a pulse train ($n_p > 1$). A single isolated pulse always produce either a reversible shrinkage or a junction collapse in absence of cadherin turnover. This result is intuitive because without any change in total cadherin the single pulse can only impart transient effect (no effect of the pulse remain in L, ρ_m and ρ_c at a time $t > \tau_m$, τ_c, τ_L) on the junction length. Thus if the junction length becomes very small $L \to 0$ within

the duration of the pulse we get a junction collapse but all other cases result in reversible or unreliable shrinkage.

When the junctional pulse signal (Δ_J) consists of many pulses we get *stepwise looking* shrinkage in a limit where the relaxation of myosin, cadherin or length is much slower compared to the pulse waiting time i.e., $\tau_w < \tau_m$, τ_c, τ_L. In this limit the stepwise nature of junction shrinkage emerges from a collective effect of pulses where the junction cannot relax back to the steady state as the pulsation is faster than the timescale of relaxation. Thus the observed stepwise shrinkage is referred as *unreliable stepwise shrinkage* where the stepwise shrinkage disappears and the junction returns to its initial length once the pulse train is removed ($\Delta_J = 0$) (see Fig.6.5c).

We present the phase diagram predicted from the analytic study (see Fig.6.5a) and the phase diagram from numerical solutions (see Fig.6.5b). The analytic phase diagram calculated from a simplified system roughly matches with the numerical study of the system (Eq.6.13). The analytic phase boundaries between reversible and unreliable stepwise shrinkage is given by the condition

$$\begin{aligned} L^* + \tau_L\zeta_1\Delta\mu(\rho_{m0} + A\tau_m(1-\chi^p)) \\ +\beta_1(1-e^{-\frac{\tau_p}{\tau_c}})\left(\frac{e^{\gamma_1\zeta_1\Delta\mu A\tau_m(1-\chi^p)}}{1+e^{\gamma_1\zeta_1\Delta\mu A\tau_m(1-\chi^p)}}\right)n \\ +\beta_1\left(\frac{e^{-\frac{\tau_p}{\tau_c}}}{2}\right)n &= 0 \end{aligned} \tag{6.14}$$

and the analytic phase boundaries between unreliable stepwise shrinkage and junction collapse is given by the following condition

$$L^* + \tau_L\zeta_1\Delta\mu(\rho_{m0} + A\tau_m\phi^H) + \beta_1\left(\frac{e^{\gamma_1\zeta_1\Delta\mu A\tau_m\phi^H}}{1+e^{\gamma_1\zeta_1\Delta\mu A\tau_m\phi^H}}\right)n = 0\,. \tag{6.15}$$

Here $\phi^H = 1 - \left(\frac{1-\chi^p}{1-\chi^p\chi^w} + \chi^p\right)\chi^p$, $\chi^p = e^{\frac{-\tau_p}{\tau_m}}$ and $\chi^w = e^{\frac{-\tau_w}{\tau_m}}$. See Appendix.A.6 for details.

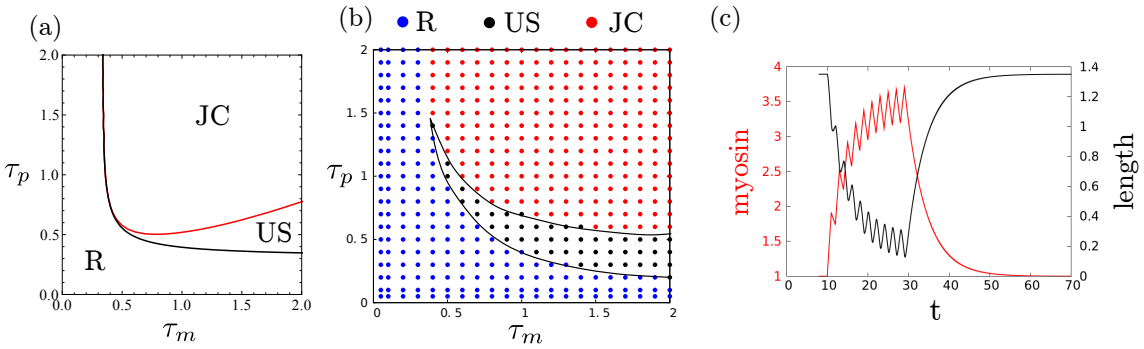

Figure 6.5. Fixed cadherin level produces unreliable shrinkage : Phase diagram in myosin relaxation time (τ_m) and pulse duration (τ_p) from (a) approximate analytical solution and (b) numerical solution shows the reversible or unreliable junction shrinkage (R), unreliable stepwise shrinkage (US) and junction collapse (JC). Here we take $\zeta_2 = 0$, $\theta = 1$ and the other parameter values used for both the phase diagrams are given below (Table.6.1). (c) An instance of unreliable stepwise junction shrinkage from numerical solution of Eq.6.13.

Table 6.1. Parameter values

$\gamma_1 = 1$	$n_p = 10$	$-\zeta_1 \Delta\mu = 1$	$A = 2$	$\tau_w = 1$
$\tau_L = 0.5$	$\beta_1 = 0.1$	$\rho_{m0} = 1$	$L^* = 0.1$	$\tau = 0.1$

These results leads to the conclusion that in the fixed cadherin level model we only achieve unreliable shrinkage and junction collapse but no true case of stepwise junction shrinkage can be achieved. This spells out the importance of cadherin turnover in the junction dynamics. We explore the junction shrinkage with turnover of cadherin in the next section. For details of the analytical solution please refer to the appendix.

6.5 Junction shrinkage with leaky cadherin level : Reliable shrinkage

The study of fixed cadherin level does not show reliable stepwise shrinkage and indicates that cadherin turnover might be important for reliable shrinkage of the cell

junction. Here we use the description given by the equations Eq.6.4-6.7 with constitutive relations described in Eq.6.9-6.11 and propose an active force dependent turnover dynamics for cadherin referred as *leaky cadherin* dynamics here. We consider extraction of cadherin monomers driven by contractile forces from actomyosin flow. This is incorporated here via the source term for cadherin monomer S_1, taken in the following form

$$S_1 = -\beta_2 g_R(\rho_m)\rho_1 \tag{6.16}$$

where g_R is a response function which facilitates cadherin monomer extraction in response of the junctional pulse (Δ_J). This response function takes value as $g_R = 1$ and $g_R = 0$ in presence and absence of the pulse respectively. The proportionality constant β_2 determine the amount of monomer extraction and can in principle depend on local chemical regulation or contractile force exerted by junctional actomyosin. Here g_R is defined in such a way that it requires a threshold active force (F^c) to initiate extraction of cadherin monomers. We define this force as $F^c = F^a(\rho_m = \rho_m^c)$ where ρ_m^c is a parameter of the system. Finally g_R is given by

$$g_R(\rho_m) = \frac{1}{2}\left(1 + tanh(s(\rho_m - \rho_m^c))\right) . \tag{6.17}$$

Here s is a positive constant that controls sensitivity of the response function. The sharpness of the transition of g_R from 0 to 1 increases with increasing s.

It is noteworthy that we do not consider direct turnover of cadherin trans-clusters ($S_c = 0$) as the cadherin trans-clusters are formed by cadherin molecules from opposing cell membranes, it seems unlikely that they can be directly added or removed to/from the membrane without breaking the trans cluster into monomers. But extraction of monomer will result in reduction of the steady state cadherin cluster amount via aggregation-fragmentation dynamics. Now we rewrite the resulting system as

$$\begin{aligned}
\dot{L} &= -\frac{L - L_0}{\tau_L} + F^a \,, \\
\dot{\rho}_m &= -\frac{1}{\tau_m}\left(\rho_m - \rho_{m0}\right) + \Delta_J(t) \,, \\
\dot{\rho}_1 &= -\frac{1}{\tau_c}\left(\rho_1 - \rho_{10}\right) - \beta_2 g_R(\rho_m)\rho_1 \\
\dot{\rho}_c &= -\frac{1}{\tau_c}\left(\rho_c - \rho_{c0}\right) \,. \qquad (6.18)
\end{aligned}$$

With this description now we probe the junction shrinkage dynamics with E-cadherin extraction.

6.5.1 Permanent change in junction length: Effect of a single pulse

Actomyosin pulsation and flow appear periodically and remodel the vertical junction in successive shrinkage steps during germband extension to drive the process of cell intercalation. Thus a proper description of the junctional pulse signal Δ_J should contain multiple pulses. Despite the above fact, we shall first consider a single pulse (Δ_J with $n_p = 1$) to understand its effect on the junction length. We analytically derive the amount of length shrinkage (δL) caused by a single pulse of duration τ_p to be

$$\delta L = \frac{\beta_1 n(0)}{2}\left(e^{-\kappa\tau_p} - 1\right) \,. \qquad (6.19)$$

Here $\kappa = \frac{\beta_2 g_R}{(1+\alpha)(1+\tau_c\beta_2 g_R)}$ with $\alpha = e^{\gamma_1\zeta_1\Delta\mu A\tau_m(1-\chi^p)}$ and $n(0)$ denotes the total amount of cadherin before arrival of the pulse. This change in junction length is a direct result of reduction in steady state cadherin trans-cluster amount (ρ_{c0}) in the junction. This reduction in trans-cluster amount will reduce the rest length of the junction resulting permanent change in junction length i.e., $\delta L > 0$ (see Fig.6.6a). We now present the phase diagram from analytical calculations and compare it with a phase diagram from numerical solution (Fig.6.6b-c) of the system (Eq.6.18). Note that a pulse of low amplitude (A) and duration (τ_p) might not exert enough

contractile force to remodel the junction and the response function g_R remains zero resulting no permanent shrinkage but a transient shrinkage ($\delta L = 0$) of the junction as seen in the reversible phase (Fig.6.6). For details of the analytical treatment See Appendix.A.8.

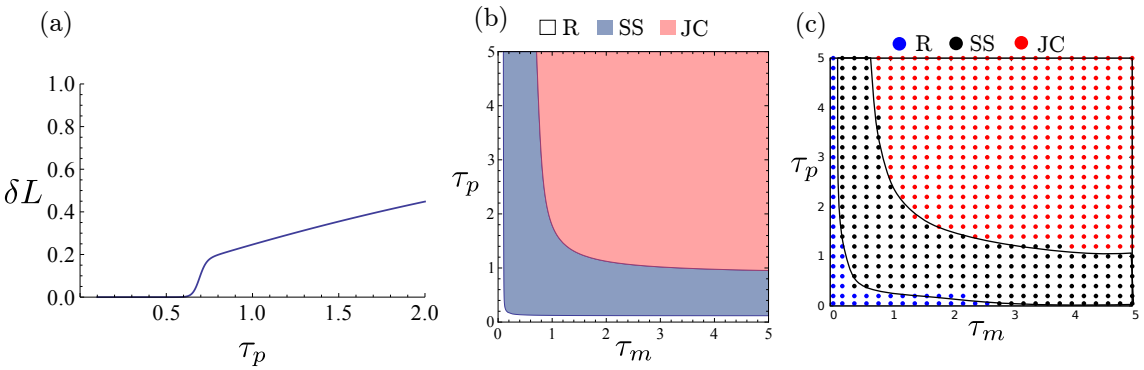

Figure 6.6. Leaky cadherin level produces permanent deformation of junction and reliable shrinkage: (a) Amount of shrinkage δL for a single pulse becomes non-zero then increases as we increase the pulse duration (τ_p). Phase diagram in myosin relaxation time (τ_m) and pulse duration (τ_p) from (b) approximate analytical solution and (c) numerical solution shows the reversible or unreliable junction shrinkage (R), reliable stepwise shrinkage (SS) and junction collapse (JC). Fixed parameters was taken to be $\zeta_2 = 0$, $\theta = 1$, $L^* = 0.5$, $\beta_1 = 0.2$, $\rho_m^c = 1.5$ and $\gamma_1 = 0.1$. All other parameters are given by (Table. 6.2).

Table 6.2. Parameter values

$\beta_2 = 0.1$	$N_0 = 10$	$-\zeta_1 \Delta\mu = 1$	$A = 2$
$\tau_L = 0.5$	$\rho_{m0} = 1$	$s = 50$	$\tau_{a0}, \tau_{f0} = 0.1$

6.5.2 Reliable stepwise shrinkage

We now solve the system (Eq.6.18) for a pulse train ($n_p > 1$) and obtain stepwise shrinkage of the junction (see Fig.6.7 a). Note that the dynamic phase of stepwise shrinkage in this case shows permanent change in junction length. Thus in this description we achieved *reliable stepwise shrinkage* through the active force dependent

cadherin extraction from the junction. This reliable stepwise shrinkage of the junction is remarkably similar to the observed junction length dynamics in experiments (Fig.6.1). We present the numerical phase diagram in terms of reversible, reliable stepwise shrinkage and junction collapse (Fig.6.7b) in force independent cadherin turnover timescale (τ_{c0}) and myosin turnover timescale (τ_m).

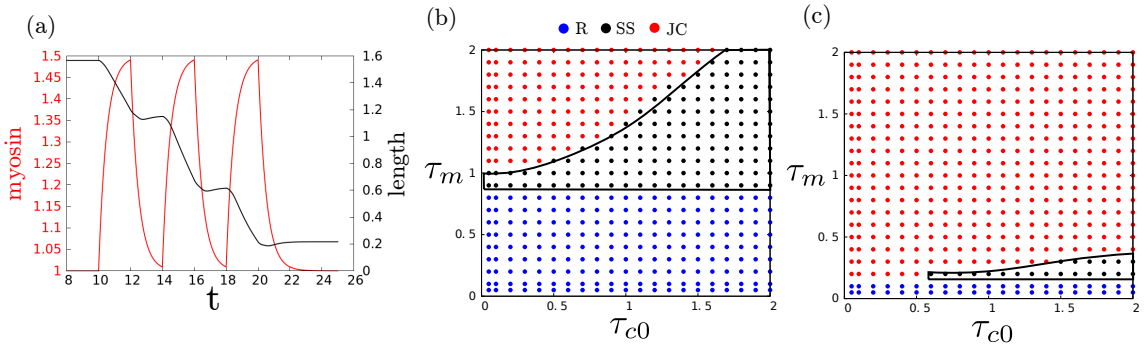

Figure 6.7. Leaky cadherin level produces reliable stepwise shrinkage bus lacks robustness : (a) An instance of reliable stepwise shrinkage. (b-c) Phase diagram in cadherin relaxation time (τ_{c0}) and myosin relaxation time (τ_m) for junction myosin pulse amplitude (b) $A = 1$ and (c) $A = 10$ shows significant loss in stepwise shrinkage phase pointing towards a lack of robustness in the current description of junction shrinkage. Phases are reversible or unreliable junction shrinkage (R), reliable stepwise shrinkage (SS) and junction collapse (JC). Here we take $\zeta_2 = 0$, $\theta = 1$, $\gamma_1 = 0.5$, $\rho_m^c = 2$ and the other parameter values used for both the phase diagrams are given below (Table.6.3).

Table 6.3. Parameter values

$\beta_2 = 5$	$n(0) = 10$	$-\zeta_1 \Delta\mu = 1.5$	$\tau_p, \tau_w = 5$
$\tau_L = 0.2$	$\rho_{m0} = 1$	$s = 50$	$\beta_1 = 10$

The topology of the phase diagram in Fig.6.7 is easy to understand. Increasing myosin turnover timescale (i.e., slow turnover) would increase myosin accumulation in the junction from a junctional pulse thus it would result in production of higher amount of active force in the junction. Thus we see a transition from reversible to stepwise shrinkage to junction collapse with increasing myosin turnover (Fig.6.7b).

Playing an opposite role, increase in cadherin aggregation-fragmentation timescale will stabilize a junction collapse to a stepwise shrinkage (Fig.6.7b) as slower cadherin dynamics will result in reduced extraction of cadherin. The transition from reversible to stepwise shrinkage phase does not depend on the cadherin aggregation-fragmentation but determined by the myosin turnover and the pulse amplitude as active force increase during a pulse goes as $\sim A\tau_m$.

6.5.3 Timescales in junction shrinkage

So far we have not discussed the actual ranges of the various timescales that we use in the theoretical description of junction shrinkage dynamics and where the experimental system resides in the parameter space of these timescales. It is easy to see that the timescale of pulsation τ_p, τ_w is roughly 30-60 s (see Fig.6.4 a) [11, 12]. The timescale for myosin turnover is 5-10 s (from FRAP experiments) and cadherin turnover timescales are reported to be $\sim$ 10 s (from FRAP experiments) [93, 92]. The timescale for length relaxation is inferred from local mechanical measurements in germband cells to be 3-5 s [76]. Thus the relevant regime of timescales for the junction remodeling dynamics seen in germband cell during intercalation would be $\tau_m, \tau_c, \tau_L << \tau_p, \tau_w$. This condition essentially means that the junction relaxation dynamics is faster than pulsation. So the junction would usually reach a steady state between any two pulses rendering collective effects of consecutive pulses to be negligible.

6.5.4 Robustness against noise?

The duration, amplitude and waiting time of the pulses (τ_p, A, τ_w respectively) are emergent quantities resulting from the local dynamics of actomyosin. So stochasticity in the local dynamics (such as molecular mechanisms of actomyosin dynamics, chemical regulation etc) can result in large pulse to pulse variation of the mentioned emergent quantities. This scenario poses a problem of robustness for the desired reliable stepwise shrinkage feature which is important for a timely completion of intercalation. We can see an increase in pulse amplitude (keeping everything else same) reduces the reliable stepwise shrinkage phase significantly (see Fig.6.7

b-c). This clearly states the lack of robustness in the proposed description of junction shrinkage dynamics. In the next section we extend the current description of junction shrinkage with the goal of achieving robust stepwise shrinkage or *robust ratcheting*.

6.6 Robust and reliable shrinkage requires medial and junctional myosin working in tandem

The role of actomyosin generated contractile forces in regulating E-cadherin dynamics has been studied [6, 93, 92] but how the active contractile forces effects cell-cell adhesion and tissue morphogenesis remain poorly understood.

The major active contractile force generator in the germband cell is the myosin minifilaments and this myosin population in the apical actomyosin layer can be divided into two different sub-populations, namely the medial myosin pool and the junctional myosin pool, with different mechanisms regulating various aspect of their dynamics [12, 89]. A recent study by Kale *et al* [88] indicates that these two different myosin pools effect E-cadherin dynamics at the junction differently in germband cell during intercalation.

The medial myosin activity increases E-cadherin level at the junctions (Fig.6.8) while the activity of junctional myosin reduces E-cadherin on the vertical junctions (Fig.6.8) which are undergoing stepwise shrinkage during intercalation [88]. This might stem from the difference in which medial and junction actomyosin interact with junction. The medial actomyosin mainly exerts normal forces at the junction while the junctional actomyosin, producing asymmetric forces at different sides [88] of the junction, leads to shearing of the junction. This shear stress at the junction results in stretching of the cadherin trans-bonds [94] which may lead to dissociation of cadherin trans-clusters. A negative correlation of junctional E-cadherin with inferred shear stress has been reported [88]. With this discussion in mind we propose a regulation of cadherin dynamics from both junctional and medial actomyosin and show that this can provide robustness of the stepwise shrinkage of the junction or *robust ratcheting*.

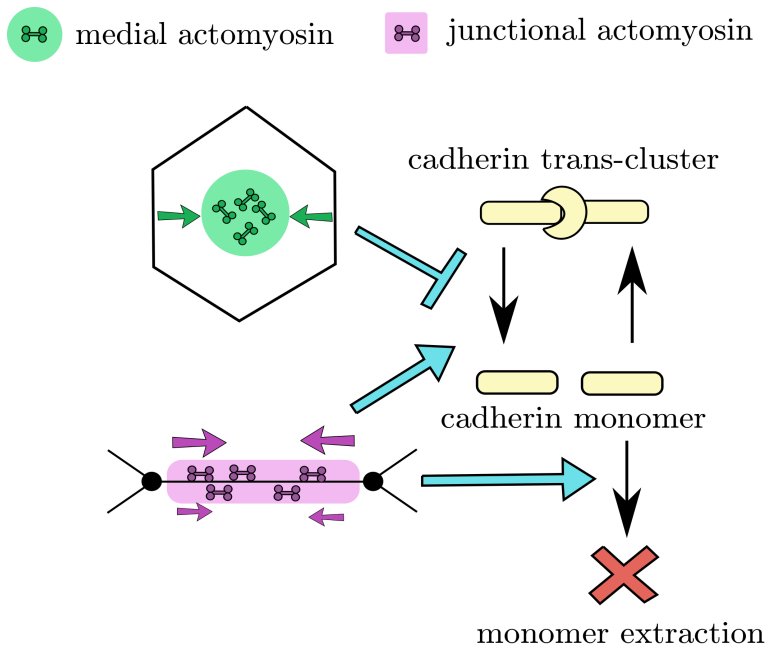

Figure 6.8. Medial and junctional myosin work in tandem to produce robust ratcheting of junction: The medial myosin activity increases E-cadherin level at the junctions by reducing trans-cluster fragmentation while the activity of junctional myosin reduces E-cadherin by increasing trans-cluster fragmentation on the vertical junctions which are undergoing stepwise shrinkage during intercalation.

6.6.1 Forces from medial actomyosin stabilize cadherin clusters

For description of robust ratcheting we recall the description given by the equations Eq.6.18 with constitutive relations described in Eq.6.9-6.10 and propose a modified aggregation-fragmentation dynamics with both medial and junctional actomyosin force dependent fragmentation of cadherin clusters with fragmentation time

$$\tau_f = \tau_{f0} e^{\gamma_1 (F^a - F_0^a)} e^{-\gamma_2 \zeta_1 \Delta\mu \Delta_M} . \tag{6.20}$$

Here γ_2 is a positive constant representing the medial actomyosin force dependence of fragmentation time and Δ_M is the *medial myosin pulse* given by $\Delta_M(t) = \Delta_J(t + \phi)$. We consider that the medial myosin pulse has the same amplitude and periodicity of the junctional myosin pulse as both Δ_M and Δ_J are originating from

the same actomyosin flow by spatially integrating over myosin density ($\rho(x,t)$) in the medial and junctional regions respectively. During the actomyosin flow actomyosin rich regions start flowing from the medial region towards the junctional region of the cell. Thus medial pulse precedes the junctional pulse. This delay in Δ_J is represented here by ϕ ($\phi > 0$) and has been estimated to be $\sim 10\,s$ [12].

Now γ_2 being positive the force from medial pulse ($-\zeta_1 \Delta\mu \Delta_M$) will increase fragmentation time of cadherin cluster thereby stabilizing the cadherin cluster amount in the junction. Higher fragmentation time will result in less amount of cadherin monomers. Thus a reduction in extraction of cadherin will follow as the extraction of cadherin is proportional to the available monomer numbers ($S_1 \propto \rho_1$). Note that there is a overlap in medial and junctional pulse signals controlled by the delay ϕ. Also note that the cadherin extraction happens due the myosin influx via junctional pulse (Fig.6.8) while medial pulse results in reduced extraction via stabilization of cadherin trans-clusters (Fig.6.8). Thus in the current description the overlap between Δ_M and Δ_J controlled by ϕ will effect cadherin extraction with more overlap resulting in less extraction of cadherin.

6.6.2 Robustness of stepwise shrinkage : Against external noise

With the above specified description for junction shrinkage we do see a recovery of the reliable stepwise shrinkage phase against parameter variation in the myosin pulse (see Fig.6.9 a-b). This recovery of the stepwise shrinkage phase occurs via reduction in the cases of junction collapse because of stabilization of E-cadherin trans-clusters.

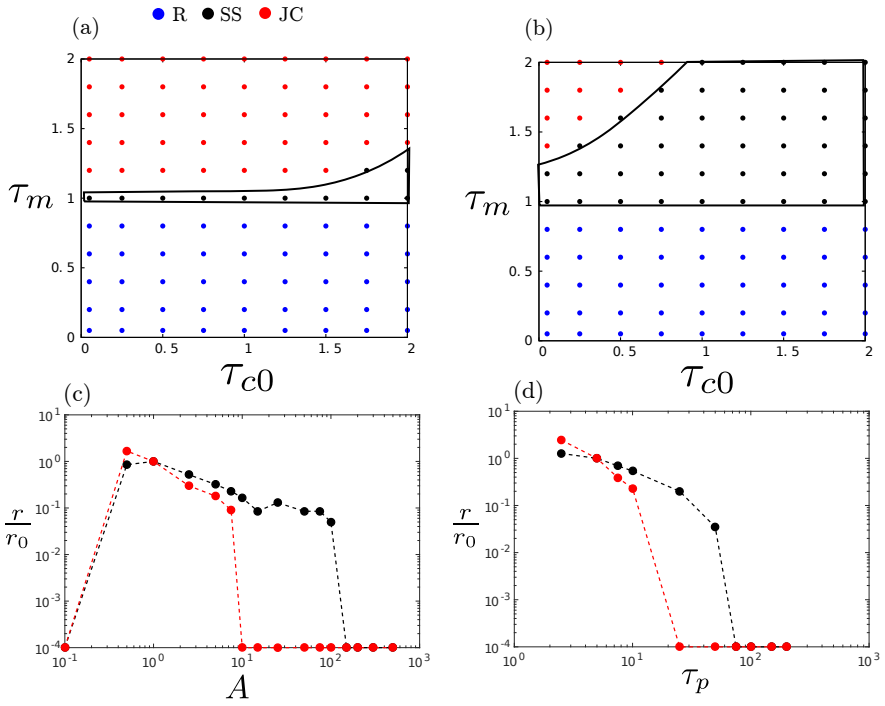

Figure 6.9. Robustness of stepwise shrinkage phase via medial pulse dependent stabilization of cadherin clusters: Recovery of the reliable stepwise shrinkage phase in cadherin relaxation time (τ_{c0}) and myosin relaxation time (τ_m) phase diagram, upon introducing medial myosin pulse dependent stabilization of cadherin trans-clusters (a) $\gamma_2 = 0$ (means no effect of myosin pulse on cadherin dynamics), (b) $\gamma_2 = 1$. (c) Robustness of stepwise shrinkage against pulse amplitude A calculated from area of the stepwise shrinkage phase for $\gamma_2 = 0$ (red) and $\gamma_2 = 1$ (black) with $\phi = \frac{0.25}{A}$. (d) Robustness of stepwise shrinkage against pulse duration τ_p calculated from area of the stepwise shrinkage phase for $\gamma_2 = 0$ (red) and $\gamma_2 = 1$ (black) with $\phi = \frac{0.25}{A}$ and $A = 1$. Here we take $\zeta_2 = 0$, $\theta = 1$, $\rho_m^c = 2$, $n(0) = 10$ and the other parameter values used for both the phase diagrams are given below (Table.6.4).

Table 6.4. Parameter values

$\beta_1 = 2$	$\beta_2 = 1$	$-\zeta_1 \Delta\mu = 1.5$	$\tau_p, \tau_w = 5$
$\tau_L = 0.2$	$\rho_{m0} = 1$	$\gamma_1 = 0.5$	$L^* = 0.1$

To probe robustness for stepwise shrinkage, first we calculated the phase diagram in cadherin relaxation time and myosin relaxation time myosin for a single set of

parameters and define this set as *null set* and calculate the area for the stepwise shrinkage phase for the null set given by r_0. Now we vary the pulse amplitude (A) and pulse duration (τ_p) over a large range of values and calculate the phase diagram for each values of these parameters and determine the area for the stepwise shrinkage phase r for all the cases. Finally we compare the ratio of the area of stepwise shrinkage phase, given by ($\frac{r}{r_0}$), for this current description of junction shrinkage dynamics with ($\frac{r}{r_0}$) calculated for leaky cadherin description (Eq.6.18). From this comparison we can see that with the stabilization of cadherin clusters from medial pulse we can achieve robustness of the stepwise shrinkage phase over a few decades of variation in pulse amplitude and pulse duration (see Fig.6.9 c-d).

6.6.3 Robustness of stepwise shrinkage : Against internal noise

The robustness against noise in myosin or cadherin dynamics (internal noise) can be probed in the current description of junction shrinkage dynamics. We take an additive Gaussian white noise in the junctional myosin dynamics and calculate the robustness from the stepwise shrinkage phase area (Fig.6.10).

Introducing internal noise in the dynamics produce a mixed state (Fig.6.10 a) of stepwise shrinkage and junction collapse. We see a significant recovery of the stepwise shrinkage phase area from the medial myosin stabilization of E-cadherin (Fig.6.10 b) indicating robustness against internal noise.

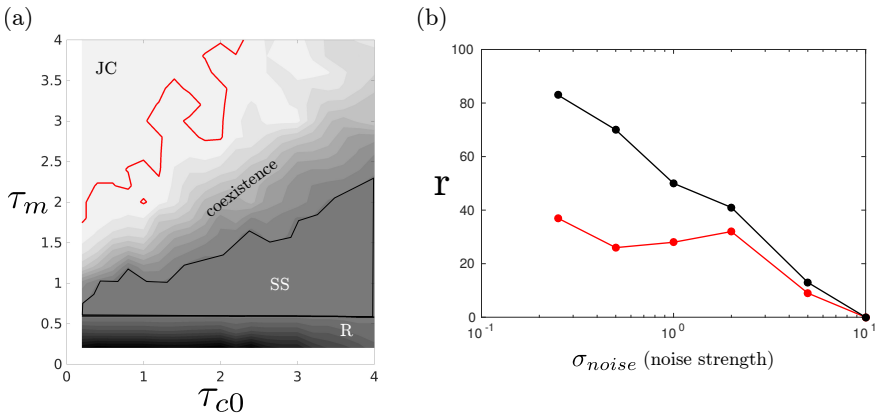

Figure 6.10. Robustness of stepwise shrinkage phase via medial pulse dependent stabilization of cadherin against internal noise: (a) Phase diagram in force independent cadherin relaxation time (τ_{c0}) and myosin relaxation time (τ_m) for junction myosin noise $\sigma_{noise} = 0.5$ shows a coexistence phase of stepwise shrinkage and junction collapse. Usual phases are reversible or unreliable junction shrinkage (R), reliable stepwise shrinkage (SS) and junction collapse (JC). (b) Robustness of stepwise shrinkage against noise strength σ_{noise} calculated from area of the stepwise shrinkage phase (r) for $\gamma_2 = 0$ (red) and $\gamma_2 = 1$ (black). Here we take $\phi = \frac{0.25}{A}$, $A = 2$, $\zeta_2 = 0$, $\theta = 1$, $\rho_m^c = 2$, $n(0) = 10$ and the other parameter values used for both the phase diagrams are given below (Table.6.5). All phase diagrams were averaged over 16 ensembles.

Table 6.5. Parameter values

$\beta_1 = 1$	$\beta_2 = 0.5$	$-\zeta_1 \Delta\mu = 0.5$	$\tau_p, \tau_w = 5$
$\tau_L = 0.5$	$\rho_{m0} = 1$	$\gamma_1 = 0.2$	$L^* = 1$

6.7 Concluding remarks and future directions

In this chapter we have proposed a theoretical description for the dynamics of junction shrinkage in terms of integrated quantities $(L(t), \rho_m(t), \rho_c(t), \rho_1(t))$ starting from a local description of displacement field and respective densities (Section.6.2). The approximate analytical studies of Eq.6.13 and Eq.6.18 successfully captured the dynamical response of the junction to contractile forces from the myosin pulse.

Studying the resulting descriptions we determine the important consequence of cadherin turnover from the junction: Without cadherin turnover (i.e., in the fixed cadherin level dynamics) we do not get reliable stepwise shrinkage. The active force driven extraction of cadherin is essential to produce permanent deformation of the junction that results in reliable stepwise shrinkage. Further study of the junction shrinkage dynamics with cadherin turnover reveals the lack of robustness in the stepwise shrinkage phase against noise in the myosin pulse. This brings out the need for robustness in stepwise shrinkage dynamics of junction. Here we propose a mechanism where contractile forces from junctional actomyosin and medial actomyosin effect the cadherin dynamics differently (as suggested in the recent work [88]). We show that this force dependent regulation of cadherin gives rise to a mechanism which can achieve robust stepwise shrinkage of the junctions against variation in myosin pulse (external noise) and noisy myosin dynamics (internal noise).

Despite the theory successfully capturing the qualitative nature of the junction shrinkage during germband extension, we do acknowledge the lack of comprehensive comparison with *in vivo* experimental results. Further experiments to explicitly validate the assumptions in the theory and the predicted results are needed for the maturation of this current study of junction shrinkage.

End of Chapter

Chapter A

Appendix

A.1 Strain dependent unbinding

For the turnover of bound myosin filament density, we allow for a possible strain-induced unbinding of the Hill-form, $k_u = k_{u0} e^{\alpha \nabla \cdot \mathbf{u}}$. The sign of the coefficient α can be taken to be either positive or negative (Fig. SA.1 a,b) : $\alpha > 0$ implies a local extension (compression) of the mesh will increase (decrease) the myosin unbinding, while $\alpha < 0$ implies a local compression (extension) of the mesh will increase (decrease) the myosin unbinding. The choice $\alpha = 0$ implies that the myosin unbinding rate is a constant, independent of mesh deformation. We thus cover all possibilities.

Changing the sign of α only affects the placement of the phase boundaries, but not the qualitative aspects of the phases (see Fig. SA.1 b,c). We find that the oscillatory phase exists, as long as the eigenvalue $Im[\lambda_{\pm}] < 0$, from which get the maximal (positive) value $\alpha_{max}(B, \zeta_1, \ldots)$, beyond which there are no oscillations. Thus to get oscillations for a given set of (other) parameters, we have to set $-\infty < \alpha < \alpha_{max}$. We have taken $\alpha > 0$ (but smaller than α_{max}) in all numerical results presented in the main text.

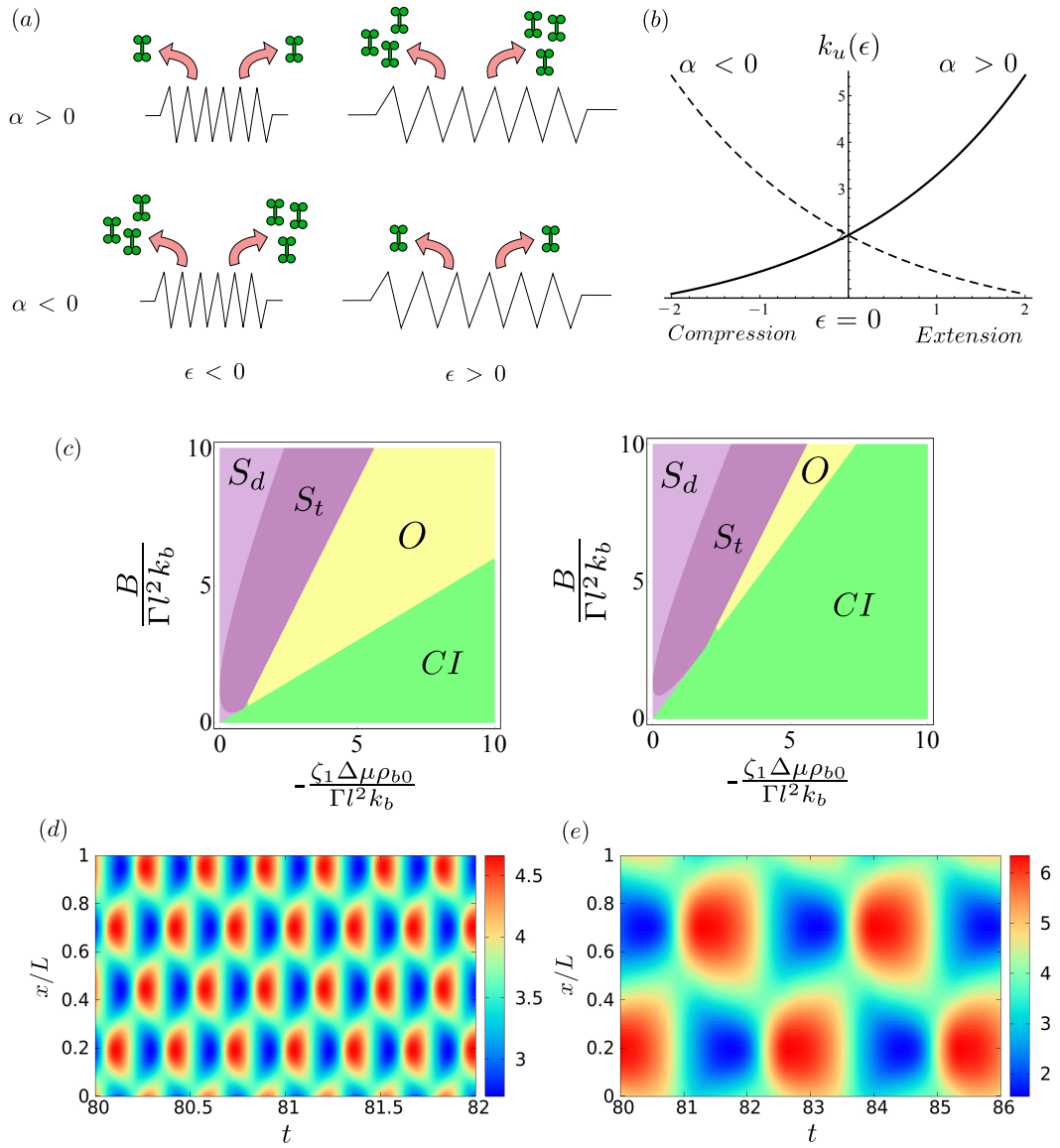

Figure A.1. Strain dependent unbinding: effect of α sign. (a)Scehematic describing the effect of local compression and extension on strain dependent unbinding. (b) Plot of unbinding rate $k_u(\epsilon)/k_{u0}$ with strain ϵ, for both positive and negative α. (c, left and right) Sign of α does not change the qualitative nature of the phase diagram in the effective elastic stress density versus active stress density (nomalized to the frictional stress), as long as $\alpha < \alpha_{max}$. The color scheme and legend are as in Fig.3.4, (left) $\alpha = -0.5$ and (right) $\alpha = 0.5$. Other parameters are $k = 10$, $c = 0.1$ and $D = 0.1$. Note that the regime of oscillations is larger when $\alpha < 0$. Numerical solutions of myosin density (ρ_b) kymographs showing oscillations with (d) $\alpha = -5$ and (e) *alpha* $= 3$. Other parameter values are $B = 8$, $-\zeta_1 \Delta\mu = 5.2$, $k = 0.2$,$D = 0.2$.

A.2 Numerical methods

Since the dynamical equations have nonlinear advection and diffusion, care must be taken in evaluating the flux due to dissipative and dispersive errors arising from spatial discretization. We use the finite volume method for spatial discretization [77], which has been found to be useful for non-linear advection equations [78].

We calculate the numerical flux using the Van-Leer's flux limiter, which uses a different formula to calculate the spatial derivative depending on how sharply the ρ_b profile changes in space. When the profile changes very fast, the scheme implements the upwind method [79] which reduces the dispersion error through numerical diffusion. When the profile changes smoothly the scheme implements a second order accurate method called Lax-Wendroff method [80]. In our numerical scheme, the density (ρ_b or ρ) flux on the interface between i^{th} and $(i-1)^{th}$ node is computed as,

$$\begin{aligned} f_{i-\frac{1}{2}}^{n+\frac{1}{2}} &= \frac{1}{2} v_{i-\frac{1}{2}} [(1+\theta_{i-\frac{1}{2}})\rho_{i-1}^n + (1-\theta_{i-\frac{1}{2}})\rho_i^n] \\ &+ \frac{1}{2}|v_{i-\frac{1}{2}}| \left(1 - \left|\frac{v_{i-\frac{1}{2}}\Delta t}{\Delta x}\right|\right) \phi_{i-\frac{1}{2}}^n(r_{i-\frac{1}{2}}^n) \left(\rho_i^n - \rho_{i-1}^n\right) \end{aligned} \tag{A.1}$$

Here $v_{i-\frac{1}{2}} = \frac{v_i - v_{i-1}}{2}$ and

$$\theta_{i-\frac{1}{2}} = \begin{cases} +1, & \text{if } v_{i-\frac{1}{2}} > 0 \\ -1, & \text{if } v_{i-\frac{1}{2}} \leq 0 \end{cases} \tag{A.2}$$

$$r_{i-\frac{1}{2}}^n = \begin{cases} \frac{\rho_{i-1}^n - \rho_{i-2}^n}{\rho_i^n - \rho_{i-1}^n}, & \text{if } v_{i-\frac{1}{2}} > 0 \\ \frac{\rho_{i+1}^n - \rho_i^n}{\rho_i^n - \rho_{i-1}^n}, & \text{if } v_{i-\frac{1}{2}} \leq 0 \end{cases} \tag{A.3}$$

The function $\phi(r)$ is the Van Leer flux limiter

$$\phi(r) = \frac{r + |r|}{1 + |r|}\,. \tag{A.4}$$

The time integration is done with a total variation diminishing (TVD) 3^{rd}order Runge-kutta method [81]. All other derivative terms were discretized using a simple finite difference. The initial conditions were chosen from a uniform random distribution of fixed width about a uniform, unstrained configuration. We used periodic boundary conditions throughout and a time-space discretization, $\Delta t = 10^{-4}$ and $\Delta x = 5 \times 10^{-2}$.

A.3 Experimental methods

For fluorescence time-lapse imaging, embryos at stage 7 were dechorionated with 100% bleach and mounted on No. 1 coverslip with halocarbon oil [82]. A 100X, 1.4 N.A oil immersion objective with Nikon spinning disc Eclipse Ti inverted microscope was used [82]. The system acquires images using the MetaMorph software. Starting from the most apical plane, 4- 7 z-sections $0.5\,\mu$m apart were acquired every $1.5-4$s (depending on the experiment) using a single camera. Sum-intensity z-projection of slices was used for all quantifications, followed by a background subtraction using the available plugin in Fiji.

A.4 Image analysis : Actomyosin pulsation and flow

All data analysis are done using customized code written in MATLAB. For realization of pulse shape, velocity and skewness pulses were projected on the line of their movement.

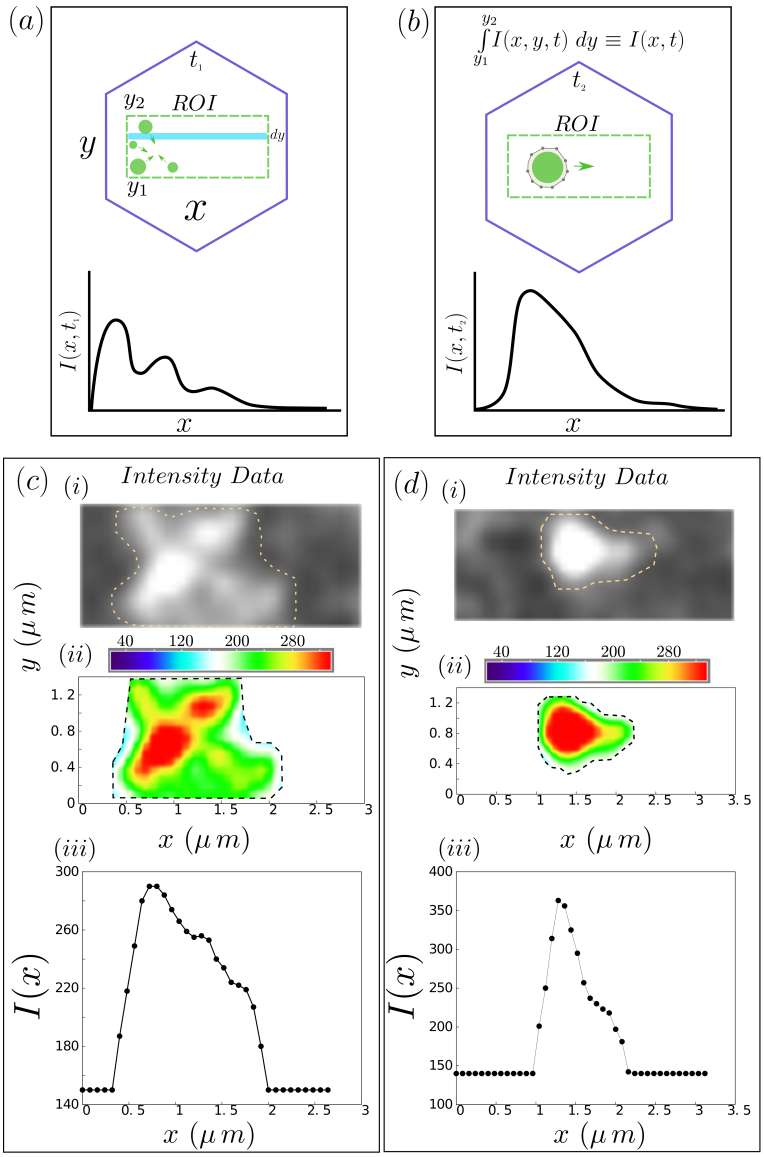

Figure A.2. Protocol for image analysis of the experiments on the dynamics of labeled medial myosin. (a,b) We collect the 2d intensity map ($I(x, y, t)$) of myosin (green dots) at different times, e.g., t_1, t_2 (with $t_2 > t_1$), within a thin rectangular strip (green rectangle) chosen so that it is not contaminated by signals at the cell boundary. After background subtraction, we integrate the intensity $I(x, y, t)$ along y between the limits y_{min} and y_{max}, along each thin rectangular strip (blue). This gives us the 1-dimensional profile $I(x, t)$ vs. x, as shown schematically here. (c,d)(i) We carry out the above protocol for the labeled myosin-dense images obtained in two different experiments. (ii) After background subtracting the intensity maps, we plot $I(x, y, t)$ in the $x - y$ plane. (iii) The 1D projection $I(x, t)$ is plotted versus x.

A.5 Junction shrinkage calculations

Dynamics equations for junction length :

To get junction length dynamics, we integrate over space and go to ODE's.

We first consider the local force balance on a 1D junction given by

$$\Gamma\left(\dot{u}-v\right)=\partial_x\sigma(x,t)\,. \tag{A.5}$$

The stress σ is composed of elastic, dissipative and active contributions:

$$\sigma(t)=\sigma^e+\sigma^d+\sigma^a \tag{A.6}$$

The elastic stress is written $\sigma^e = B\left(\partial_x u-\epsilon_0(...)\right)$, where ϵ_0 is a reference strain which, as we develop below, depends on variables such as the cadherin density. The dissipative stress is $\sigma^d = \eta\partial_x\dot{u}$; together, σ^e and σ^d specify the viscoelastic relaxational dynamics of the junction. The active stress is a function of the local junctional myosin density, $\sigma^a(\rho)$.

Assuming negligible movement of junctional actomyosin with respect to the lipid bilayer ($\Gamma\left(\dot{u}-v\right)=0$), force balance implies a spatially homogeneous total stress ($\sigma=\sigma_0(t)$) profile, which could depend on time. By continuity of stress, we identify σ_0 with the boundary stress exerted by neigbouring junctions.

Integrating over the reference coordinate x, which takes values from 0 to L_R:

$$\begin{aligned}\int_0^{L_R}\sigma_0\,dx = B\int_0^{L_R}\left(\partial_x\boldsymbol{u}-\epsilon_0\right)dx+\eta\int_0^{L_R}\partial_x\dot{\boldsymbol{u}}\,dx\\ +\int_0^{L_R}\sigma^a(\rho)\,dx\end{aligned} \tag{A.7}$$

we find an ODE for the dynamics of the junction length L, defined as $L_R + \int_0^{L_R} dx\, \partial_x u$:

$$\dot{L} = -\frac{B}{\eta}\left(L - \underbrace{\left(L_R + \frac{L_R}{B}\sigma_0(t) + L_R\bar{\epsilon}_0(...)\right)}_{L_0}\right) + \frac{L_R}{\eta}\bar{\sigma}^{(a)}(\rho) \tag{A.8}$$

L_0 is the rest length of the junction emerging from molecular components of the junction and phenomenology of the system. Here the overbar indicates an average over the junction length.

Dynamics equations for junctional myosin :

To derive the dynamical equation for the total junctional myosin ($\rho_m(t)$) we start with the microscopic description of the local bound myosin density at junction ($\rho(x,t)$).

$$\partial_t\rho + \partial_x J = k_b - k_u\rho + P(x,t) \tag{A.9}$$

Here $J(x,t)$ is the current due to diffusion and advection of bound myosin with the cortex mesh and k_b, k_u are the binding and unbinding rates respectively and $P(x,t)$ denotes the myosin influx to junctional myosin density $\rho(x,t)$ coming from the medial actomyosin flow. Similarly as before if we integrate over the space to derive an ODE describing the dynamics of total myosin amount $\rho_m = \int_0^{L_R}\rho(x,t)\,dx$ we get

$$\begin{aligned}\int_0^{L_R}\partial_t\rho\,dx + \int_0^{L_R}\partial_x J\,dx = k_b\int_0^{L_R}dx - k_u\int_0^{L_R}\rho\,dx \\ + \int_0^{L_R}P(x,t)\,dx\end{aligned} \tag{A.10}$$

Rewriting this in terms of ρ_m we get

$$\dot{\rho}_m = k_b L_R - k_u\rho_m + \Delta_J(t) - (J(L,t) - J(0,t)) \tag{A.11}$$

The last term on the right is the boundary perturbations of flux which we assume

to be have slower dynamics than ρ_m and Δ_J represents the total amount of myosin that arrives at the junction due to medial myosin pulse $P(x,t)$. So finally we arrive at

$$\dot{\rho}_m = -\left(\frac{\rho_m - \rho_{m0}}{\tau_m}\right) + \Delta_J(t) \tag{A.12}$$

Here $\tau_m = k_u^{-1}$ and $\rho_{m0} = \frac{k_b L_R}{k_u}$

Dynamics equations for cadherin clusters : E-cadherin monomers and trans cluster dynamics is given by

$$\begin{aligned}
\partial_t \rho_1' + \partial_x J_1 &= -\frac{\rho_1'}{\tau_a} + \frac{\rho_c'}{\tau_f} + s_1(x,t) \\
\partial_t \rho_c' + \partial_x J_c &= -\frac{\rho_c'}{\tau_f} + \frac{\rho_1'}{\tau_a} + s_c(x,t)\,.
\end{aligned} \tag{A.13}$$

Similarly as before if we integrate over the space to derive an ODE describing the dynamics of total cadherin monomer and trans-cluster amount $\rho_{1,c} = \int_0^{L_R} \rho_{1,c}'(x,t)\,dx$ we get

$$\begin{aligned}
\dot{\rho}_1 &= \frac{\rho_c}{\tau_f} - \frac{\rho_1}{\tau_a} + S_1 \\
\dot{\rho}_c &= -\frac{\rho_1}{\tau_a} + \frac{\rho_c}{\tau_f} + S_c\,.
\end{aligned} \tag{A.14}$$

Here $S_{1,c} = \int_0^{L_R} s_{1,c}(x,t)\,dx$ and ρ_1 and ρ_c are the total amount of E-cad in monomeric state which does not contribute in mechanical properties of the junction and total amount of E-cad cluster which contribute to the mechanical properties of the junction respectively. τ_a and τ_f are the aggregation and fragmentation timescale for E-cad and S_1 and S_c are the source/sink term for monomer and cluster respectively.

A.6 Approximate analytical solutions: Fixed cadherin level dynamics (single pulse)

Here we take the total amount of cadherin to be a constant, i.e. $\rho_1 + \rho_c = n$, with no source or sink. The dynamical equations in this model are

$$\begin{aligned} \dot{L} &= -\frac{L - L_0(\rho_c)}{\tau_L} + \zeta_1 \Delta\mu \rho_m \\ \dot{\rho}_m &= -\frac{\rho_m - \rho_{m0}}{\tau_m} + \Delta_J(t) \\ \dot{\rho}_c &= -\frac{\rho_c - \rho_{c0}(\rho_m)}{\tau_c(\rho_m)} \,. \end{aligned} \tag{A.15}$$

Essential elements and ideas of the conservative model are

- Total amount of cadherin remains conserved : $\rho_1 + \rho_c = n$, i.e. $\dot{n} = 0$. This implies $S_1 + S_c = 0$ and to keep the analytics simple we take S_1, $S_c = 0$.
- The constraint from the conservation of the total cadherin amount ($\dot{n} = \dot{\rho}_1 + \dot{\rho}_c = 0$) allows us to reduce the dynamics of monomer and cluster to only the dynamics of the clusters as given by the above equation (Eq.A.15).
- cadherin fragmentation rate depends on active force at junction : increases with increasing active force. The fragmentation time is given by $\tau_f(\rho_m) = \tau_{f0} e^{\gamma_1 (F^a - F^a_0)} = \tau_{f0} e^{\gamma_1 \zeta_1 \Delta\mu (\rho_m - \rho_{m0})}$.
- We shall assume $\tau_{f0} = \tau_{a0} = \tau$ to keep the analytics simple without any qualitative loss of understanding.
- Change in myosin amount ρ_m will result in change in cadherin cluster amount ρ_c as the relaxation timescale τ_c and the steady state cluster amount ρ_{c0} are

function of active force and will be respectively given by

$$\begin{aligned} \tau_c &= \frac{\tau e^{\gamma_1(F^a - F_0^a)}}{1 + e^{\gamma_1(F^a - F_0^a)}} \\ &= \left(\frac{\tau\alpha}{1+\alpha}\right) \end{aligned} \tag{A.16}$$

and

$$\begin{aligned} \rho_{c0} &= \left(\frac{\tau_c}{\tau_a}\right) n \\ &= \left(\frac{\alpha}{1+\alpha}\right) n \end{aligned} \tag{A.17}$$

where $\alpha = e^{\gamma_1(F^a - F_0^a)}$

- We assume a simpler linear relation for cadherin dependence of rest length

$$L_0(\rho_c) = L^* + \beta_1 \rho_c \tag{A.18}$$

- at very low values of the junction length $L \to 0$ we assume that the junction has been remodelled and changed its alignment accordingly through T_1 process.

Response of the junction upon arrival of a pulse will certainly depend on the properties of the pulse-signal Δ_J. Properties of the signal $\Delta_J(t)$ are defined by four parameters namely the amplitude of the pulse, duration of the pulse, waiting time between two pulses and noise in the signal, given by A, τ_p, τ_w and δ respectively. We shall use the below defined functional form in this study unless specified otherwise

$$\begin{aligned} \Delta_J(t) = A \sum_{i=1}^{n_p} (H(t - t_i) \\ -H(t - (t_i + \tau_p)) + \delta(t) \end{aligned} \tag{A.19}$$

Where $H(t)$ is an *Heaviside step function* defined as $H(x) = \frac{d}{dx} max\{x, 0\}$ and

$t_i = t_0 + (i-1)(\tau_p + \tau_w)$ where the pulses start from $t = t_0$. For most of the discussions in this section we consider the pulses are noise free, $\delta = 0$. To understand the junction shrinkage in a simple manner we have considered pulses of rectangular shape here but this restriction does not curtail our understanding of the system.

We shall now divide the analysis of junction dynamics for a single pulse ($n_p = 1$) and for a pulse train ($n_p > 1$) in two different sections below.

Myosin dynamics : We first solve for with the myosin dynamics as it is not coupled to length and cadherin dynamics. In the case of a single myosin pulse ($n = 1$, i.e. pulse is "ON" while $t_0 < t < t_0 + \tau_p$) the solution for ρ_m will be given by

$$\rho_m(t) = \begin{cases} \rho_{m0} + (\rho_m(0) - \rho_{m0})e^{-\frac{t}{\tau_m}} & \text{for } t < t_0 \\ \rho_{m0} + (\rho_m(t_0+\tau_p) - \rho_{m0})e^{-\frac{t-(t_0+\tau_p)}{\tau_m}} & \text{for } t > t_0 + \tau_p \\ \rho_{m0} + A\tau_m(1 - e^{-\frac{t-t_0}{\tau_m}}) & \\ +(\rho_m(t_0) - \rho_{m0})e^{-\frac{t-t_0}{\tau_m}} & \text{otherwise} \end{cases} \tag{A.20}$$

The important features of myosin dynamics that are evident from the solution are

- If $\tau_p \to \infty$ then myosin reaches a steady state at $\rho_m = \rho_{m0} + \tau_m A$
- For any finite τ_p, at the end of the pulse, myosin reaches a value $\rho_m(t_0+\tau_p) = \rho_{m0} + A\tau_m(1 - e^{-\frac{\tau_p}{\tau_m}})$. For limiting cases this value can be approximated as $\rho_{m0} + A\tau_p$ (when $\frac{\tau_p}{\tau_m} << 1$) or $\rho_{m0} + A\tau_m$ (when $\frac{\tau_p}{\tau_m} >> 1$).

Cadherin dynamics : Now we consider the dynamics of cadherin cluster (ρ_c) dynamics. Note that the instantaneous amount of cadherin cluster ρ_c depends on the amount of myosin ρ_m as the fragmentation rate τ_f depends on active force F^a .

- The cadherin cluster equation can be solved exactly if we assume some approximations of the nonlinear dependence of fragmentation rate upon active force. As we know from definition of active force $F^a < 0$ and with a pulse induced enrichment of total myosin if ρ_m increases sufficiently, fragmentation

time will decrease $\tau_f << 1$ as $\alpha << 1$. We assume the form for cadherin relaxation time and ρ_{c0} to be

$$\begin{aligned} \tau_c &\simeq \alpha\tau \\ \rho_{c0} &\simeq \alpha n \end{aligned} \tag{A.21}$$

- We also approximate the early change (i.e. $t - t_0 \sim$ small, positive) in ρ_m upon arrival of pulse as

$$\begin{aligned} \rho_m(t) &= \rho_{m0} + A\tau_m(1 - e^{-\frac{t-t_0}{\tau_m}}) \\ &\simeq \rho_{m0} + A\tau_m\left(1 - (1 - \frac{t-t_0}{\tau_m})\right) \\ &= \rho_{m0} + A(t - t_0) \end{aligned} \tag{A.22}$$

  Here we have set t_0 to be $t_0 >> \tau_m$ (i.e., $e^{-\frac{t_0}{\tau_m}} \to 0$) to further simplify calculations without any loss of generality. Now we describe α as

$$\alpha = \begin{cases} e^{\gamma_1\zeta_1\Delta\mu A(t-t_0)} & \text{for } t - t_0 << \tau_m \\ e^{\gamma_1\zeta_1\Delta\mu A\tau_m} & \text{for } t - t_0 >> \tau_m \end{cases} \tag{A.23}$$

With the above described assumptions we write down the exact solution for total

cadherin cluster ρ_c as

$$\rho_c(t) = \begin{cases} \rho_{c0} + (\rho_c(0) - \rho_{c0})e^{-\frac{t}{\tau_c}} & \text{for } t < t_0 \\ \rho_{c0} + (\rho_c(t_0+\tau_p) - \rho_{c0})e^{-\frac{t-(t_0+\tau_p)}{\tau_c}} & \text{for } t > t_0 + \tau_p \\ \rho_c(t_0)e^{-p_0}e^{p_1(t)} + \frac{\rho_{c0}}{\gamma_1\zeta_1\Delta\mu A\tau}e^{p_1(t)} & \\ \times\left(E(-p_0) - E(-p_1(t))\right) & \text{for } t - t_0 << \tau_m \\ \rho_c(t')e^{\frac{-t}{\tau_c}} + n\left(\frac{e^{\gamma_1\zeta_1\Delta\mu A\tau_m}}{1+e^{\gamma_1\zeta_1\Delta\mu A\tau_m}}\right)\left(1 - e^{\frac{-t}{\tau_c}}\right) & \text{for } t - t_0 >> \tau_m \end{cases} \tag{A.24}$$

Where $p_0 = e^{\frac{e^{\gamma_1\zeta_1\Delta\mu A t_0}}{\gamma_1\zeta_1\Delta\mu A\tau}}$, $p_1 = e^{\frac{e^{-\gamma_1\zeta_1\Delta\mu A(t-t_0)}}{\gamma_1\zeta_1\Delta\mu A\tau}}$, $E(x)$ denotes the *exponential integral function* given by $\int_x^\infty \frac{e^{-t}}{t}\,dt$ and $\rho_c(t')$ defines a intermediate value at $t - t_0 \sim \tau_m$. These piecewise solutions approximately trace the dynamics of cadherin clusters.

Length dynamics : With the knowledge of instantaneous values of the amount of myosin and cadherin clusters we can ask for the response of the pulse in terms of the length of the junction L. Away from the pulse (i.e., L_0 is constant) the exact solution will be

$$L(t) = \begin{cases} L_0 + \tau_L F^a & \\ + \left(L(0) - (L_0 + \tau_L F^a)\right) e^{-\frac{t}{\tau_L}} & \text{for } t < t_0 \\ L_0 + \tau_L F^a & \\ + \left(L(t_0+\tau_p) - (L_0 + \tau_L F^a)\right) e^{-\frac{t-(t_0+\tau_p)}{\tau_L}} & \text{for } t >> t_0 + \tau_p \end{cases} \tag{A.25}$$

To understand the response in junction length in terms of the phases defined we can look at the value of steady state length of the junction L^s at the end of the pulse at $t = t_0 + \tau_p$.

- Looking at the Eq.A.25, it is clear that before and after the pulse the junction length reaches a steady state value $L_0 + \tau_L F^a$ which remains unaffected by

the pulse. Thus in the context of *conserved model* it is not possible to get ratcheting which gives rise to stepwise shrinkage of the junction. This logic can be stretched for a pulse train too. In that case away from the pulse train with n pulses (i.e., $t < t_0$ and $t > t_0 + (n-1)(\tau_p + \tau_w) + \tau_p$) the solution for length will behave in the very same way.

- We know from solutions of $\rho_m(t)$ that at the end of the pulse myosin reaches a value given by $\rho_{m0} + A\tau_m(1 - e^{-\frac{\tau_p}{\tau_m}})$ and cadherin clusters amount can be approximated to be $\left(\frac{\alpha}{1+\alpha}\right) n$ where $\alpha = e^{\gamma_1\zeta_1\Delta\mu A\tau_m(1-\chi^p)}$ where $\chi^p = e^{-\frac{\tau_p}{\tau_m}}$.

- Now the approximate expression for steady state length of junction at the end of the pulse can be written as

$$\begin{aligned} L^s \simeq L^* + \beta_1 \left(\frac{e^{\gamma_1\zeta_1\Delta\mu A\tau_m(1-\chi^p)}}{1 + e^{\gamma_1\zeta_1\Delta\mu A\tau_m(1-\chi^p)}} \right) n \\ +\tau_L\zeta_1\Delta\mu \left(\rho_{m0} + A\tau_m(1-\chi^p)\right) \end{aligned} \tag{A.26}$$

- Now the condition

$$\begin{aligned} L^* + \beta_1 \left(\frac{e^{\gamma_1\zeta_1\Delta\mu A\tau_m(1-\chi^p)}}{1 + e^{\gamma_1\zeta_1\Delta\mu A\tau_m(1-\chi^p)}} \right) n \\ +\tau_L\zeta_1\Delta\mu \left(\rho_{m0} + A\tau_m(1-\chi^p)\right) \leqslant 0 \end{aligned} \tag{A.27}$$

will dictate the resulting junction shrinkage from the pulse will be a junction collapse when the above condition is true or a reversible shrinkage when $L^s > 0$.

- Phase diagrams constructed from the above expression (and other analysis like these) will significantly deviate from the true results when relaxation of length and cadherin is slower than the timescales of pulsation (i.e., τ_L, $\tau_c \gtrsim \tau_p$, τ_w).

A.7 Approximate analytical solutions: Fixed cadherin level dynamics (pulse train)

Now we consider a pulse train ($n_p > 1$ in Eq.A.19) instead of a single pulse. It can be understood from the single pulse results that if the temporal separation between pulses (τ_w) is large enough then all the results of single pulse analysis will hold for the pulse train too, i.e., the response of the junction remains similar as seen in single pulse and they just repeat the same response of reversible shrinkage or junction collapse with every coming pulse. However when τ_w is small the response of the junction from a coming pulse will depend on the previous pulse too. Below we elaborate these concepts and try to understand the junction dynamics at τ_w small limit.

- When τ_m, $\tau_c << \tau_p$, τ_w the effect of the pulse train can essentially be understood as mere repetitions a of single pulse in time. The phase diagrams and the approximate solutions wont change in this case.

- When τ_m, $\tau_c > \tau_p$, τ_w myosin (ρ_m) and cadherin cluster (ρ_c) relaxation is slower compared to the timescales of the pulsation and the resulting dynamics can be understood using the piecewise solution of ρ_m and ρ_c in presence and absence of pulse. The piecewise solutions for ρ_m for the first pulse will be

$$\begin{aligned} \rho_m(\tau_p) &= \rho_{m0} + A\tau_m(1-\chi^p) \\ \rho_m(\tau_p+\tau_w) &= \rho_{m0} + A\tau_m(1-\chi^p)\chi^w \end{aligned} \tag{A.28}$$

  The above relations are derived from the solution $\rho_m(t) = \rho_{m0} + A\tau_m(1 - e^{\frac{-t}{\tau_m}}) + (\rho_m(0) - \rho_{m0})e^{\frac{-t}{\tau_m}}$ and assuming $\rho_m(0) = \rho_{m0}$ for the first equation and taking $\rho_m(0) = \rho_m(\tau_p)$ for the second equation and pulse starting time is taken to be $t_0 = 0$ throughout in this section. Here $\chi^p = e^{\frac{-\tau_p}{\tau_m}}$ and $\chi^w = e^{\frac{-\tau_w}{\tau_m}}$. Following similar calculations we can calculate the the value of ρ_m at the end

of nth pulse (at $t = n(\tau_p + \tau_w)$) to be

$$\begin{aligned} \rho_m^n &= \rho_{m0} + A\tau_m\left((1-\chi^p)S^n + \chi^p\right) \\ S^n &= \sum_{k=0}^{n} e^{-k\,\frac{(\tau_p+\tau_w)}{\tau_m}} \\ &= \left(\frac{1}{1-\chi^p\chi^w}\right)\left(1-(\chi^p\chi^w)^{(n+1)}\right) \end{aligned} \tag{A.29}$$

- The resulting dynamics for ρ_m for a large train of pulses ($n \to$ large) can be calculated from the above results at time when $n(\tau_p + \tau_w)$ is large compared to τ_m. The value of ρ_m will periodically change between a high ρ_m^H and a low value ρ_m^L given by

$$\begin{aligned} \rho_m^H &= \rho_{m0} + A\tau_m\phi^H \\ \rho_m^L &= \rho_{m0} + A\tau_m\phi^L \\ \phi^H &= 1 - \left(\frac{1-\chi^p}{1-\chi^p\chi^w} + \chi^p\right)\chi^p \\ \phi^L &= 1 - \left(\frac{1-\chi^p}{1-\chi^p\chi^w} + \chi^p\right) \end{aligned} \tag{A.30}$$

- The cadherin cluster amount ρ_c will also decrease and increase with increasing and decreasing ρ_m in a periodic way between a high ρ_c^H and a low value ρ_c^L approximately given by

$$\begin{aligned} \rho_c^H &\simeq \left(\frac{e^{\gamma_1\zeta_1\Delta\mu A\tau_m\phi^L}}{1+e^{\gamma_1\zeta_1\Delta\mu A\tau_m\phi^L}}\right)n \\ \rho_c^L &\simeq \left(\frac{e^{\gamma_1\zeta_1\Delta\mu A\tau_m\phi^H}}{1+e^{\gamma_1\zeta_1\Delta\mu A\tau_m\phi^H}}\right)n \end{aligned} \tag{A.31}$$

- Now we can estimate the dynamics of length and plot the approximate analytic phase diagrams. From these piecewise solution of ρ_m and limiting cases of ρ_c

we can estimate the effective rest length at the maximum of myosin ρ_m during nth pulse (i.e., at $t = (n-1)(\tau_p + \tau_m) + \tau_p$) to be

$$L^s \simeq L^* + \tau_L \zeta_1 \Delta\mu \rho_m^n + \beta_1 \rho_c(\rho_m^n)$$

- Now it can be such that the very first pulse ($n = 1$) in the pulse train makes the effective rest length very small ($L_1^s \to 0$) signifying a junction collapse. The condition for this will be given by $L_1^s \leqslant 0$. If $L_1^s \geqslant 0$ then there can be two possible outcomes in course of the whole pulse train, first if $L_1^s \geqslant 0$ for $n \to \infty$ then the resulting phase is reversible shrinkage secondly there can be cases where the junction totally shrinks ($L_n^s \to 0$) upon receiving finite number (n) of pulses.

- The second case will look like ratcheting but it is actually a reversible shrinkage and if pulse train is smaller than n pulses (for which $L_n^s \to 0$) then after pulses stop the length of the junction will return to the value of steady length in absence of any pulse ($L^* + \beta_1\rho_{c0} + \tau_L F_0^a$) within a time $t \sim \tau_m,\ \tau_c$. We call this second case *pseudo-ratcheting* (PR) and the condition for this will be $L_n^s \leqslant 0$. When written in terms of parameters these conditions $L_1^s \leqslant 0$ and $L_n^s \leqslant 0$ will be given by Eq.A.33 and Eq.A.34 respectively.

$$\begin{aligned} L^* + \tau_L\zeta_1\Delta\mu(\rho_{m0} + A\tau_m(1-\chi^p)) & \\ +\beta_1(1-e^{-\frac{\tau_p}{\tau_c}})\left(\frac{e^{\gamma_1\zeta_1\Delta\mu A\tau_m(1-\chi^p)}}{1+e^{\gamma_1\zeta_1\Delta\mu A\tau_m(1-\chi^p)}}\right)n & \\ +\beta_1\left(\frac{e^{-\frac{\tau_p}{\tau_c}}}{2}\right)n \ &\leqslant\ 0 \qquad \text{(A.32)} \\ & \qquad \text{(A.33)} \end{aligned}$$

$$L^* + \tau_L \zeta_1 \Delta\mu(\rho_{m0} + A\tau_m \phi^H) + \beta_1 \left(\frac{e^{\gamma_1 \zeta_1 \Delta\mu A \tau_m \phi^H}}{1 + e^{\gamma_1 \zeta_1 \Delta\mu A \tau_m \phi^H}} \right) n \leqslant 0 \tag{A.34}$$

A.8 Approximate analytical solutions: Leaky cadherin level dynamics

Myosin dynamics :

The dynamics of ρ_m is same as discussed in *conservative model* and given by (Eq.A.20)

Cadherin dynamics :

In this case ($\dot{n} \neq 0$) total amount of cadherin decreases when a pulse arrives if the myosin increases enough ($\rho_m > \rho_m^c$) during the "ON" period of the pulse (i.e., $t_0 < t < t_0 + \tau_p$) to trigger the structural reorganization / extraction. Now the amount of cadherin cluster amount ρ_c will decrease as myosin ρ_m increases with a coming pulse through two different ways, (i) firstly due to active force dependent enhanced fragmentation of clusters into monomer, this process has been discussed in details in the previous section, (ii) then due to possible extraction triggered by accumulation of myosin.

- To calculate the net cadherin loss during the pulse we solve the steady state of cadherin monomer ρ_1^s to be

$$-\frac{1}{\tau_c}\left(\rho_1^s - \frac{n}{1+\alpha}\right) - \beta_2 g_R \rho_1^s = 0 \tag{A.35}$$

  Here $\alpha = e^{\gamma_1 \zeta_1 \Delta\mu A \tau_m (1-\chi^p)}$ and the equation for n

$$\dot{n} = -\left(\frac{\beta_2 g_R}{(1+\alpha)(1+\tau_c \beta_2 g_R)}\right) n \tag{A.36}$$

- Solving the above equation for n, we get

$$n(t) = n_0 e^{-\kappa t} \tag{A.37}$$
$$\kappa = \frac{\beta_2 g_R}{(1+\alpha)(1+\tau_c \beta_2 g_R)}$$

  Where $n_0 = n(0)$. Now we calculate the total cadherin at the end of the pulse $n(\tau_p) = n_0 e^{-\kappa \tau_p}$.

- It is important to note that the above solutions are true in the parameter regime where ρ_1 and ρ_c relaxation is faster compared to the timescale of extraction i.e., $\tau_c < \kappa^{-1}$.

Length dynamics :
The length dynamics will be dictated by the rest length L_0 and will be affected by the changes in ρ_m and ρ_c. Approximate phase diagrams can be analytically predicted from conditions discussed below.

- The condition for reversible shrinkage will be $e^{-\kappa \tau_p} = 1$ given that $L^s > 0$ in absence of pulse.

- If the condition is true then the resulting phase will be stepwise shrinkage.

$$e^{-\kappa \tau_p} < 1 \tag{A.38}$$

- Junction collapse will happen when steady state length $L^s \leqslant 0$ at the end of the pulse ($t = \tau_p$).

$$L^* + \beta_1 \left(\frac{\alpha}{1+\alpha}\right) e^{-\kappa \tau_p} n_0 + \tau_L \zeta_1 \Delta\mu(\rho_{m0} + A\tau_m(1-\chi^p)) \leqslant 0 \tag{A.39}$$

permanent deformation of junction :

The remodelling of L_0 through extraction of cadherin represents the structural reorganization of the junction and cause a permanent/plastic deformation ΔL in the junction. The amount of this permanent deformation can be calculated from the cadherin dynamics and its effect in rest length of the junction. Here we calculate this ΔL for a single pulse

$$\begin{aligned} \Delta L &= L_1^s - L_0^s \\ &= \frac{\beta_1 n_0}{2}\left(e^{-\kappa\tau_p} - 1\right) \end{aligned} \tag{A.40}$$

References

[1] R. Phillips , J. Kondev, J. Theriot 2008. Physical Biology of the Cell. New York: Garland Sci.

[2] Munjal, A. and Lecuit, T. (2014). Actomyosin networks and tissue morphogenesis. Development 141, 1789-1793.

[3] Lecuit, T. and Lenne, P. F., Cell surface mechanics and the control of cell shape, tissue patterns and morphogenesis. Nature Rev. Mol. Cell Biol. **8**, 633644 (2007).

[4] Leptin, M., Gastrulation movements: the logic and the nuts and bolts. Dev. Cell **8**, 305320 (2005).

[5] K.D. Irvine, E. Wieschaus, Cell intercalation during Drosophila germband extension and its regulation by pair-rule segmentation genes Development **120**, 827-841, (1994).

[6] T. Lecuit, P-F Lenne and E. Munro, Force Generation, Transmission, and Integration during Cell and Tissue Morphogenesis, Annu. Rev. Cell Dev. Biol., **27**, 15784, (2011).

[7] C. Bertet, L. Sulak and T. Lecuit Myosin-dependent junction remodelling controls planar cell intercalation and axis elongation, Nature, **429**, (2004).

[8] A.C. Martin, M. Kaschube and E.F. Wieschaus, Pulsed contractions of an actin-myosin network drive apical constriction, Nature **457**, 495-499 (2009).

[9] Ramaswamy, S., 2010, Annu. Rev. Condens. Matter Phys. 1, 323.

[10] M. C. Marchetti, J. F. Joanny, S. Ramaswamy, T. B. Liverpool, J. Prost, Madan Rao and R. Aditi Simha, Hydrodynamics of soft active matter, Review of Modern Physics, **85**, (2013).

[11] A. Munjal, J-M. Philippe, E. Munro and T. Lecuit, A self-organized biomechanical network drives shape changes during tissue morphogenesis, Nature **524**, 351-355 (2015).

[12] M. Rauzi, P.F. Lenne, and T. Lecuit, Planar polarized actomyosin contractile flows control epithelial junction remodelling, Nature **468**, 1110-1114 (2010).

[13] Dombrowski, C., L. Cisneros, S. Chatkaew, R. E. Goldstein, and J. O. Kessler, Phys. Rev. Lett. **93**, 098103, (2004).

[14] Narayan, V., S. Ramaswamy, and N. Menon, Science **317**, 105 , (2007).

[15] Paxton, W. F., K. C. Kistler, C. C. Olmeda, A. Sen, S. K. S. Angelo, Y. Cao, T. E. Mallouk, P. E. Lammert, and V. H. Crespi, 2004, J. Am. Chem. Soc. 126, 13 424.

[16] Palacci, J., S. Sacanna, A. P. Steinberg, D. J. Pine, and P. M. Chaikin, 2013, Science 339, 936.

[17] Parrish, J. K., and W. M. Hamner, Animals Groups in Three Dimensions: How Species Aggregate (Cambridge University Press, Cambridge, England) , (1997).

[18] Serra-Picamal, X., V. Conte, R. Vincent, E. Anon, D. T. Tambe, E. Bazellieres, J. P. Butler, J. J. Fredberg, and X. Trepat, 2012, Nat. Phys. 8, 628.

[19] Surrey, T., F. J. Ne de lec, S. Leibler, and E. Karsenti, 2001, Science 292, 1167.

[20] Jon Bertsch, from underwater images from the Sea of Cortez: http://www.thalassagraphics.com/blog/?p=167 .

[21] Vicsek,T., Czirok,A., Ben-Jacob,E., Cohen,I., and Shochet,O., Novel type of phase transition in a system of self-driven particles, Phys. Rev. Lett. **75**, 1226, (1995).

[22] Toner,J., and Tu,Y., Flocks, herds, and schools: A quantitative theory of flocking Phys. Rev. E **58**, 4828, (1998).

[23] Prost, J., and R. Bruinsma, 1996, Europhys. Lett. 33, 321.
Ramaswamy, S., J. Toner, and J. Prost, 2000, Phys. Rev. Lett. 84, 3494.
Ramaswamy, S., and M. Rao, 2001, C. R. Acad. Sci. Paris, Se rie IV2, 817.

[24] Kruse, K., J. F. Joanny, F. Ju licher, J. Prost, and K. Sekimoto, 2005,Eur. Phys. J. E 16, 5.
Ju licher, F., K. Kruse, J. Prost, and J.-F. Joanny, 2007, Phys. Rep. 449, 3.

[25] Gre goire, G., and H. Chate , 2004, Phys. Rev. Lett. 92, 025702.

[26] Pinot, M., F. Chesnel, J. Z. Kubiak, I. Arnal, F. J. Nedelec, and Z.Gueroui, 2009, Curr. Biol. 19, 954.
Ne de lec, F., T. Surrey, A. Maggs, and S. Leibler, 1997, Nature (London) 389, 305.
Head, D. A., W. J. Briels, and G. Gompper, 2011, BMC Biophysics 4, 18.

[27] Simha, R. A., and S. Ramaswamy, 2002a, Phys. Rev. Lett. 89, 058101.

[28] Ramaswamy, S., R. A. Simha, and J. Toner, 2003, Europhys. Lett. 62, 196.

[29] J. Howard, Mechanics of Motor Proteins and the Cytoskeleton, Sinauer Associates, Sunderland (2001).

[30] Campos-Ortega JA, Hartenstein V (1985) The embryonic development of Drosophila melanogaster. Springer, Berlin.

[31] A.C. Martin, Pulsation and stabilization: Contractile forces that underlie morphogenesis, Dev. Biol. **341**, 114125, (2010).

[32] J. Solon, A. Kaya-Copur, J. Colombelli and D. Brunner, Pulsed forces timed by a ratchet-like mechanism drive directed tissue movement during dorsal closure. Cell **137**, 1331-1342 (2009).

[33] C. Meghana, N. Ramdas, F. M. Hameed, M. Rao, G. V. Shivashankar, and M. Narasimha, Integrin adhesion drives the emergent polarization of active

cytoskeletal stresses to pattern cell delamination, Proc. Nat. Acad. Sc. **108**, 9107-9112 (2011).

[34] G.B. Blanchard, S. Murugesu, R.J. Adams, A. Martinez-Arias, and N. Gorfinkiel, Cytoskeletal dynamics and supracellular organisation of cell shape fluctuations during dorsal closure, Development **137**, 2743-2752 (2010).

[35] M. Roh-Johnson, G. Shemer, C.D. Higgins, J.H. McClellan, A.D. Werts, U.S. Tulu, L. Gao, E. Betzig, D.P. Kiehart, and B. Goldstein, Triggering a cell shape change by exploiting preexisting actomyosin contractions, Science **335**, 1232-1235 (2012).

[36] R. Levayer and T. Lecuit, Oscillation and Polarity of E-Cadherin Asymmetries Control Actomyosin Flow Patterns during Morphogenesis, Dev. Cell **26**, 162-175 (2013).

[37] R. Fernandez-Gonzalez, and J.A. Zallen, Oscillatory behaviors and hierarchical assembly of contractile structures in intercalating cells, Phys Biol. **8**, 045005 (2011).

[38] R. Keller, L. Davidson, A. Edlund, T. Elul, M. Ezin, D. Shook and P. Skoglund, Mechanisms of convergence and extension by cell intercalation, Phil. Trans. R. Soc. Lond. **355**, 897-922 (2000).

[39] M. Rauzi, P. Verant, T. Lecuit, and P.F. Lenne, Nature and anisotropy of cortical forces orienting Drosophila tissue morphogenesis, Nat. Cell Biol. **10**, 1401-1410 (2008).

[40] M. Cavey, M. Rauzi, P.F. Lenne, and T. Lecuit, A two-tiered mechanism for stabilization and immobilization of E-cadherin. Nature **453**, 751-756 (2008).

[41] S. Yonemura, Y. Wada, T. Watanabe, A. Nagafuchi, and M. Shibata, alpha-Catenin as a tension transducer that induces adherens junction development, Nat. Cell Biol. **12**, 533-542 (2010).

[42] C.D. Buckley, J. Tan, K.L. Anderson, D. Hanein, N. Volkmann, W.I. Weis, W.J. Nelson, and A.R. Dunn, The minimal cadherin-catenin complex binds to actin filaments under force, Science **346**, 1254211 (2014).

[43] A. C. Martin, M. Gelbart, R. Fernandez-Gonzalez, M. Kaschube and E. F. Wieschaus1, Integration of contractile forces during tissue invagination, J. Cell Biol. **188**, 735-749 (2010).

[44] S. K. Wu, G. A. Gomez, M. Michael, S. Verma, H. L. Cox, J. G. Lefevre, R. G. Parton, N. A. Hamilton, Z. Neufeld and A.S. Yap, Cortical F-actin stabilization generates apicallateral patterns of junctional contractility that integrate cells into epithelia, Nat. Cell Biol. **16**, 167178 (2014)

[45] S. Banerjee, T.B. Liverpool and M.C. Marchetti, Generic phases of cross-linked active gels: Relaxation, oscillation and contractility, Europhys. Lett. **96**, 58004 (2011).

[46] S. Banerjee and M.C. Marchetti, Instabilities and oscillations in isotropic active gels. Soft Matter **7**, 463 (2011).

[47] Storm C. et al., Nature, 435 (2005) 191; Gardel M. L. et al., Science, 304 (2004) 1310.

[48] J. Keener and J. Sneyd, in *Mathematical Physiology, I: Cellular Physiology*, (2nd Ed., Springer, NY, 2009).

[49] K. Dierkes, A. Sumi, J. Solon and G. Salbreux, Spontaneous oscillations of elastic contractile materials with turnover, Phys. Rev. Lett. **113**, 148102 (2014).

[50] F. Tanaka and S.F. Edwards, Viscoelastic properties of physically crosslinked networks: Transient network theory, Macromolecules **25**, 1516-1523 (1992); Viscoelastic properties of physically crosslinked networks: Non-linear stationary viscoelasticity, J. Non-Newtonian Fluid Mech. **43** ,247-271 (1992).

[51] M. Mayer, M. Depken, J.S. Bois, F. Julicher and S.W. Grill, Anisotropies in cortical tension reveal the physical basis of polarizing cortical flows, Nature **467**, 617-621 (2010).

[52] N. W. Goehring, P. Khuc Trong, J. S. Bois, D. Chowdhury, E. M. Nicola, A. A. Hyman, and S. W. Grill, Polarizing PAR proteins by advective triggering of a pattern-forming system, Science **334**, 1137-1141 (2011).

[53] M. Doi and S. F. Edwards in *The theory of polymer dynamics*, (Oxford University Press, New York, (1986)).

[54] M. C. Marchetti, J.-F. Joanny, S. Ramaswamy, T. B. Liverpool, J. Prost, M. Rao and R.A. Simha, Hydrodynamics of Soft Active Matter, Rev. Mod. Phys. **85** 1143 (2013).

[55] R. Fernandez-Gonzalez, S. de M. Simoes, J.C. Roper, S. Eaton and J. A. Zallen, Myosin II dynamics are regulated by tension in intercalating cells, Dev. Cell **17**, 736743 (2009).

[56] M. Kovacs, K. Thirumurugan, P. J. Knight and J. R. Sellers, Load-dependent mechanism of nonmuscle myosin 2, Proc. Nat. Acad. Sc. **104**, 9994 9999 (2007)

[57] C. G. Vasquez, M. Tworoger and A. C. Martin, Dynamic myosin phosphorylation regulates contractile pulses and tissue integrity during epithelial morphogenesis, J. Cell Biol. **206**, 435-450 (2014).

[58] K. E. Kasza, D. L. Farrell and J. A. Zallen, Spatiotemporal control of epithelial remodeling by regulated myosin phosphorylation, Proc. Nat. Acad. Sc. **111**, 11732-11737 (2014).

[59] C. A. J. Fletcher in *Computational Galerkin Methods*, SpringerVerlag, New York, (1984).

[60] S. Strogatz in *Nonlinear dynamics and Chaos*, (2nd Ed., Perseus, Cambridge, MA (2014)).

[61] A. Wolf, J. Swift, H. L. Swinney, J. Vastano. Determining Lyapunov exponents from a time series. Physica D: Nonlinear Phenomena, **16**, 285-317, (1985).

[62] M. Sano and Y. Sawada, Measurement of the Lyapunov spectrum from a chaotic time series, Phys. Rev. Lett. 55, 1082 (1985).

[63] J.-P. Eckmann, S. Oliffson Kamphorst, D. Ruelle, and S. Ciliberto, Lyapunov exponents from a time series, Phys. Rev. A 34, 4971 (1986).

[64] R. Hegger, H. Kantz, and T. Schreiber, Practical implementation of nonlinear time series methods: The TISEAN package, CHAOS 9, 413 (1999).

[65] Spatiotemporal Rheochaos in Nematic Hydrodynamics, Buddhapriya Chakrabarti, Moumita Das, Chandan Dasgupta, Sriram Ramaswamy, and A. K. Sood Phys. Rev. Lett. 92, 055501, (2004).

[66] D. Banerjee et al., in preparation.

[67] K. Murthy and P. Wadsworth, Myosin-II-dependent localization and dynamics of f-actin during cytokinesis, Curr. Biol., **15**, 724731 (2005)

[68] W. Engl, B. Arasi, L. L. Yap, J. P. Thiery and V. Viasnoff, Actin dynamics modulate mechanosensitive immobilization of E-cadherin at adherens junctions, Nat. Cell Biol. **16**, 584-591 (2014)

[69] M. Guha, M. Zhou, and Y. Wang, Cortical actin turnover during cytokinesis requires myosin II, Curr. Biol., **15**, 732736 (2005)

[70] A.K. Murthy and M. Muthukumar, Dynamic mechanical properties of poly (γ-benzyl L-α-glutamate) gels in benzyl alcohol, Macromolecules **20**, 564-569 (1987).

[71] L. Leibler, M. Rubinstein and R.H. Colby, Dynamics of reversible networks, Macromolecules **24**, 4701-4707 (1991).

[72] M. Rubinstein and S. Panyukov, Nonaffine Deformation and Elasticity of Polymer Networks, Macromolecules 1997 30 (25), 8036-8044.

[73] D. S. Banerjee, A. Munjal, T. Lecuit and M. Rao, Actomyosin pulsation and flows in an active elastomer with turnover and network remodeling, Nat. Comm. 8, 1121 (2017).

[74] T. Kim, M.L. Gardel and E. Munro, Determinants of Fluidlike Behavior and Effective Viscosity in Cross-Linked Actin Networks, Biophys J. **106**, 526-534 (2014).

[75] W. M. McFadden, P. M. McCall and E. M. Munro, Filament turnover is essential for continuous long range contractile flow in a model actomyosin cortex, arXiv:1612.07430 [q-bio.SC] (2016).

[76] K. Bambardekar, R. Clement, O. Blanc, C. Chardes, and P.F. Lenne, Direct laser manipulation reveals the mechanics of cell contacts in vivo, Proc. Nat. Acad. Sc. **112**, 1416-1421 (2015).

[77] P. K. Sweby, High Resolution Schemes Using Flux Limiters for Hyperbolic Conservation Laws, SIAM J. Num. Anal. **21**, 995-1011 (1984).

[78] R.J. LeVeque in *Numerical Methods for Conservation Laws*, Lectures in Mathematics (2nd edition, Berlin, Birkhauser 1992).

[79] R. Courant, E. Isaacson and M. Rees, On the solution of nonlinear hyperbolic differential equations by finite differences, Comm. Pure App. Math. **V**, 243-255 (1952).

[80] P. Lax and B. Wendroff, Systems of conservation laws, Comm. Pure App. Math. **XIII**, 217-237 (1960).

[81] S. Gottlieb and C-W. Shu, Total variation diminishing Runge-Kutta scheme, Math. Comp. **67**, 73-85 (1988).

[82] M. Cavey, and T. Lecuit, Imaging cellular and molecular dynamics in live embryos using fluorescent proteins, Meth. Mol Biol **420**, 219-238 (2008).

[83] Rauzi, M., Verant, P., Lecuit, T. and Lenne, PF. Nature and anisotropy of cortical forces orienting Drosophila tissue morphogenesis. Nat. Cell Biol. **10**, 1401-1410 (2008).

[84] R. Levayer and T. Lecuit, Oscillation and Polarity of E-Cadherin Asymmetries Control Actomyosin Flow Patterns during Morphogenesis, Dev. Cell **26**, 162-175 (2013).

[85] R. Clement, C. Collinet, B. Dehapiot, T. Lecuit, P. F. Lenne Viscoelastic dissipation stabilizes cell shape changes during tissue morphogenesis

[86] Quang BT, Mani M, Markova O, Lecuit T and Lenne PF Principles of e-cadherin supramolecular organization in vivo Curr. Biol. **23**, 2197 -2207 (2013).

[87] Heisenberg, C.-P. and Bellache, Y. Forces in Tissue Morphogenesis and Patterning. Cell 153, 948962 (2013).

[88] Girish R. Kale, Xingbo Yang, Jean-Marc Philippe, Madhav Mani, P.F. Lenne, T. Lecuit, Two contractile pools of actomyosin distinctly load and tune E-cadherin levels during morphogenesis, bioRxiv preprint, 2018.

[89] Kerridge, S. et al. Modular activation of Rho1 by GPCR signalling imparts polarized myosin II activation during morphogenesis. Nat. Cell Biol. 18, 261270 (2016).

[90] Truong Quang, B. A., Mani, M., Markova, O., Lecuit, T. and Lenne, P. F. Principles of Ecadherin supramolecular organization in vivo. Curr. Biol. 23, 21972207 (2013).
Wu, Y., Kanchanawong, P. and Zaidel-Bar, R. Actin-Delimited Adhesion-Independent Clustering of E-Cadherin Forms the Nanoscale Building Blocks of Adherens Junctions. Dev. Cell 32, 139154 (2015).
Yap, A. S., Gomez, G. A. and Parton, R. G. Adherens Junctions Revisualized: Organizing Cadherins as Nanoassemblies. Dev. Cell 35, 1220 (2015).

[91] Sako, Y., Nagafuchi, A., Tsukita, S., Takeichi, M. and Kusumi, A. Cytoplasmic regulation of the movement of E-cadherin on the free cell surface as studied by optical tweezers and single particle tracking: corralling and tethering by the membrane skeleton. J. Cell Biol. 140, 122740 (1998).
Cavey, M., Rauzi, M., Lenne, P.-F. and Lecuit, T. A two-tiered mechanism for stabilization and immobilization of E-cadherin. Nature 453, 7516 (2008).
Buckley, C. D. et al. Cell adhesion. The minimal cadherin-catenin complex binds to actin filaments under force. Science 346, 1254211 (2014).

[92] Hoffman, B. D. and Yap, A. S. Towards a Dynamic Understanding of Cadherin-Based Mechanobiology. Trends Cell Biol. 25, 803814 (2015)

[93] Cavey, M., Rauzi, M., Lenne, P.-F. and Lecuit, T. A two-tiered mechanism for stabilization and immobilization of E-cadherin. Nature 453, 7516 (2008).

[94] Weng, M. and Wieschaus, E. Myosin-dependent remodeling of adherens junctions protects junctions from Snail-dependent disassembly. J. Cell Biol. 212, 219229 (2016).

[95] Chiou, K. K., Hufnagel, L. and Shraiman, B. I. Mechanical stress inference for two dimensional cell arrays. PLoS Comput. Biol. 8, e1002512 (2012).